THE DESIGN AND PRELIMINARY TESTING OF A LIQUID JET IN SUBSONIC CROSSFLOW TEST SETUP

SESALTI YANAKIŞ ALTINDAKİ BİR SIVI JET TEST DÜZENEĞİNİN TASARIMI VE ÖN TESTLERİ

ALİ KILIÇKAYA

PROF. DR. MURAT KÖKSAL

Thesis Supervisor

Graduate School of Science and Engineering of Hacettepe University

as a Partial Fulfilment of the Requirements for the Award of the Degree of

Master of Sciences

in Mechanical Engineering.

2024

To my family…

ABSTRACT

THE DESIGN AND PRELIMINARY TESTING OF A LIQUID JET IN SUBSONIC CROSSFLOW TEST SETUP

Ali KILIÇKAYA

Master of Science, Department of MECHANICAL ENGINEERING

Supervisor: Prof. Dr. Murat KÖKSAL

May 2024, 136 pages

Liquid jets injected into gaseous crossflows have been extensively investigated in the literature due to their wide range of applications, such as ramjet/scramjet fuel injectors, gas turbine combustors, and the agriculture industry. The available studies have mainly focused on investigating primary breakup regimes, jet trajectory, penetration, fracture length, droplet features, formation mechanisms, and droplet distribution in the liquid jet's far-field region at standard temperature and pressure (STP) conditions. This work aimed to design and manufacture a test system to investigate the characteristics of liquid jets in subsonic crossflow at high temperature and standard pressure (HTSP) and high temperature and pressure (HTP) conditions. The test system was specifically designed to house high-speed shadowgraphy and Phase Doppler Particle Analysis (PDPA) measurement systems, and preliminary tests were conducted using the high-speed shadowgraphy system. Moreover, JP-10 was used as a test liquid of jet

injected into gaseous crossflow, which was not used in the open literature before. In shadowgraphy tests, normalized values of jet penetration's length and height with jet diameter were measured and found to be between 38 and 124 and between 24.6 and 49.4, respectively, under 2 bar and 493.15 K crossflow conditions. An essential parameter for PDPA measurements, the attenuation coefficient for JP-10 was measured and found to be between 0.00871 and 0.0115 mm^{-1}. The developed test system is a valuable contribution to TÜBİTAK SAGE's infrastructure, enabling more comprehensive studies about developing related propulsion systems in the near future.

Keywords: PDPA, shadowgraphy, JP-10, liquid jet in subsonic crossflow, high temperature, high pressure.

ÖZET

SESALTI YANAKIŞ ALTINDAKİ BİR SIVI JET TEST DÜZENEĞİNİN TASARIMI VE ÖN TESTLERİ

Ali KILIÇKAYA

Yüksek Lisans, MAKİNE MÜHENDİSLİĞİ Bölümü

Tez Danışmanı: Prof. Dr. Murat KÖKSAL

Mayıs 2024, 136 sayfa

Gaz halindeki yanakışlara enjekte edilen sıvı jetler, ramjet/scramjet yakıt enjektörleri, gaz türbini yanma odası ve tarım endüstrisi gibi çok sayıda uygulamaya sahip olduğundan literatürde kapsamlı bir şekilde araştırılmıştır. Mevcut çalışmalar temel olarak birincil kırılma rejimlerini, jet eğrisini, penetrasyonunu, kırılma uzunluğunu, damlacık özelliklerini, oluşum mekanizmalarını ve standart sıcaklık ve basınç (STP) koşullarında, sıvı jetin uzak alan bölgesindeki damlacık dağılımını araştırmaya odaklanmıştır. Bu çalışmanın amacı, yüksek sıcaklık ve standart basınç (HTSP) ile yüksek sıcaklık ve basınç (HTP) koşullarındaki sesaltı yanakışa enjekte edilen sıvı jetinin özelliklerini araştırmak için bir test sistemi tasarlamak ve üretmektir. Test sistemi, yüksek hızlı gölgegrafi ve Faz Doppler Parçacık Analizi (PDPA) ölçüm sistemleri ile ölçüm alınacak şekilde tasarlanmış ve yüksek hızlı gölgegrafi sistemi kullanılarak ön testler gerçekleştirilmiştir. Ayrıca, gaz yanakışı üstüne püskürtülen jetin test sıvısı olarak, açık literatürde daha önce bu tarz çalışmalarda kullanılmayan JP-10

kullanılmıştır. Gölgegrafi testlerinde jet penetrasyonunun jet çapına göre normalize edilmiş uzunluk ve yükseklik değerleri ölçülmüş ve 2 bar ve 493.15 K yanakış koşullarında sırasıyla 38 ile 124, ve 24.6 ile 49.4 arasında bulunmuştur. PDPA ölçümleri için önemli bir parametre olan JP-10'un zayıflama katsayısı ölçülmüş ve 0.00871 ile 0.0115 mm^{-1} arasında bulunmuştur. Geliştirilen test sistemi, TÜBİTAK SAGE'nin altyapısına değerli bir katkı vererek, yakın gelecekte ilgili itki sistemlerinin geliştirilmesi konusunda daha kapsamlı çalışmalar yapılmasına olanak sağlayacaktır.

Anahtar Kelimeler: PDPA, gölgegrafi, JP-10, sesaltı yanakış altında sıvı jet, yüksek sıcaklık, yüksek basınç.

ACKNOWLEDGEMENTS

I want to express my deepest gratitude to all those who have contributed to completing this master's thesis. First and foremost, I sincerely thank my supervisor, Prof. Dr. Murat Köksal, for his invaluable guidance, unwavering support, and insightful feedback throughout this research.

Special thanks are due to my colleague, Halil Arslan, whose expertise and patience significantly enriched this thesis from test setup design to test execution. His dedication and meticulous approach were instrumental in overcoming challenges and achieving meaningful results.

I am also grateful to my colleagues, Yasemin Zengin, Ali İhsan Akbaş and Murat Sercan Şengül, who provided invaluable assistance during the testing phase. Their support and collaboration were indispensable in ensuring the smooth execution of the experiments.

Additionally, I extend my heartfelt gratitude to Dr. Bülent Sümer, Bora Yazıcı, and Tolga Tokgöz for their support and invaluable feedback throughout the research process and for graciously allowing me access to the test facility at TÜBİTAK SAGE.

Special appreciation is also extended to Altay Tekin, Levent Çağatay Öz, Mehmet Burak Solmaz, Muharrem Özgün, Muhsin Arslan, Mustafa Pelit, Okan Koçyiğit, and Yiğitcan Yanık for their support and encouragement throughout this journey.

TABLE OF CONTENTS

ABSTRACT i

ACKNOWLEDGEMENTS v

TABLE OF CONTENTS vi

LIST OF FIGURES viii

LIST OF TABLES xi

NOMENCLATURE xiii

1. INTRODUCTION 1

1.1. Introduction 1

1.2. Literature Review 2

1.3. Aim and Scope of The Thesis 10

2. DESIGN OF THE TEST SETUP 12

2.1. Test Facility at TÜBİTAK SAGE 13

2.2. 1-D Design of Test Section and Test Section Area Selection 16

2.3. Test Setup Assemblies 26

2.3.1. PDPA Test Setup Assembly 27

2.3.2. Shadowgraphy Test Setup Assembly 29

2.4. Sub-Parts of PDPA and Shadowgraphy Test Setup Assemblies 30

2.4.1. Plenum Chamber Assembly 30

2.4.2. Preliminary Acceleration Section 31

2.4.3. Test Section 32

2.4.4. Injectors 34

2.4.5. Test Section Window 35

2.4.6. Test Section Window Holder 36

2.4.7. Fuel Supply Lines 36

2.4.8. High-Pressure Chamber Assembly, PDPA 38

2.4.9. High-Pressure Chamber Assembly, Shadowgraphy 39

2.4.10. High-Pressure Chamber Window 40

2.4.11. High-Pressure Chamber Window Holder 40
2.4.12. Gaskets 41
2.5. CFD Analysis 42
2.5.1. Governing Equations and Turbulence Model 43
2.5.2. Geometry and Numerics 46
2.5.3. Mesh Sensitivity Analysis 49
2.6. Production, Endurance, and Leakage Tests of the Setup 54
2.7. Integration of Test Setup to The Test Facility 55
3. THEORY AND WORKING PRINCIPLE OF PHASE DOPPLER PARTICLE ANALYZER 56
4. RESULTS AND DISCUSSION 64
4.1. Results of CFD Analysis 64
4.2. Discharge Coefficient Measurement of Injectors 66
4.3. Attenuation Coefficient Measurement of JP-10 76
4.4. Penetration Measurement of JP-10 Liquid Jet (Shadowgraphy Test) 78
5. CONCLUSION 96
5.1. Recommendations for Future Work 97
6. REFERENCES 99
APPENDICES 104
APPENDIX 1 – Extras 104
CURRICULUM VITAE 137

LIST OF FIGURES

Figure 1.1. Schematic view of a ramjet engine [2]. 1
Figure 1.2. Schematic view of atomizers (a: pressure atomizers, b: rotary atomizers, c: twin-fluid atomizers) [3]. 3
Figure 1.3. Schematic view of liquid jet in subsonic crossflow (u_g and v_j represent crossflow and jet velocities, respectively) [4]. 5
Figure 1.4. Primary breakup process of a non-turbulent liquid jet in a gaseous crossflow where gas Weber numbers are 0 (no breakup), 3 (capillary breakup), 8 (bag breakup), 30 (multimode breakup), and 220 (shear breakup) for a, b, c, d, and e, respectively [4]. 6
Figure 2.1. Schematic view of test facility by Lubarsky et al. [55]. 13
Figure 2.2. Schematic view of the test facility at TÜBİTAK SAGE. 14
Figure 2.3. Test facility at TÜBİTAK SAGE. 14
Figure 2.4. PDPA test setup assembly (isometric view). 28
Figure 2.5. PDPA Test setup assembly (cross-sectional view 1 and 2). 28
Figure 2.6. Shadowgraphy test setup assembly (isometric view). 29
Figure 2.7. Plenum chamber assembly (isometric view). 31
Figure 2.8. Preliminary acceleration section (isometric view). 32
Figure 2.9. Test section (isometric view). 33
Figure 2.10. Injector (isometric view). 34
Figure 2.11. Injector (cross-sectional view). 34
Figure 2.12. Test section window holder (back and front views). 36
Figure 2.13. Fuel supply line 1 (isometric view). 37
Figure 2.14. Fuel supply line 2 (isometric and cross-sectional views). 37
Figure 2.15. High-pressure chamber assembly, PDPA (isometric view). 38
Figure 2.16. High-pressure chamber assembly, shadowgraphy (isometric view). 39
Figure 2.17. High-pressure chamber window holder (back and front views). 41
Figure 2.18. Plenum chamber flange gasket. 42
Figure 2.19. High-pressure chamber flange gasket. 42
Figure 2.20. The geometry of the test system used in CFD analysis. 47
Figure 2.21. Mesh comparison. 50
Figure 2.22. Control line and plane for results of mesh sensitivity analysis. 51
Figure 2.23. Mass-weighted average static pressure on the plane given in Figure 2.22 for analysis done using coarse, medium, fine, and very fine meshes. 52
Figure 2.24. Static pressure on nodes passing through the line given in Figure 2.22 for analysis done using coarse, medium, fine, and very fine meshes. 53
Figure 2.25. View of fine mesh and the plane for the cross-sectional view of some part of it. 53

Figure 2.26. The cross-sectional view of the fine mesh that passes through the plane given in Figure 2.25. 54
Figure 2.27. View of produced test setup and testing process (endurance and leakage). 55
Figure 2.28. Integrated shadowgraphy test setup assembly at the test facility at TÜBİTAK SAGE. 55
Figure 3.1. TSI two-component PDPA System at test facility at TÜBİTAK SAGE [64]. 56
Figure 3.2. Schematic view of the transmission side of PDPA [65]. 57
Figure 3.3. Measurement volume [66]. 57
Figure 3.4. Schematic view of light scattering by droplets ($n_p > n_m$) and bubbles ($n_p < n_m$); general definitions and calculations with ray tracing software for a water droplet in air (a, b) and for an air bubble in water (c, d) [65]. 59
Figure 3.5. Schematic view of Phase Doppler measurement setup [65]. 59
Figure 3.6. Scattering domain and off-axis angle (scattering angle) [67]. 62
Figure 3.7. Feasible scattering modes for various domains, attenuation levels, and polarization [67]. 63
Figure 4.1. The contours of the velocity magnitude on the plane shown in Figure 2.22 for cases given in Table 2.9. 65
Figure 4.2. The contours of the total pressure on the symmetry plane for cases given in Table 2.9. 65
Figure 4.3. The contours of the velocity magnitude on the symmetry plane for cases given in Table 2.9. 66
Figure 4.4. Schematic view of the discharge coefficient measurement test setup. 68
Figure 4.5. View of thermocouple inside the injector. 69
Figure 4.6. Injector and sensor part view of discharge coefficient measurement test setup. 69
Figure 4.7. Discharge coefficient measurement test setup. 69
Figure 4.8. Attenuation Coefficient of JP-10 between 300 and 1100 nm wavelength. 77
Figure 4.9. Penetration of the jet for 2 g/s jet flow rate case. 88
Figure 4.10. Penetration of the jet for 3 g/s jet flow rate case. 88
Figure 4.11. Penetration of the jet for 4 g/s jet flow rate case. 89
Figure 4.12. The line inserted in the photo of the 2 g/s [1st] case in the direction of the crossflow starting from the exit of the injector to find the penetration length of the jet. 90
Figure 4.13. The grey value of pixels on the line given in Figure 4.12 to find the penetration length of the jet. 90
Figure 4.14. The line inserted in the photo of the 2 g/s [1st] case in the middle point of the penetration length interval, which is 42.5 mm from the exit of the injector in the direction of the jet starting from the wall to find the penetration length of the jet. 91
Figure 4.15. The grey value of pixels on the line given in Figure 4.14 to find the penetration height of the jet. 92
Figure A1.1. PDPA Test setup assembly (cross-sectional view 3). 115

Figure A1.2. PDPA Test setup assembly (view from both windows on the setup). 115
Figure A1.3. Shadowgraphy test setup assembly (view from both windows on the setup). 116
Figure A1.4. Plenum chamber assembly (cross-sectional view 1). 117
Figure A1.5. Plenum chamber assembly (cross-sectional view 2). 117
Figure A1.6. Preliminary acceleration section (cross-sectional view). 118
Figure A1.7. Preliminary acceleration section (top view). 118
Figure A1.8. Preliminary acceleration section (bottom view). 119
Figure A1.9. Test section (cross-sectional view 1). 119
Figure A1.10. Test section (cross-sectional view 2). 120
Figure A1.11. Test section (top view). 120
Figure A1.12. Technical drawing of injector, 0.4 mm. 121
Figure A1.13. Technical drawing of injector, 0.5 mm. 121
Figure A1.14. Technical drawing of injector, 0.6 mm. 122
Figure A1.15. Technical drawing of test section window. 122
Figure A1.16. Fuel supply line-1 (cross-sectional view). 123
Figure A1.17. High-pressure chamber assembly, PDPA (cross-sectional view 1). 124
Figure A1.18. High-pressure chamber assembly, PDPA (cross-sectional view 2). 125
Figure A1.19. High-pressure chamber assembly, shadowgraphy (cross-sectional view). 126
Figure A1.20. Technical drawing of the high-pressure chamber window. 126
Figure A1.21. Test section with window assembled. 127
Figure A1.22. Test setup sub-assembly view. 127
Figure A1.23. Test section view from windows. 128

LIST OF TABLES

Table 1.1. Atomizer types [3]. 2
Table 1.2. Correlations for jet penetration at HTSP conditions in the literature [4]. 7
Table 1.3. Correlations for jet penetration at HTP conditions in the literature [4]. 7
Table 2.1. Initial crossflow conditions for 1-D design of test section. 16
Table 2.2. The updated crossflow conditions (short form) for the 1-D design of the test section. 19
Table 2.3. Final crossflow conditions for the tests. 20
Table 2.4. Jet conditions for the tests. 24
Table 2.5. Physical properties of JP-10. 24
Table 2.6. Maximum penetration height for HTP conditions when d_j is 0.4 mm and $\dot{m}_j$ is 4 g/s (short form). 25
Table 2.7. Maximum penetration height for HTSP conditions when d_j is 0.4 mm and $\dot{m}_j$ is 4 g/s (short form). 25
Table 2.8. Settings of model for CFD analysis in Fluent. 48
Table 2.9. CFD analysis conditions. 48
Table 2.10. Mesh data. 49
Table 2.11. Mesh sensitivity analysis boundary condition. 51
Table 3.1. Attenuation level [67]. 61
Table 4.1. Comparison of 1-D equation and CFD results. 64
Table 4.2. Parameter values and associated standard deviations for Equation 4.10 [58]. 72
Table 4.3. Discharge coefficient experiment calculation results. 73
Table 4.3. Continued. 74
Table 4.3. Continued. 75
Table 4.4. Sensor data 1. 80
Table 4.5. Camera data. 80
Table 4.6. Parameter values and associated standard deviations for Equation 4.32 [58]. 85
Table 4.7. Non-dimensional numbers of the penetration experiment 1. 87
Table 4.8. Non-dimensional numbers of the penetration experiment 2. 87
Table 4.9. Penetration length and height results. 92
Table 4.10. Penetration calculations in the literature for the comparison with the current study 1. 94
Table 4.11. Penetration calculations in the literature for the comparison with the current study 2. 94
Table 4.12. Non-dimensional numbers and conditions for the jet penetration in the literature [4]. 95
Table A1.1. The required cross-sectional area of the test section. 104

Table A1.1. Continued. 105
Table A1.1. Continued. 106
Table A1.1. Continued. 107
Table A1.2. Total pressure corresponding to 600 mm^2 cross-sectional area. 107
Table A1.2. Continued. 108
Table A1.3. The updated crossflow conditions 109
Table A1.4. Maximum penetration height for HTP conditions for Bellofiore and Ragucci when d_j is 0.4 mm and m_j is 4 g/s. 110
Table A1.5. Maximum penetration height for HTP conditions for Masuda, Li, and Eslamian when d_j is 0.4 mm and m_j is 4 g/s. 111
Table A1.6. Maximum penetration height for HTSP conditions for Stenzler-1 and Lakhamraju when d_j is 0.4 mm and m_j is 4 g/s. 112
Table A1.7. Maximum penetration height for HTSP conditions for Stenzler-2 and Yoon when d_j is 0.4 mm and m_j is 4 g/s. 112
Table A1.8. Parts of test setup assemblies. 112
Table A1.8. Continued. 113
Table A1.8. Continued. 114
Table A1.9. Parts of plenum chamber assembly. 116
Table A1.10. Parts of fuel supply line 1. 123
Table A1.11. Parts of fuel supply line 2. 123
Table A1.12. Parts of high-pressure chamber assembly, PDPA. 124
Table A1.13. Parts of high-pressure chamber assembly, shadowgraphy. 125
Table A1.14. The diameter of produced injectors. 128
Table A1.15. Data of the discharge coefficient measurement experiment. 129
Table A1.15. Continued. 130
Table A1.15. Continued. 131
Table A1.16. Transmittance and Attenuation Coefficient of JP-10. 132
Table A1.16. Continued. 133
Table A1.16. Continued. 134
Table A1.17. Sensor data 2. 135
Table A1.18. Sensor data 3. 136

NOMENCLATURE

Symbols

a_0	Parameter for density calculation
a_1	Parameter for density calculation
a_2	Parameter for density calculation
A_0	The model constant of turbulence
A_2	Area of the surface 2
Ab	Absorbance
A_c	The cross-sectional area of the test section
A_{exit}	Exit area of the injector
A_s	The model constant of turbulence
α	Attenuation coefficient
β_1	Parameter for viscosity calculation
β_2	Parameter for viscosity calculation
β_3	Parameter for viscosity calculation
β_4	Parameter for viscosity calculation
c	Molarity
c_1	Model coefficient of turbulence
$c_{1\varepsilon}$	The model constant of turbulence
c_2	The model constant of turbulence
$c_{3\varepsilon}$	The model constant of turbulence
C_D	Discharge coefficient
C_{level}	Coefficient to find the attenuation level of particle
c_μ	Model coefficient of turbulence

D_1	High-pressure chamber temperature 1
D_2	High-pressure chamber temperature 2
D_3	High-pressure chamber surface temperature
D_4	Fuel temperature before entering the injector in the conditioned fuel feeding system
D_5	Fuel pressure before entering the injector in the conditioned fuel feeding system
D_6	The flow rate in the line 2
D_h	Hydraulic diameter of the test section
d_j	Exit diameter of the injector / Diameter of the jet
d_p	Particle diameter
d_{pmax}	Maximum expected particle diameter
ΔP	Pressure drop
e	Internal energy
ε	Rate of dissipation of turbulence kinetic energy
ε_{ijk}	The Levi-Cirita symbol
ϵ	Molar extinction coefficient
f	Doppler shift frequency
f_0	Frequency of shifted beam coming from the transmitter
F	External force
F_a	Apparent elastic limit or rupture modulus
g	Gravitational acceleration
γ	Specific heat ratio
G_k	The generation of turbulent kinetic energy due to mean velocity gradients
G_b	The generation of turbulent kinetic energy due to buoyancy

h	Enthalpy
h_j	Enthalpy of species
I	Unit tensor
I_l	The transmitted intensity of the light
I_0	The incident intensity of the light
J_j	Diffusion flux of species
K	Empirical constant
k	Turbulence kinetic energy
k_{eff}	Effective conductivity
k_{eotvos}	Eotvos-Ramsay coefficient
l	Thickness of the cuvette
L	Unclamped length of the window
λ	Wavelength
m	Relative refractive index
M	Mach number of the crossflow
$\dot{m}$	Mass flow rate
$m_{fuel\ storage\ tank}$	Mass of the fuel storage tank after the experiment
$\dot{m}_g$	The mass flow rate of the crossflow
$\dot{m}_j$	The mass flow rate of the jet
M_j	The molecular weight of the jet
M_w	Molecular weight
μ	Dynamic viscosity
$\mu_{air,300\ K}$	Dynamic viscosity of the air at 300 K
μ_g	Dynamic viscosity of the crossflow
μ_j	Dynamic viscosity of the jet

μ_t	Turbulent kinetic energy
μ_w	Dynamic viscosity of the water
ν	Kinematic viscosity
η	Model coefficient of turbulence
$\overline{\Omega_{ij}}$	The mean rate-of-rotation tensor viewed in a moving reference frame with the angular velocity ω_k
p	Static pressure
P_1	Pressure at the point 1
P_2	Pressure at the point 2
P_{amb}	The pressure of the ambient
P_{flow}	The pressure of the flow
P_g	Crossflow pressure
P_{max}	Load per unit area
p_{op}	Operating pressure
P_t	The total pressure of the crossflow
Φ	Phase difference
Θ	Half-beam intersection angle
Ψ	Elevation angle
φ	Scattering angle
q	Momentum flux ratio
q_c	Coefficient
r	The unclamped length-to-width ratio of the window
R	Individual gas constant
Re_{ch}	Channel Reynolds number
Re_g	Crossflow Reynolds number

Re_j	Jet Reynolds number
R_u	Universal gas constant
ρ	Density
ρ_g	Density of the crossflow
ρ_j	Density of the jet
S	Magnitude of strain-rate tensor
SF	Safety factor
S_{a_0}	Standard deviation in the parameter a_0
S_{a_1}	Standard deviation in the parameter a_1
S_{a_2}	Standard deviation in the parameter a_2
S_{β_1}	Standard deviation in the parameter β_1
S_{β_2}	Standard deviation in the parameter β_2
S_{β_3}	Standard deviation in the parameter β_3
S_{β_4}	Standard deviation in the parameter β_4
S_{C_D}	Standard deviation in the discharge coefficient
$S_{\Delta P}$	Standard deviation in the pressure drop
S_ε	User-defined source term
S_h	Volumetric heat source
S_{ij}	Strain-rate tensor
S_k	User-defined source term
S_m	Mass source
$S_{\dot{m}_g}$	Standard deviation in the mass flow rate of the crossflow
$S_{\dot{m}_j}$	Standard deviation in the mass flow rate of the jet
S_{μ_g}	Standard deviation in the dynamic viscosity of the crossflow

S_{μ_j}	Standard deviation in the dynamic viscosity of the jet
$S_{P_{amb}}$	Standard deviation in the pressure of the ambient
S_{P_g}	Standard deviation in the pressure of the crossflow
$S_{P_{flow}}$	Standard deviation in the pressure of the flow
S_q	Standard deviation in the momentum flux ratio
$S_{Re_{ch}}$	Standard deviation in the channel Reynolds number
S_{Re_g}	Standard deviation in the crossflow Reynolds number
S_{Re_j}	Standard deviation in the jet Reynolds number
S_{ρ_g}	Standard deviation in the density of the crossflow
S_{ρ_j}	Standard deviation in the density of the jet
S_σ	Standard deviation in the surface tension of the jet
$S_{T_{flow}}$	Standard deviation in the temperature of the flow
S_{T_g}	Standard deviation in the temperature of the crossflow
S_{T_j}	Standard deviation in the temperature of the jet
S_{T_r}	Standard deviation in the reduced absolute temperature
S_{u_g}	Standard deviation in the velocity of the crossflow
S_{v_j}	Standard deviation in the velocity of the jet
$S_{We_{aero}}$	Standard deviation in the aerodynamic Weber number
S_{We_g}	Standard deviation in the crossflow Weber number
S_z	Standard deviation in the penetration height
σ	Surface tension of the jet
σ_k	Turbulent Prandtl number for k
σ_ε	Turbulent Prandtl number for ε

t	Time
t_{test}	Test duration
T	Temperature
T_c	Critical temperature of the jet [JP-10]
T_0	Reference temperature
T_{flow}	Temperature of the flow
T_g	Crossflow temperature
T_j	Temperature of the jet
T_l	Transmittance of the light
T_r	Reduced absolute temperature
T_t	The total temperature of the crossflow
T_w	Thickness of the window
$\bar{\bar{\tau}}$	Stress tensor
$\bar{\bar{\tau}}_{eff}$	Effective stress tensor
ϑ	The intersection angle of the shifted and unshifted beams
U^*	Shear velocity
u_g	Velocity of the crossflow
u_j	Velocity components
v	Velocity
v_j	Velocity of the jet at the exit of the injector
We_{aero}	Aerodynamic Weber number
We_g	Crossflow Weber number
ω_k	Angular velocity
x	Penetration length
x_j	Position components

Y_M	The contribution of the fluctuating dilatation in compressible turbulence to the overall dissipation rate
z	Penetration height

Abbreviations

1-D	One Dimensional
3-D	Three Dimensional
Avg.	Average
B. Sc.	Bachelor of Science
BSP	British Standard Pipe
CFD	Computational Fluid Dynamics
DAQ	Data Acquisition
Dev.	Deviation
Dr.	Doctor
FEM	Finite Element Method
H.Ü.	Hacettepe Üniversitesi
Inc.	Incorporated
ISO	International Organization for Standardization
JP-10	Jet Propellant 10
LDV	Laser Doppler Velocimeter
M. Sc.	Master of Science
NPT	National Pipe Thread
PDPA	Phase Doppler Particle Analyzer
P/N	Part Number
Prof.	Professor

PTFE	Polytetrafluorethylene
RTV	Room Temperature Vulcanizing
SAGE	Savunma Sanayii Araştırma ve Geliştirme Enstitüsü
SS	Stainless Steel
STP	Standard Temperature and Pressure
STHP	Standard Temperature and High Pressure
HTSP	High Temperature and Standard Pressure
HTP	High Temperature and Pressure
TÜBİTAK	Türkiye Bilimsel ve Teknolojik Araştırma Kurumu
UNF	Unified Inch Fine Thread
YÖK	Yükseköğretim Kurulu

1. INTRODUCTION

1.1. Introduction

Ramjet is an air-breathing engine for supersonic applications such as air-to-air missiles, cruise missiles, and afterburners of jet aircraft. It has no moving parts and only has an inlet, a combustion chamber, fuel injectors, an igniter (or flame holder), and a converging-diverging nozzle [1]. A schematic view of a ramjet engine is given in Figure 1.1.

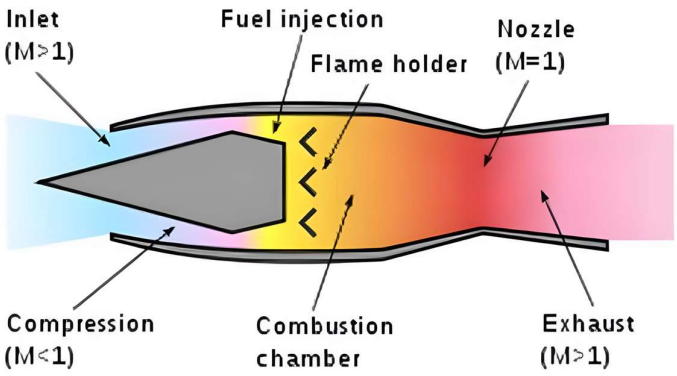

Figure 1.1. Schematic view of a ramjet engine [2].

As shown in Figure 1.1, the airspeed at the inlet of the ramjet is at supersonic conditions. It is compressed at the compression section of the engine, and its pressure increases while the velocity goes below the speed of sound. After the air is compressed and its speed is subsonic, the liquid fuel is injected through injectors placed perpendicularly on the engine's walls to incoming air. Then, mixed air fuel is ignited in the flame holder region and continues to burn after this region. Afterward, the burnt gases go through the converging-diverging nozzle section. In the converging section of the nozzle, the subsonic exhaust gases are speeded up to Mach 1 at the nozzle's throat. After the throat and in the diverging section of the nozzle, the velocity goes beyond Mach 1, in other words, supersonic velocities. Finally, the supersonic exhaust gases exit the nozzle, and the trust is obtained.

For the injection section of the engine, as was expressed above, the injectors are placed on the wall of the engine, and they inject the liquid fuel perpendicularly to the incoming air at subsonic conditions. In literature, the keyword for this type of application is the liquid jet in subsonic crossflow. In the context of this thesis, the liquid jet in subsonic crossflow was investigated.

1.2. Literature Review

Injectors are widely used technology in diverse applications, such as agriculture (disinfection of plants), home appliances (showerheads), automotive (fuel injector of internal combustion engines), the painting industry, energy, furnaces, and aerospace (gas turbines, ramjet/scramjet). Their characteristics have not been fully understood, and no exact analytical or numerical solution exists for their applications. Therefore, they still require deep research to understand the flow characteristics and develop more efficient systems.

Injectors can be categorized into four main categories which are pressure atomizers, rotary atomizers, twin-fluid atomizers, and other types of atomizers [3]. Table 1.1 and Figure 1.2 give examples of these atomizers and a schematic view of some.

Table 1.1. Atomizer types [3].

Pressure atomizers	**Rotary atomizers**	**Twin-fluid atomizers**	**Other Types**
Plain orifice	Rotating disk	Air-assist	Electrostatic
Pressure-swirl (simplex)			Ultrasonic
Square spray			Sonic (whistle)
Duplex			Windmill
Dual orifice	Rotating cup	Air-blast	Vibrating capillary
Spill return			Flashing liquid
Fan spray			Effervescent atomization

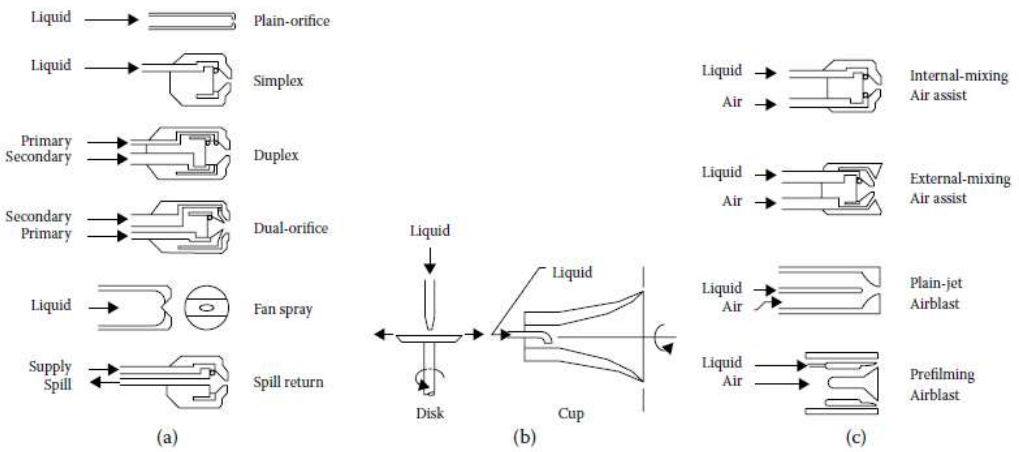

Figure 1.2. Schematic view of atomizers (a: pressure atomizers, b: rotary atomizers, c: twin-fluid atomizers) [3].

Pressure atomizers transform high pressure to kinetic energy in a small aperture [3]. This small aperture is a circular orifice for plain orifice atomizers, as shown in Figure 1.2. The applications of the pressure atomizers can be given as injectors of ramjet or internal combustion engines (plain-orifice), the injectors of turbojet or rocket engines (simplex or spill return), the showerheads (plain-orifice), the atomizers of the gas turbines (duplex), the atomizer of disinfection devices for agriculture (fan spray), etc.

Rotary atomizers inject a jet into a high-speed rotating disk or cup, and it goes through the perimeter of the rotating element. At the periphery of the component, the liquid leaves the part at a high speed [3]. This type of atomizer is generally used in paint lines, spray dryers, and other industries.

Twin-fluid atomizers consist of air assist and air blast atomizers. In air-assist atomizers, the liquid supplied to the atomizers is broken up by air provided to the atomizers at high pressure, and droplets are produced at the exit, injected to a distance by the air. The air blast atomizer works similarly to air assist atomizers,

and the only difference between them is the air assist atomizers use a small amount of air at very high velocities, and the air blast atomizers use large amounts of air at much lower velocities when compared to air assist atomizers [3]. They are generally used in gas turbines and industrial furnaces since they create fine atomization when compared to pressure atomizers.

There are also other types of atomizers, which are electrostatic, sonic (whistle), windmill, vibrating capillary, flashing liquid, and effervescent atomization [3]. Electrostatic atomizers use electric pressure to break up the liquid jet, and their application can be given as spray drying, acid etching, paint spraying, and printing [3]. In ultrasonic atomization, the liquid is supplied to a transducer that vibrates at ultrasonic frequencies, and very fine droplets are created; the application of this type of atomizer is medical sprays and humidification [3]. The information about other types of atomization can be found in [3].

In the context of this thesis, two different test setups for the experimental investigation of a liquid jet in subsonic crossflow were designed, manufactured, and using a plain orifice injector as a pressure atomizer; preliminary testing was carried out with shadowgraphy as a flow visualization method. A schematic view of a liquid jet in subsonic crossflow is given in Figure 1.3. The literature on the topic is presented below.

A liquid jet coming out of the injector is given in Figure 1.3. goes through two different breakup mechanisms, which are surface breakup and column breakup. Surface breakup occurs at the jet's periphery region due to the crossflow's high aerodynamic force. Column breakup can go through two consequent processes: primary and secondary. In the primary breakup process, the liquid jet or column coming out of the injector breaks into ligaments and bigger droplets due to axial and hydrodynamic instabilities. These ligaments and bigger droplets break into smaller droplets in the secondary breakup process. The breakup process continues until the force is balanced between droplet surface tension and

aerodynamic forces. As a result, the spray is created in the far-field region of the injector. This process can be seen in Figure 1.3.

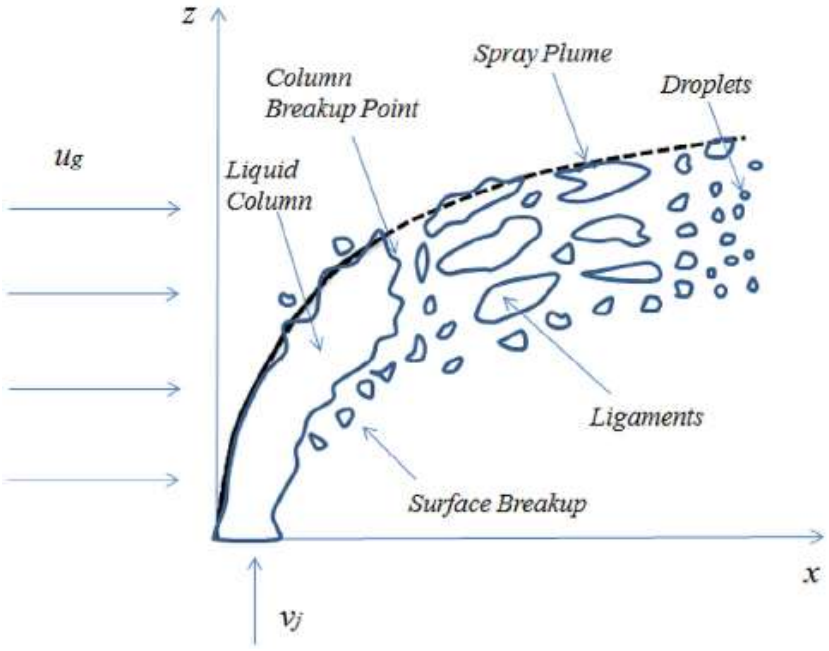

Figure 1.3. Schematic view of liquid jet in subsonic crossflow (u_g and v_j represent crossflow and jet velocities, respectively) [4].

Since the open literature is abundant in works in liquid jets in subsonic crossflow, experimental studies were given priority, excluding evaporating, and reacting flows. Also, the review was grouped using the methodology followed by M. Broumand and M. Birouk [4]. In a review paper by M. Broumand and M. Birouk [4], liquid jet in a gaseous crossflow has been investigated in four main parts as follows:

1- Liquid jet primary breakup regimes: The jet coming out of the injector goes through two subsequent processes, which are primary and secondary breakup. In the primary breakup process, the liquid jet breaks as column (ligaments), known as column breakup, and from its surface, known as surface breakup. In this process, some regimes occur in which one of the breakup modes, surface or

column breakup modes, is dominant or both modes are active, known as mixed mode, or other modes are active. These modes are defined by non-dimensional parameters of the flow, such as gas or jet Weber number, which is the ratio of the gas or jet inertial forces to surface tension forces of the jet, jet to crossflow momentum flux ratio, and Reynolds number of jet or crossflow. Details of these regimes can be found in [5-18] for non-turbulent liquid jets and in [19-27] for turbulent liquid jets. An example of the regimes can be seen in Figure 1.4, taken from [4].

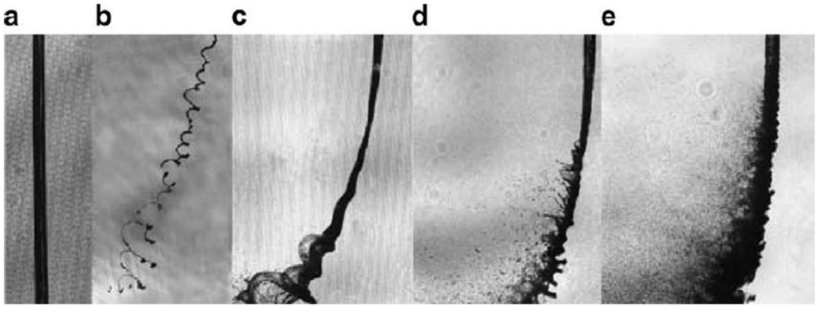

Figure 1.4. Primary breakup process of a non-turbulent liquid jet in a gaseous crossflow where gas Weber numbers are 0 (no breakup), 3 (capillary breakup), 8 (bag breakup), 30 (multimode breakup), and 220 (shear breakup) for a, b, c, d, and e, respectively [4].

2- Liquid jet trajectory and penetration: the jet's maximum trajectory and penetration into gaseous crossflow can be seen in Figure 1.3 (solid and dashed lines). It is one of the most critical aspects of the liquid jet in gaseous crossflow since it affects the droplet distribution and prevents impingement of the spray to the wall. The detailed information can be found in [5, 9, 14, 16, 27-40] for standard temperature and pressure (STP) conditions, in [8, 16, 17, 41-43] for standard temperature and high pressure (STHP) conditions, in [15, 32, 35, 40] for high temperature and standard pressure (HTSP) conditions, in [19, 44-47] for high temperature and pressure (HTP) conditions. Correlations for jet penetration are given in Tables 1.2 and 1.3 for HTSP and HTP conditions, respectively.

Table 1.2. Correlations for jet penetration at HTSP conditions in the literature [4].

Correlation	q	We_g	x/d_j	T_g [K]	Reference
$\frac{z}{d_j} = 2.630 q^{0.442} \left(\frac{x}{d_j}\right)^{0.390} We_g^{-0.088} \left(\frac{\mu_j}{\mu_w}\right)^{-0.027}$	18 - 36	1.3 - 106.2	0 - 100	291 - 573	Stenzler et al. [32]
$\frac{z}{d_j} = 1.844 \ln\left(1.324 \frac{x}{d_j} + 1\right) q^{0.456} We_g^{-0.088} \left(\frac{T_g}{T_0}\right)^{-0.117}$	1 - 49.5	50.3 - 967.5	1 - 30	366.5 - 505.4	Lakhamraju and Jeng [15]
$\frac{z}{d_j} = 3.354 q^{0.442} \left(\frac{x}{d_j}\right)^{0.391} We_g^{-0.088} \left(\frac{\mu_j}{\mu_w}\right)^{-0.027}$	9 - 18	0.9 - 164.3	0 - 100	291 - 573	Stenzler et al. [35]
$\frac{z}{d_j} = 2.241 q^{0.402} \left(\frac{x}{d_j}\right)^{0.41}$	2 - 29.1	5.3 - 47.9	0 - 27	293, 500	Yoon et al. [40]

where μ_w is the dynamic viscosity of the water at 20 ºC, T_0 is the reference temperature, and its value is 294 K.

Table 1.3. Correlations for jet penetration at HTP conditions in the literature [4].

Correlation	q	We_g	x/d_j	P_g [bar]	T_g [K]	Reference
$\frac{z}{d_j} = 15 q^{0.5} \left(\frac{x}{d_j}\right)^{0.33} We_g^{-0.41} \left(\frac{\mu_j}{\mu_w}\right)^{-0.027}$	2.2 - 75	700 - 1580	0 - 12	3.8 - 6.5	350 - 475	Masuda and McDonell [45]
$\frac{z}{d_j} = 0.909 q^{0.476} \left(\frac{x}{d_j}\right)^{0.35} We_{aero}^{-0.128} Re_g^{0.135}$	12.2 - 71.4	We_{aero} = 10.4 - 410.5	0 - 12	10, 20	300, 600	Bellofiore et al. [44]
$\frac{z}{d_j} = 2.28 q^{0.422} \left(\frac{x}{d_j}\right)^{0.367} We_{aero}^{-0.015} \left(\frac{\mu_g}{\mu_{air,300\ K}}\right)^{0.186}$	5 - 280	We_{aero} = 7 - 340	0 - 12	20	600	Ragucci et al. [46]
$\frac{z}{d_j} = 1.44 \ln\left(1.06 \frac{x}{d_j} + 1\right) q^{0.4356} We_g^{0.01147} \left(\frac{T_g}{T_0}\right)^{0.295}$	16 - 76	399 - 1630	0 - 40	5 - 20	280 - 650	Li et al. [47]
$\frac{z}{d_j} = 0.191 q^{0.3} \left(\frac{x}{d_j}\right)^{0.43} Re_{ch}^{0.12} Re_j^{0.14}$	10 - 80	20 - 487	0 - 17	2.1 - 5.2	298 - 573	Eslamian et al. [19]

where μ_w is the dynamic viscosity of the water at 20 ºC, T_0 is the reference temperature, and its value is 280 K.

3- Liquid jet breakup length: it is the length where the first column breakup point occurs, and it can be seen in Figure 1.3 as the column breakup point. It has two parts: one is column breakup distance, which is defined as the distance between the jet exit center of the injector and the column breakup point's projection parallel to the crossflow, and the other is the column breakup height, which is defined as the distance between jet exit center of the injector and the column breakup point's projection perpendicular to the crossflow. The detailed information can be found in [5, 7-9, 11, 20, 23, 26, 27, 33, 36, 38, 39, 41, 44, 46, 48-50] for column breakup distance and in [5, 9, 11, 20, 23, 27, 33, 38, 39, 41, 44, 46, 48, 50] for column breakup height.

4- Droplet features and formation mechanisms: as explained before, two consequent processes occur for the liquid jets in gaseous crossflow, which are primary and secondary breakup. The primary breakup process occurs at the near field region of the liquid jet, and detailed information can be found in [7, 12, 21, 23, 24, 26, 51]. The secondary breakup occurs at the far-field region of the liquid jet, and the droplet distribution occurs because of the secondary breakup. For the far-field region, the works that use PDPA as a flow visualization method can be found in [9, 17, 29, 52-56]. Other works related to the far field region can be found in [4].

The works related to the PDPA used as a flow visualization method are given below. It was seen that JP-10 was not used as a test liquid for the liquid jet in any of these works. JP-10 is a jet fuel developed mainly for military use in missiles at low temperatures (freezing point: -79 °C) and is a single-component synthetic fuel. It has more energy density when compared to traditional petroleum-based fuels, e.g., JP-8 (Jet-A). Still, it is costly, making it unattractive to use in other applications, such as fuel for aircraft.

Inamura and Nagai [53] investigated jet breakup images and spray behavior (droplet size, velocity, and mass flux distributions) experimentally at STP conditions using PDPA and high-speed cameras as flow visualization methods and water as test liquid. They found that droplet diameter reaches its maximum in the peripheral mixing region at low crossflow velocity and in the core region at high crossflow velocity. Also, it is pointed out in the study that the maximum droplet velocity is reached in the peripheral mixing region for the whole crossflow velocity range.

In another study conducted by Wu et al. [54], jet penetration and spray behavior (droplet size, velocity, and volume flux distributions) were studied experimentally at STP conditions using PDPA as a flow visualization method and water as a test liquid. They discovered that the droplets penetrate further into crossflow at high jet-to-crossflow momentum flux ratios.

Rachner et al. [52] investigated jet penetration and droplet size distribution experimentally and numerically at STHP conditions (6-9 bar) using PDPA and high-speed cameras as flow visualization methods and Kerosene Jet A-1 as test liquid. In the study, a comprehensive model of liquid jet atomization in crossflow is presented, and it is validated by comparing the model outputs with experimental results. They think that the model presented is a valuable tool for seeing the effects of design modifications of a given configuration for the Lean Premixed Prevaporized combustion concept.

Furthermore, Tambe et al. [9] investigated breakup modes (column, mixed, and surface breakup), breakup location, jet penetration, and spray behavior (droplet size and velocity distributions) experimentally at STP conditions using PDPA and high-speed cameras as flow visualization methods and water, Jet-A and N-Heptane as test liquids. They found that droplet sizes decrease by increasing the crossflow velocity while penetration increases by increasing the injector diameter or momentum flux ratio. They also found that the droplet size reaches its

maximum in the spray core region at low momentum flux ratios and in the periphery region at high momentum flux ratios.

Lubarsky et al. [55] investigated spray behavior (droplet size and velocity distributions) experimentally to investigate the effect of Weber number at high temperature (555 K) and high pressure (4 atm) (HTP) conditions using PDPA as flow visualization method and Jet-A as test liquid. They found that the larger droplets produced at low crossflow velocity and penetrated further into crossflow, and the smaller droplets produced at high crossflow velocity. They also showed a double peak distribution of droplet size at low crossflow velocity.

In another study conducted by Farvardin et al. [29], breakup modes, jet penetration, and spray behavior (droplet size, velocity, and volume flux distributions) were studied experimentally to compare biodiesel and diesel jets at STP conditions using PDPA and high-speed cameras as flow visualization methods. They found that breakup regimes and trajectory differed greatly for biodiesel blends and attributed this to biodiesel's high viscosity.

Finally, Song et al. [17] investigated breakup modes, jet penetration, and spray behavior (droplet size distribution) experimentally, focusing on the impact of surrounding air pressure at STHP conditions (2.07 - 9.65 bar) using PDPA and high-speed cameras as flow visualization methods and Jet A-1 as test liquid. They showed that spray can penetrate further into crossflow by increasing crossflow pressure at constant momentum flux ratio and crossflow Weber number. Moreover, they proposed a correlation for the mean drop size.

1.3. Aim and Scope of The Thesis

The injector dynamics in crossflow have not been fully understood, and there is no exact analytical, numerical, or experimental solution for their application. They still require deep research to develop related system efficiencies further.

Thus, this thesis aims to design and manufacture two different test setups for the experimental investigation of the liquid jet in subsonic crossflow for ramjet applications using high-speed camera visualizations and PDPA and carry out preliminary tests. The results of this thesis are also expected further to develop TÜBİTAK SAGE's capabilities in this field. The main novelty of the thesis is the consideration of using JP-10 as the jet fluid since there is no study in the open literature regarding this fuel.

To reach the set objectives:

- Two different test setups for investigation of the liquid jet in subsonic crossflow at HTSP and HTP conditions were designed and manufactured,
- Preliminary high-speed camera, temperature, and pressure measurements were carried out to investigate the flow patterns.

The study's scope is limited to subsonic flow conditions within the pressure and temperature ranges of 1.10 - 4.00 bar and 393.15 - 673.15 K, respectively.

2. DESIGN OF THE TEST SETUP

In this section, the design of the test setups to do a test about the liquid jet in subsonic crossflow is presented. Firstly, the information about the test facility at TÜBİTAK SAGE is given. Afterward, the design requirements of the test setups are given, and using these requirements, 1-D design calculations were performed to find the required cross-sectional area of the test section. Then, the assemblies of the test setups are presented, and sub-parts of the test setups are explained. After that, computational fluid dynamics (CFD) analysis of the designed setup, which was run to verify the design, is presented. Then, production, endurance, and leakage tests are presented. Finally, the integration of the test setup into the test facility is presented.

The 3-D design of the test setups is based on a test setup given in a work by Lubarsky et al. [55]. The experimental setup used by Lubarsky et al. [55] can be seen in Figure 2.1. The setup and its sub-parts given in Figure 2.1 were the most explicit setup for the investigation of the liquid jet in subsonic crossflow in the literature. Therefore, it was chosen as base of the design in the context of this thesis.

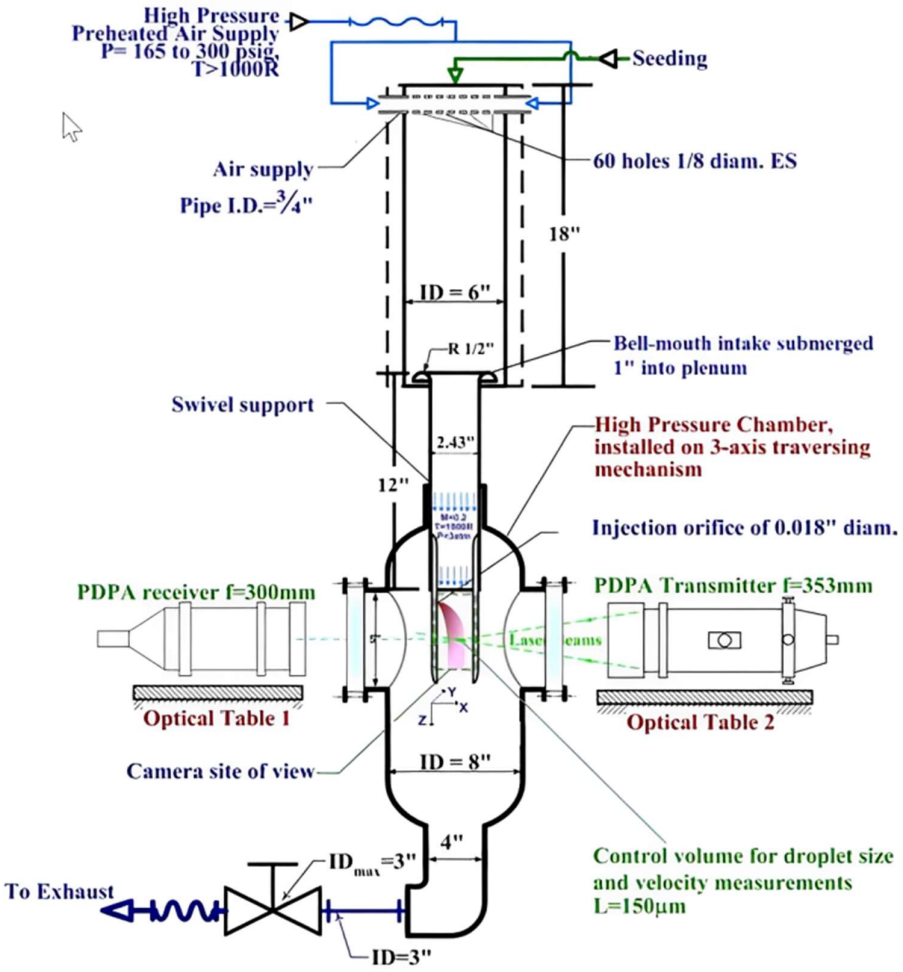

Figure 2.1. Schematic view of test facility by Lubarsky et al. [55].

2.1. Test Facility at TÜBİTAK SAGE

This section provides information about the test facility at TÜBİTAK SAGE, where the tests about the liquid jet in subsonic crossflow are done. Figure 2.2 shows a schematic view of the test facility, and Figure 2.3 presents a photograph of the facility.

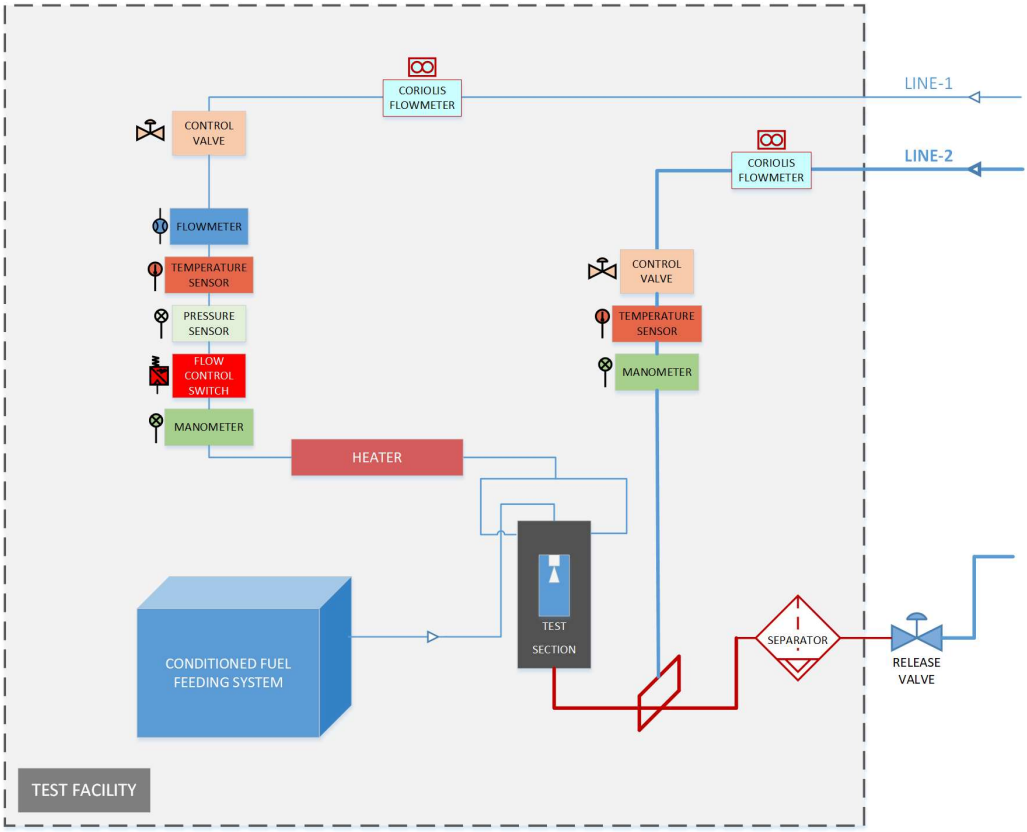

Figure 2.2. Schematic view of the test facility at TÜBİTAK SAGE.

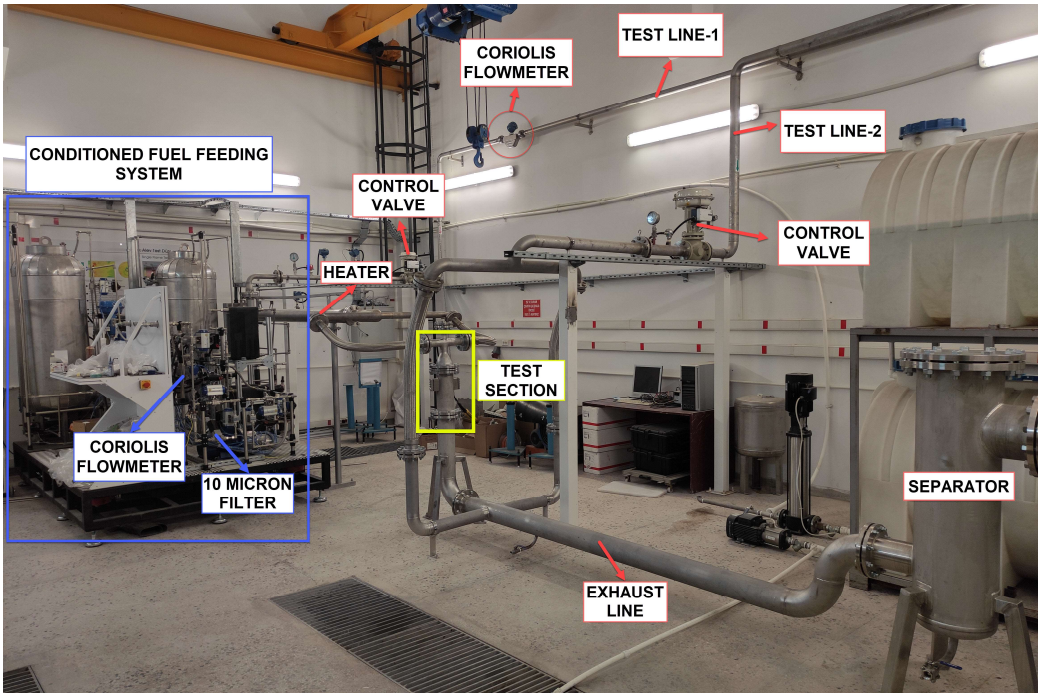

Figure 2.3. Test facility at TÜBİTAK SAGE.

The test facility is situated in TÜBİTAK SAGE, and different experimental studies can be conducted there. In the context of this thesis, the designed and produced test setups are placed and connected to this test facility.

In the facility, air or nitrogen can be used as test gases, heated to 400 °C, and pressurized to 10 bar. If air is used for the tests, the maximum applicable flow rate in test line-1 is 70 g/s, and if nitrogen is used in the system, the maximum applicable flow rate in test line-1 is 85 g/s. Also, the system can supply different fuels, such as JP-8, JP-10, and kerosene, and condition them (heat up or cool down).

The air or the nitrogen is supplied to the facility via test lines from outside the facility, and the air or nitrogen supply systems outside the facility are not given in the thesis. There are two test lines (line 1 and line 2). Air/nitrogen is adjusted to the desired flow rate by the control valve in line 1, passes through the heater, which heats the flow to the desired temperature and reaches the test section in line 1. On the other hand, line 2 connects with the outlet of the test section, and the heated air/nitrogen that comes from the test section meets the unconditioned air/nitrogen coming from line 2, so the temperature of the air/nitrogen coming from the test section is cooled down. Then, the chilled flow goes through the atmosphere, passing through the exhaust line and valve. The release valve lets the chilled flow go to the atmosphere and pressurizes the setup. There are measurement elements on line 1 and line 2 to measure flow rate, temperature, and pressure, and control valves to adjust the flow rate.

On the exhaust line, a separator separates the fuel and air/nitrogen mixture coming from the test section. The separated fuel is stored at the bottom section of the separator, and the air/nitrogen goes through the release valve.

A conditioned fuel feeding system supplies the fuel to the injector in the test section. The conditioned fuel feeding system can heat up or cool down the fuel

to the desired temperature by the heating and cooling system placed in the conditioned fuel feeding system. Also, the conditioned fuel feeding system adjusts the fuel flow rate by the pump and vanes placed in the system. The fuel flow rate is measured via a Coriolis flowmeter placed in the system. The system prevents plugging the injector by filtering the fuel with the help of a 10-micron filter placed in the system.

2.2. 1-D Design of Test Section and Test Section Area Selection

As explained in the previous section, the test facility at TÜBİTAK SAGE can condition the crossflow medium between standard atmospheric temperature and 400 °C and between standard atmospheric pressure and 10 bar. In a subsonic flow, the Mach number is below 1. Therefore, the crossflow conditions were set in Table 2.1, considering these conditions. The aim was to choose crossflow conditions as HTP since there is not much work at these conditions, so the pressure and temperature below 2 bar and 393.15 K were not considered. The pressure above 8 bar was also not considered since the maximum applicable pressure is 10 bar for the facility. Also, the Mach number below 0.1 was not considered due to the corresponding low velocity, and the Mach number above 0.7 was also eliminated due to the capability of the test facility.

Table 2.1. Initial crossflow conditions for 1-D design of test section.

Mach Number	Total Pressure [bar]	Total Temperature [K]
0.1 - 0.7 (0.1 incremental)	2 - 5 - 8	393.15
		493.15
		593.15
		673.15

TÜBİTAK SAGE's air/nitrogen supply, conditioning, and pressurization system can supply 70 g/s of air and 85 g/s of nitrogen, condition, and pressurize them

until 400 ºC and 10 bar, respectively. Three primary methodologies were used to design the test setup based on the constraints of the test facility, and they are given below.

1. 1-D compressible flow theory
2. Empirical relations for jet penetration
3. 3-D single-phase CFD simulations

1-D compressible flow theory was used to calculate the required cross-sectional area of the test section. After finding the required area, the empirical relations for jet penetration were used to find the area's dimensions. Finally, 3-D single-phase CFD simulations were done to check flow conditions inside the designed setup using the first two methodologies. In the following sections, each of these methodologies is explained in detail.

Considering these conditions and conditions in Table 2.1, the required cross-sectional area of the test section is calculated and evaluated based on the 1-D compressible flow equations with isentropic flow assumption.

In a 1-D isentropic flow, the mass flow rate equation can be given as Equation 2.1 [57].

$$\dot{m}_g = \frac{A_c P_t}{\sqrt{T_t}} \sqrt{\frac{\gamma}{R}} M \left(1 + \frac{\gamma - 1}{2} M^2\right)^{-\left(\frac{\gamma+1}{2(\gamma-1)}\right)} \tag{2.1}$$

where $\dot{m}_g$ is the mass flow rate of the crossflow, A_c is the cross-sectional area of the test section, P_t is the total pressure of the crossflow, T_t is total temperature of the crossflow, γ is specific heat ratio, R is individual gas constant and M is mach

number of the crossflow. Equation 2.2 can be obtained by leaving A_c term alone on one side:

$$A_c = \frac{\dot{m}_g\sqrt{T_t}}{MP_t}\sqrt{\frac{R}{\gamma}}\left(1+\frac{\gamma-1}{2}M^2\right)^{\left(\frac{\gamma+1}{2(\gamma-1)}\right)} \quad (2.2)$$

Equation 2.2 is used to find the required cross-sectional area of the test section. Using 85 g/s mass flow rate, Equation 2.2, air's physical properties, and conditions given in Table 2.1, the cross-sectional area of the test section was calculated and found between 57.0 and 1588.3 mm^2. The detailed values can be seen in Table A1.1 of Appendix 1.

By analyzing the results and considering the part's manufacturability, it was thought that an area smaller than 600 mm2 is not easy to produce, and the jet can hit the opposite wall with this area. Therefore, the conditions corresponding to the area smaller than 600 mm^2 were removed from the test range, but further calculations were carried out, as explained below. By leaving the P_t term in Equation 2.2 on one side, Equation 2.3 can be obtained:

$$P_t = \frac{\dot{m}_g\sqrt{T_t}}{MA_c}\sqrt{\frac{R}{\gamma}}\left(1+\frac{\gamma-1}{2}M^2\right)^{\left(\frac{\gamma+1}{2(\gamma-1)}\right)} \quad (2.3)$$

Equation 2.3 finds the maximum total pressure that a test can be performed corresponding to the 600 mm^2 cross-sectional area of the test section. Using 85 g/s mass flow rate, 600 mm^2 cross-sectional area of the test section, Equation 2.3, air's physical properties and conditions given in Table 2.1 (except total pressure), maximum total pressure corresponding to 600 mm^2 cross-sectional area was calculated and found between 0.761 and 5.294 bar. The detailed values can be seen in Table A1.2 of Appendix 1.

Considering the results above, the updated Table 2.1 (crossflow test conditions) is given in Table 2.2 in short form. The required cross-sectional area for these conditions was calculated and provided in the same table. The detailed values can be seen in Table A1.3 of Appendix 1.

Table 2.2. The updated crossflow conditions (short form) for the 1-D design of the test section.

Mach Number	**Total Pressure [bar]**	**Total Temperature [K]**	**Required Cross-Sectional Area of the Test Section [mm^2]**
0.1 - 0.4 (0.1 incremental)	1.10 - 4.00	393.15	601.84 - 1588.27
		493.15	
		593.15	
		673.15	

In Table A1.3, the required cross-sectional area values are larger than 600 mm^2, meaning all these tests could be done in one test section with an area of 600 mm^2. The maximum flow rate is 85 g/s, which is the flow rate for the minimum area in Table A1.3. Since the area is constant and 600 mm^2, the required flow rate for the conditions must be re-calculated using Equation 2.1. The required flow rate was calculated and given in Table 2.3 as the final crossflow conditions.

Table 2.3. Final crossflow conditions for the tests.

Mach Number	Total Pressure [bar]	Total Temperature [K]	Mass Flow rate [g/s]
0.1	2.00	393.15	42
		493.15	38
		593.15	34
		673.15	32
	4.00	393.15	84
		493.15	75
		593.15	68
		673.15	64
0.2	2.00	393.15	83
		493.15	74
		593.15	67
		673.15	63
0.3	1.41	393.15	85
		493.15	76
		593.15	69
		673.15	65
0.4	1.10	393.15	85
		493.15	76
		593.15	69
		673.15	65

The cross-sectional area of the test section was chosen and found to be 600 mm^2. The dimensions of the test section were decided by considering the maximum penetration distance since the jet should not hit the wall. Several correlations in the literature can be used to estimate the jet penetration distance, given in Tables 1.2 and 1.3. The correlations presented in Tables 1.2 and 1.3 were used to find and compare maximum penetration distances, then the dimensions of the cross-sectional area of the test section were decided.

The related parameters are found in Tables 1.2 and 1.3 using Equations 2.4-2.17. The following formulations and non-dimensional numbers were used to find the penetration correlations given in Tables 1.2 and 1.3. These are the non-dimensional numbers mostly used in the literature to develop correlations, such as momentum flux ratio, which is the jet-to-crossflow momentum flux ratio; crossflow Weber number, which is the ratio of the inertial forces of the crossflow to the surface tension force of the jet, and crossflow and channel Reynolds numbers.

The momentum flux ratio is defined as:

$$q = \frac{\rho_j v_j^2}{\rho_g u_g^2} \tag{2.4}$$

where ρ_j is the density of the jet, v_j is the velocity of the jet at the exit of the injector, ρ_g is the density of the crossflow and u_g is the velocity of the crossflow.

The crossflow Weber number is defined as:

$$We_g = \frac{\rho_g u_g^2 d_j}{\sigma} \tag{2.5}$$

where d_j is the exit diameter of the injector and σ is the surface tension of the jet.

The crossflow temperature is calculated from:

$$T_g = T_t \left(1 + M^2 \frac{\gamma - 1}{2}\right)^{-1} \tag{2.6}$$

where T_t is the total temperature of the crossflow, M is Mach number of the crossflow and γ is specific heat ratio.

The crossflow pressure is calculated from:

$$P_g = P_t \left(1 + M^2 \frac{\gamma - 1}{2}\right)^{-\left(\frac{\gamma}{\gamma - 1}\right)} \tag{2.7}$$

where P_t is total pressure of the crossflow.

The aerodynamic Weber number is defined as:

$$We_{aero} = \frac{\rho_g v_j^2 d_j}{\sigma} \tag{2.8}$$

The crossflow Reynolds number is defined as:

$$Re_g = \frac{\rho_g u_g d_j}{\mu_g} \tag{2.9}$$

where μ_g is the dynamic viscosity of the crossflow found using Sutherland's law.

$$\mu_g = \frac{1.458 \times 10^{-6} \times T_g^{3/2}}{T_g + 110.4} \tag{2.10}$$

$$Re_{ch} = \frac{\rho_g u_g D_h}{\mu_g} \tag{2.11}$$

where Re_{ch} is channel Reynolds number, and D_h is the hydraulic diameter of the test section, which was assumed to be circular since it was not known in the design process.

$$D_h = \sqrt{4A_c/\pi} \tag{2.12}$$

where A_c is the cross-sectional area of the test section.

$$Re_j = \frac{\rho_j v_j d_j}{\mu_j} \tag{2.13}$$

where Re_j is jet Reynolds number and μ_j is the dynamic viscosity of the jet.

$$v_j = \frac{\dot{m}_j}{\rho_j A_{exit}} \tag{2.14}$$

where $\dot{m}_j$ is the mass flow rate of the jet and A_{exit} is the exit area of the injector.

$$A_{exit} = \frac{\pi d_j^2}{4} \tag{2.15}$$

$$\rho_g = \frac{P_g R}{T_g} \tag{2.16}$$

where R is the specific gas constant.

$$u_g = M\sqrt{\gamma R T_g} \tag{2.17}$$

Table 2.4 gives the jet conditions for the tests. The jet is not conditioned for the test, so its temperature is at the ambient temperature, which is assumed to be 20 °C. Table 2.5 gives the jet's physical properties. For the test setup, three different injectors with exit diameters of 0.4 mm, 0.5 mm, and 0.6 mm were designed.

Table 2.4. Jet conditions for the tests.

Jet Type	**Temperature [°C]**	**Mass Flow rate [g/s]**
JP-10	20	2
JP-10	20	3
JP-10	20	4

Table 2.5. Physical properties of JP-10.

Density [kg/m^3] [58]	935.7
Dynamic viscosity [Pa.s] [58]	3.0752 x 10^{-3}
Surface tension [N/m] [59]	0.031

Using correlations and x/d_j ratios given in Tables 1.2 and 1.3, Equations 2.4-2.17, physical properties of air, values given in Tables 2.3-2.5, maximum penetration heights were found for each condition and injector. The penetration correlations for the 0.4 Mach cases were taken from Table 1.2 (HTSP condition correlations table), and Table 1.3 was used for the remaining cases. The worst case for the design was considered here, and it was seen in the calculation results that the calculations for the injector, whose diameter is 0.4 mm, and for the jet condition, which is 4 g/s flow rate case, is the worst case. In other words, the worst case is the case where maximum penetration height occurs. The results of maximum penetration height can be found in Tables 2.6 and 2.7 for this case. The detailed values are in Tables A1.4 - A1.7 of Appendix 1.

Table 2.6. Maximum penetration height for HTP conditions when d_j is 0.4 mm and $\dot{m}_j$ is 4 g/s (short form).

M	P_t [bar]	T_t [K]	z [mm] (Masuda)	z [mm] (Bellofiore)	z [mm] (Ragucci)	z [mm] (Li)	z [mm] (Eslamian)
0.1 - 0.3	1.41 - 4.00	393.15 - 673.15	11.76 - 60.10	12.39 - 25.54	13.10 - 29.99	15.64 - 39.37	11.44 - 19.40

Table 2.7. Maximum penetration height for HTSP conditions when d_j is 0.4 mm and $\dot{m}_j$ is 4 g/s (short form).

M	P_t [bar]	T_t [K]	z [mm] (Stenzler-1)	z [mm] (Lakhamraju)	z [mm] (Stenzler-2)	z [mm] (Yoon)
0.4	1.10	393.15 - 673.15	20.90	8.94 - 9.52	26.78	16.56

As shown in Tables 2.6 and 2.7, correlations estimate the penetration height in a very wide range, and there is no consensus among them. The reason might be that the conditions (momentum flux ratio, total temperature, total pressure, Weber numbers, etc.) given in Tables A1.4 - A1.7 of Appendix 1 differ from those in Tables 1.2 and 1.3. e.g., applicable ranges of momentum flux ratio, crossflow Weber number, pressure and temperature are between 2.2 and 75, 700 and

1580, 3.8 and 6.5 bar, 350 and 475 K, respectively, in Masuda's work, and between 16 and 76, 399 and 1630, 5 and 20 bar, 280 and 650 K, respectively, in Li's work, and between 49 and 390, 36 and 285, 1.1 and 4 bar, 393.15 and 673.15 K, respectively, in the current work. The detailed values of conditions and non-dimensional numbers considered in the correlations and current work can be seen in Tables 1.2 and 1.3 and A1.4 - A1.7 of Appendix 1, respectively. Therefore, it can be said that the correlations might not be applicable here and are not developed for the current case because the conditions and non-dimensional numbers of the current work are different from the works in the literature.

When the results of correlations are investigated, the maximum value of the penetration height is 60.10 mm, as predicted by Masuda et al. Considering maximum penetration height, it was decided to choose dimensions of the cross-section of the test section 20x30 mm, corresponding to the 600 mm^2 cross-sectional area found before. 30 mm dimension will be used in the direction of the jet. This dimension might not be used for some cases in Tables A1.4 - A1.7, but as explained before, the correlations might not be correct for the current work, and this phenomenon is checked while doing the test with the setup.

The test section and other parts of the test setup were designed using the dimensions found in this section. They are given in the following sections.

2.3. Test Setup Assemblies

3D parts of the test setup assemblies are presented in this section. Two different test setup assemblies were designed and manufactured for this thesis. One is for the test to measure the diameter and velocity distributions of droplets with PDPA. The other is for the shadowgraphy tests of the liquid jet in crossflow with a high-speed camera. The detailed parts of the assemblies are given in Table A1.8 of Appendix 1. The only difference between the two setups is the high-pressure chamber assembly.

2.3.1. PDPA Test Setup Assembly

PDPA test setup assembly is used to measure velocity and diameter distributions in the test section. The designed setup is shown in Figures 2.4-2.5 and A1.1-A1.2 of Appendix 1.

The crossflow gas enters the setup via two inlets placed on the plenum chamber assembly, then goes through the plenum chamber assembly and is uniformed here. Afterward, it goes through the preliminary acceleration section, and it speeds up here before entering the test section. After that, it goes through the test section, and its speed increases to the designed/desired condition. The liquid jet enters the test setup via fuel supply line-1 and goes through fuel supply line-2 by passing through 2 male connectors. Then, it goes through the positional elbow, and there it goes to the injector. The injector injects it perpendicularly to crossflow. The crossflow-liquid jet mixture exits the test section and enters the high-pressure chamber, and it leaves the test setup via the crossflow-liquid jet exit jet placed on the high-pressure chamber.

Five thermocouples and one pressure sensor were placed in the setup to measure crossflow and liquid jet temperature and pressure, respectively. The setup contains four windows, two of which are placed on the high-pressure chamber assembly and two placed on the test section. The angles between windows placed on the high-pressure chamber assembly and test section are 150 and 180 degrees, respectively. In other words, the windows in the test section are placed opposite, but the windows in the high-pressure chamber are not placed opposite. An explanation of the placement of the windows is given in upcoming sections.

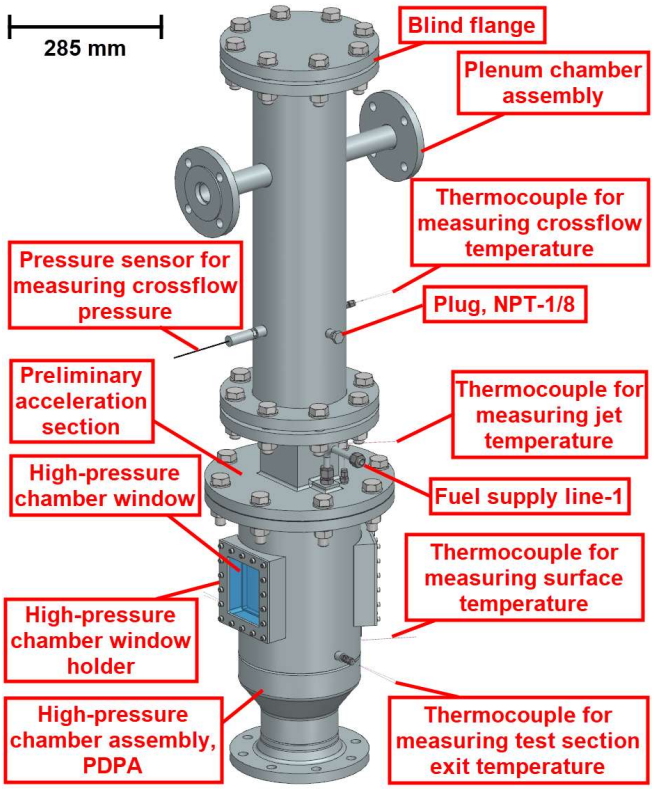

Figure 2.4. PDPA test setup assembly (isometric view).

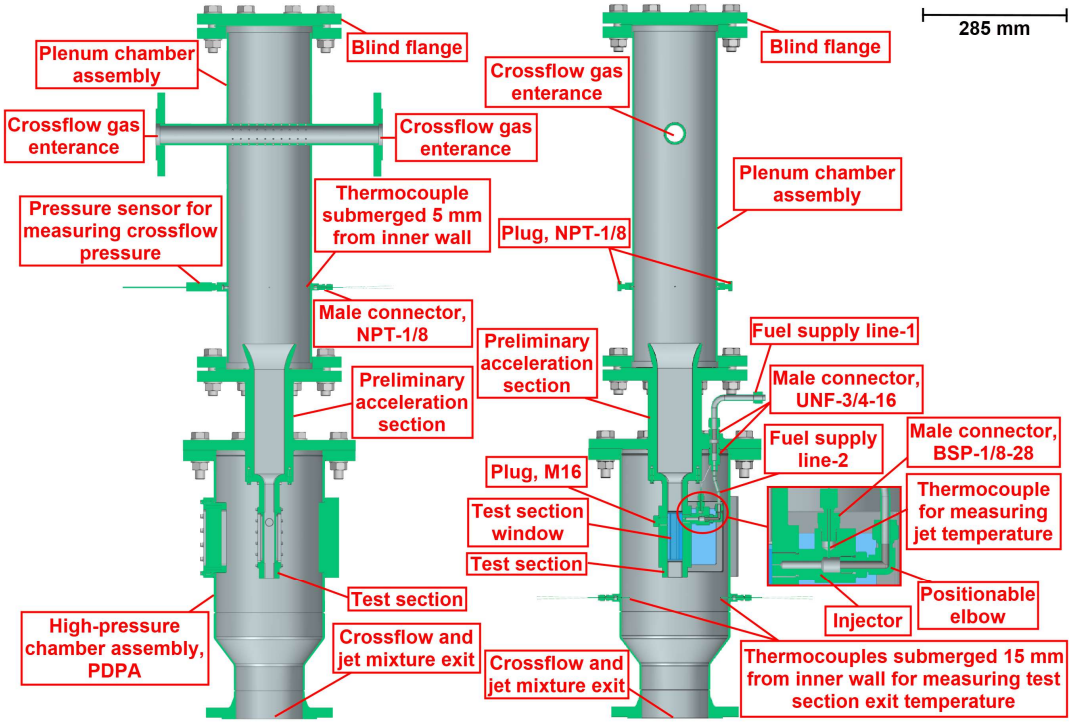

Figure 2.5. PDPA Test setup assembly (cross-sectional view 1 and 2).

2.3.2. Shadowgraphy Test Setup Assembly

The shadowgraphy test setup assembly is used to take high-speed photos of the liquid jet in subsonic crossflow in the test section. The designed setup is shown in Figures 2.6 and A1.3 of Appendix 1.

The only difference between shadowgraphy and PDPA test setup assemblies is the design of the high-pressure chamber assembly and, in detail, the windows' placement on the assembly. The windows on high-pressure chamber assembly, PDPA are not placed oppositely, but they are placed oppositely on high pressure assembly, shadowgraphy. Apart from this point, both setups work identically in point of flow dynamics (crossflow and liquid jet). Therefore, the explanation of the flow dynamics is not given again.

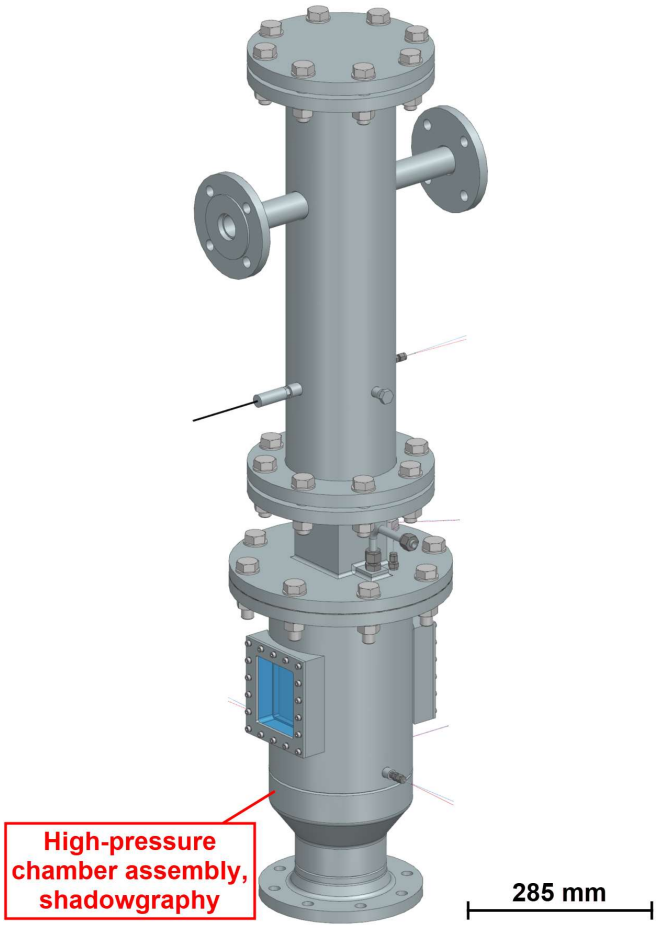

Figure 2.6. Shadowgraphy test setup assembly (isometric view).

2.4. Sub-Parts of PDPA and Shadowgraphy Test Setup Assemblies

In this section, important sub-parts of test setup assemblies are given. The list of whole parts of the test setup assemblies is given in Table A1.8 of Appendix 1.

All parts are designed to work at least at 10 bar, and while creating the parts, the strength values supplied by the standards or manufacturers for parts were checked, and it was found that finite element analysis (FEM) was not necessary. Therefore, FEM analysis was not done, and all parts can endure much more than 10 bar. On the other hand, an analytical analysis was conducted to check the endurance level of windows, which is given in related sections of this thesis. Moreover, the setups that were produced were tested at 10 bar at the production facility, which is given in the related section of this thesis.

2.4.1. Plenum Chamber Assembly

The plenum chamber assembly stores the incoming gas and sends it to the preliminary acceleration section. It consists of the parts given in Table A1.9 of Appendix 1. The parts in Table A1.9 were machined or taken off the shelf and assembled by welding. In conclusion, the plenum chamber assembly was produced. It can be seen in Figure 2.7 and Figures A1.4-A1.5 of Appendix 1.

As shown in Figure A1.4 of Appendix 1, the flow uniformity pipe has small holes, and these holes uniform the incoming gas, which is a similar design given in Figure 2.1. The holes' diameter is 3 mm, and sixty of them are equally spaced in ten circular sections, and six are spaced in each section. The chamber also has one pressure sensor fitting for pressure sensor connection and three thermocouples fitting for thermocouple connections. The sensor connections in the entire setup were only placed on the plenum chamber assembly so as not to affect the uniformity of the flow in test or preliminary acceleration sections. Therefore, there is no sensor connection in test or preliminary acceleration sections, and the required data for these regions is taken from the sensors placed on the plenum chamber assembly.

Only one thermocouple is connected to the plenum chamber assembly for the shadowgraphy test and the test with PDPA, and the other two connection points are closed by plugs for these tests. The uniformity of gas in the plenum chamber assembly is checked by three thermocouples. Therefore, all thermocouple fittings are connected by thermocouples, and this is a different test from the shadowgraphy test and tests with PDPA, which is called the flow uniformity checking test. This is why the plenum chamber assembly has three thermocouples fitting on itself; only one is used for the tests except for the flow uniformity checking test.

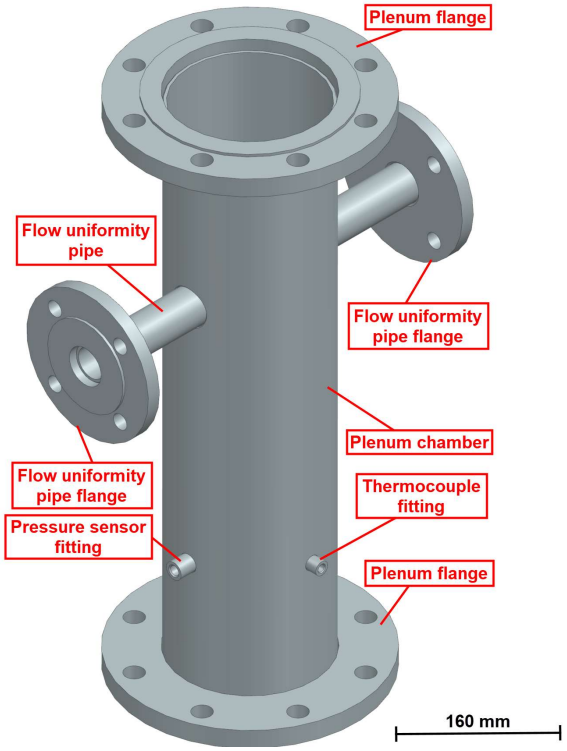

Figure 2.7. Plenum chamber assembly (isometric view).

2.4.2. Preliminary Acceleration Section

The preliminary acceleration section is used to accelerate the crossflow gas coming from the plenum chamber assembly to a level slower than the speed in the test section. The crossflow gas was not accelerated to the desired or designed speed in the test section by connecting it directly to the plenum chamber

so as not to let the flow separation occur. Therefore, a section between the test section and the plenum chamber assembly is placed, and it is the preliminary acceleration section. Preliminary acceleration also converts the circular flow in the plenum chamber assembly to rectangular flow. The part was manufactured from bulk stainless steel by machining. The part and its connections, as well as some of the dimensions and interfaces, can be seen in Figure 2.8 and Figures A1.6-A1.8 of Appendix 1.

As shown in Figure 2.8, the crossflow entrance region to the preliminary acceleration section from the plenum chamber assembly is submerged in the plenum chamber assembly to prevent flow separation in the preliminary acceleration section.

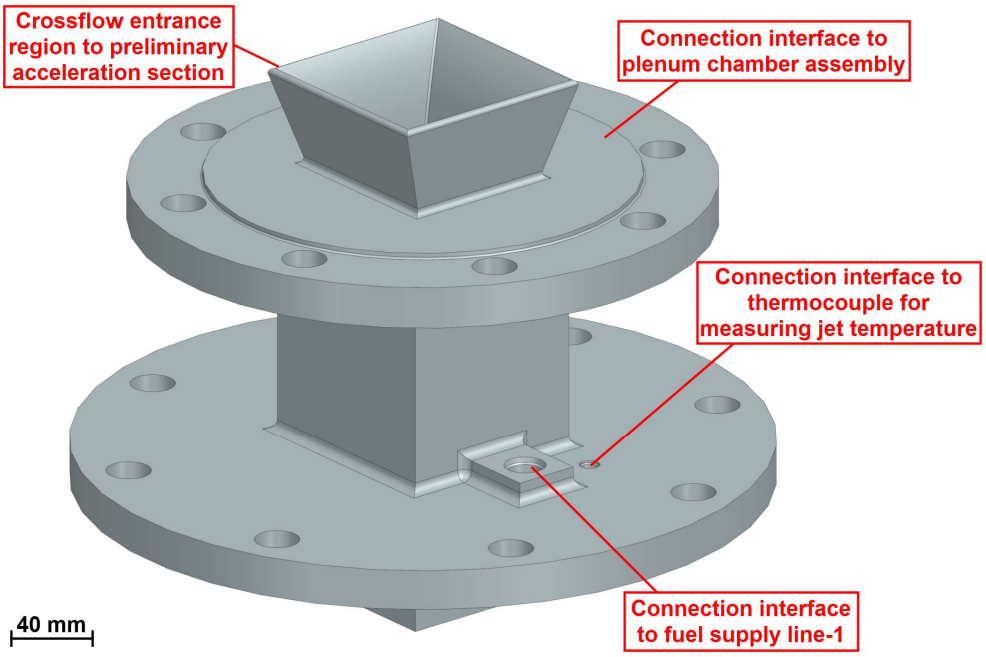

Figure 2.8. Preliminary acceleration section (isometric view).

2.4.3. Test Section

The test section is the region where the measurements and visualization of a liquid jet in subsonic crossflow are captured. The crossflow coming from the

preliminary acceleration section is speeded up to the designed point. The cross-sectional area of the visualization/measurement section is 600 mm^2 (20x30 mm), as found in Section 2.2. The part was manufactured from bulk stainless steel by machining. It and its connections, some of the dimensions and interfaces can be seen in Figure 2.9 and in Figures A1.9-A1.11 of Appendix 1.

As can be seen in Figure A1.9 of Appendix 1, the part has two injector connections which of one is placed 5 mm under the other because this placement makes possible of visualization of the liquid jet in test section if the upper placement is not satisfactory for visualization. Therefore, while doing the tests, the test injector is connected to one of them and other one is covered with plug, M16.

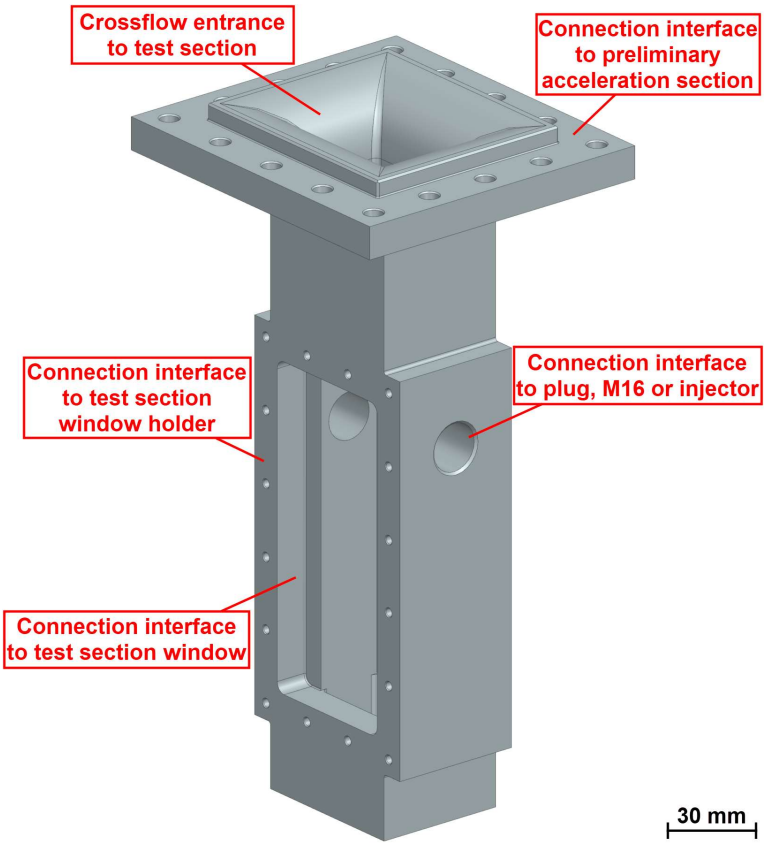

Figure 2.9. Test section (isometric view).

2.4.4. Injectors

Three different injectors with different orifice diameters (0.4, 0.5, and 0.6 mm) were designed. All the injectors have a length-to-diameter ratio of 10. 3D parts and technical drawings of injectors are given in Figures 2.10-2.11 and A1.12-A1.14 of Appendix 1. Each injector has one inlet for fuel, exit orifice and a connection port for thermocouple connection to measure jet temperature in injector. The parts were produced from a bulk stainless steel by machining.

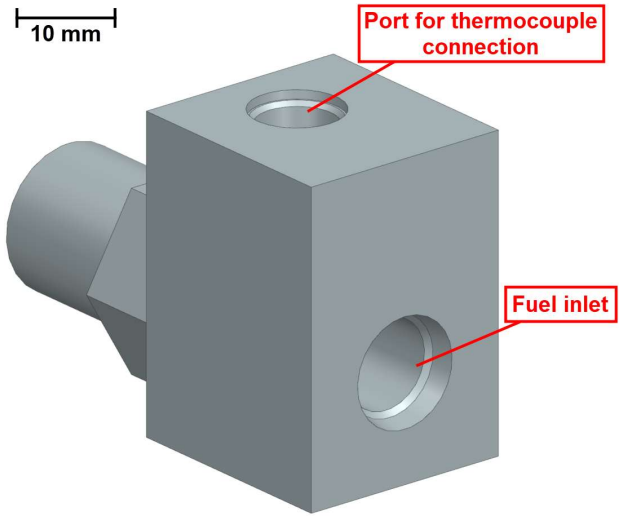

Figure 2.10. Injector (isometric view).

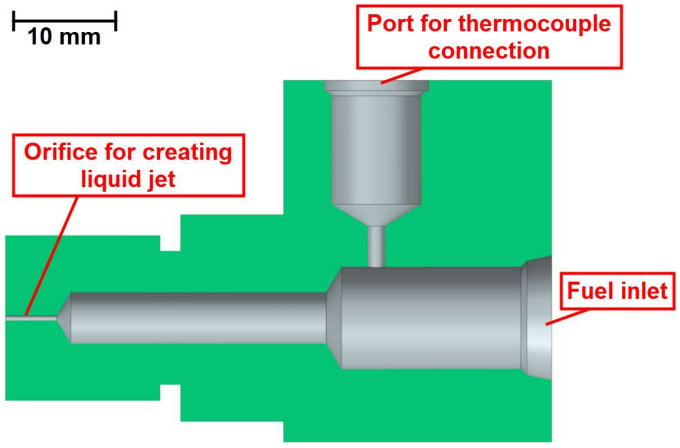

Figure 2.11. Injector (cross-sectional view).

2.4.5. Test Section Window

The test section window is used to observe the region where a liquid jet in subsonic crossflow occurs. It is placed on the test section and was produced by machining from bulk optical-grade quartz.

The test section window is placed inside the high-pressure chamber assembly, as can be seen in Figure 2.5, and this makes the pressure on both sides of the window equal or the pressure difference between both sides of the window is close to zero, so it does not carry the load (pressure), and this lets us choose a thin material. The thickness of the test section window should be as thin as possible since the receiver of PDPA does not look perpendicular to the test section window. Lubarsky et al. [55] chose the thickness of their test section window as 3.18 mm. Therefore, the thickness of the test section window is selected as 3.2 mm, and it is assumed that this thickness does not affect velocity and diameter measurements by PDPA. The window's technical drawing can be seen in Figure A1.15 of Appendix 1

As seen in Tables A1.4 and A1.5 of Appendix 1, the difference between total and static pressures at maximum is 0.11 bar, the pressure the test section window needs to carry. The safety factor for the window at this load was calculated by Equation 2.18 and found to be 83. Equation 2.18 is a safety factor calculation formula given by a quartz manufacturer in a technical report [60].

$$SF = \frac{2 \times F_a \times (1 + r^2)}{K \times P_{max}} \left(\frac{T_w}{L}\right)^2 \tag{2.18}$$

where SF is the safety factor, F_a is the apparent elastic limit or rupture modulus (its value is 41x10^6 Pa for quartz [61]), r is the unclamped length-to-width ratio of window (in the case, unclamped length and width of the window are 96 mm and 30 mm, respectively), K is empirical constant (its value is 1.125 [60]), P_{max} is the

load per unit area (its value was found above and is 0.11x10^5 Pa), T_w is the thickness of the window (its value is 3.2 mm for the case), L is unclamped length of the window (its value is 96 mm for this case).

2.4.6. Test Section Window Holder

The test section window holder places the test section window on the setup and keeps it steady. It can be seen in Figure 2.12.

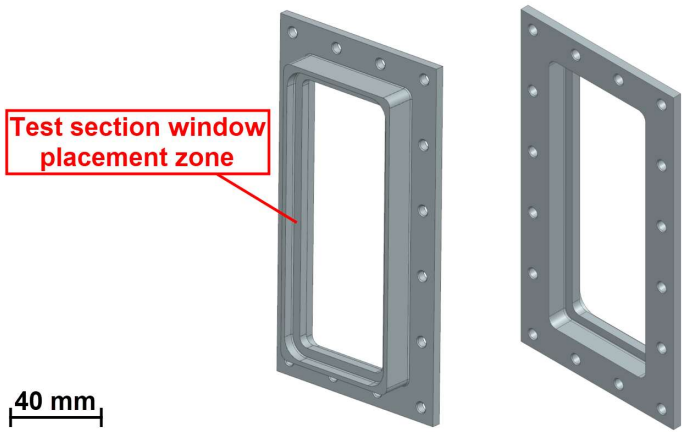

Figure 2.12. Test section window holder (back and front views).

2.4.7. Fuel Supply Lines

Fuel supply lines 1 and 2 feed JP-10 to the injector. As Figure 2.5 shows, fuel supply line 1 is the connection part outside the test setup to the conditioned fuel feeding system at the test facility given in Figures 2.2 and 2.3, and fuel supply line 2 is the connection part inside the test setup between fuel supply line 1 and the injector.

Fuel supply line 1 consists of the parts in Table A1.10 of Appendix 1. Fuel pipe 1 was produced by tube bending. Nut, 810, and ferrule set, 810, were taken off the shelf. Nuts and ferrules were connected to the produced pipe permanently by the method given in [62]. As a result, the fuel supply line 1 was produced. It can be seen in Figure 2.13 and Figure A1.16 of Appendix 1.

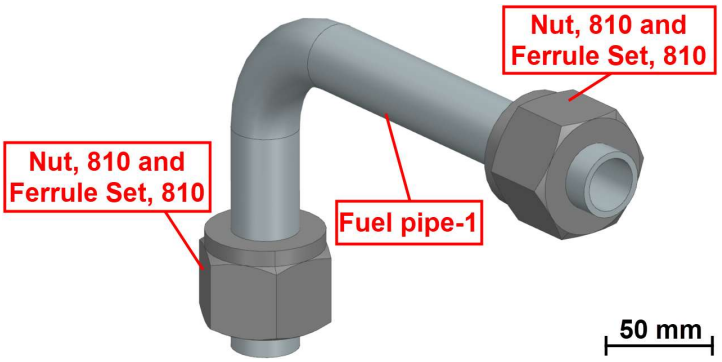

Figure 2.13. Fuel supply line 1 (isometric view).

Fuel supply line 2 consists of the parts given in Table A1.11 of Appendix 1. Fuel pipe 2 and the adaptor were produced by tube bending and from bulk stainless steel by machining, respectively, and then, the pipe and adaptor were connected by welding. Nut, 400, ferrule set, 400, nut, 810, and ferrule set, 810 were taken off the shelf. Nuts and ferrules were connected to the welded part permanently by the method given in [62]. As a result, the fuel supply line 2 was produced. It can be seen in Figure 2.14.

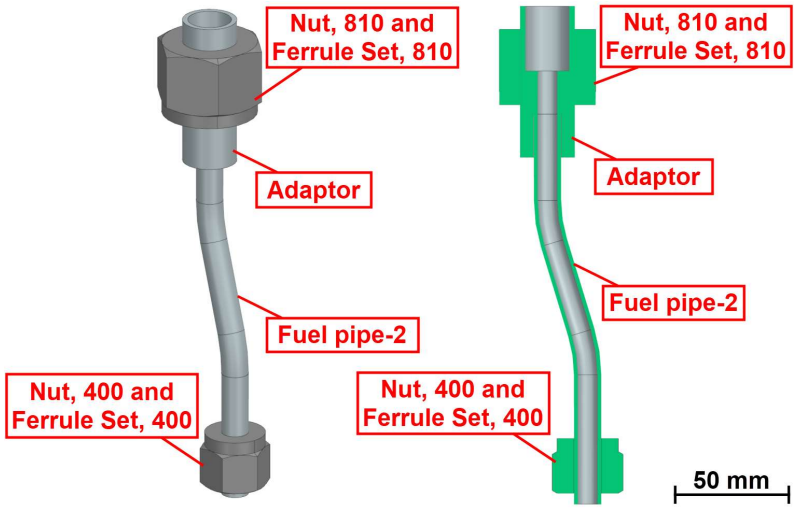

Figure 2.14. Fuel supply line 2 (isometric and cross-sectional views).

2.4.8. High-Pressure Chamber Assembly, PDPA

High-pressure chamber assembly, PDPA is used to connect the preliminary acceleration section and the test section and to equalize the pressure on each side of the test section window to make the test section window thin since the receiver of PDPA does not look perpendicularly to the test section window. Therefore, it affects the accuracy of diameter and velocity measurements by PDPA. It has two window openings, one of which is used to let laser beams of the transmitter of PDPA reach the test section, and the other is used to let the receiver of PDPA observe the test section that interfered laser beams of the transmitter of PDPA. These openings are not placed oppositely on the chamber, and they are placed at 150 degrees. This placement is related to the accuracy and calibration of the PDPA system. The details about the accuracy and calibration of PDPA are given in the related section.

The chamber consists of the parts given in Table A1.12 of Appendix 1. The parts given in Table A1.12 are either machined or taken off the shelf and assembled by welding. In conclusion, the high-pressure chamber assembly, PDPA, was produced. It can be seen in Figure 2.15 and Figures A1.17-A1.18 of Appendix 1.

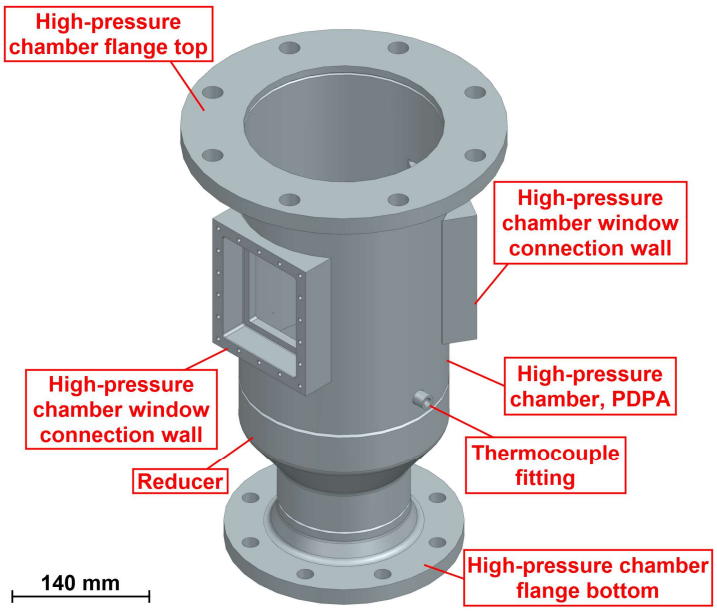

Figure 2.15. High-pressure chamber assembly, PDPA (isometric view).

2.4.9. High-Pressure Chamber Assembly, Shadowgraphy

High-pressure chamber assembly, shadowgraphy is used to connect the preliminary acceleration section and test section and to equalize the pressure on each side of the test section window to make the test section window thin. It has two window openings; one lets the light source lighten up the test section to create a shadowgraphy region, and the other allows a high-speed camera to observe the test section. These openings are placed oppositely on the chamber. Apart from the window opening placement on the chamber, the remaining parts are identical to the high-pressure chamber assembly, PDPA.

The chamber consists of the parts given in Table A1.13 of Appendix 1. The parts given in Table A1.13 are either machined or taken off the shelf and assembled by welding. In conclusion, the high-pressure chamber assembly, shadowgraphy was produced. It can be seen in Figure 2.16 and Figure A1.19 of Appendix 1.

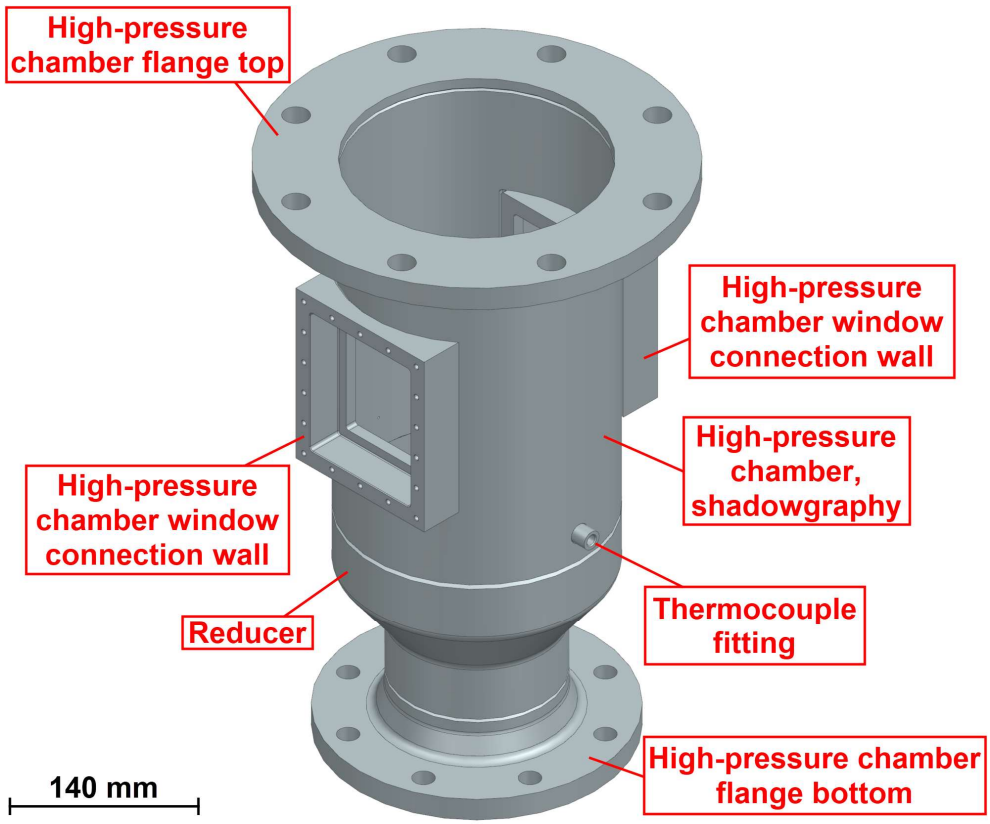

Figure 2.16. High-pressure chamber assembly, shadowgraphy (isometric view).

2.4.10. High-Pressure Chamber Window

The high-pressure chamber window is used to observe the test section region where liquid jet in subsonic crossflow occurs. It is placed on high-pressure chamber assemblies and produced from a bulk optical grade quartz by machining.

TÜBİTAK SAGE has been doing tests with PDPA for more than ten years. At this period, it was seen that PDPA system accuracy or calibration was not affected when 30 mm thickness windows were placed perpendicularly in front of the transmitter and receiver of PDPA. Therefore, the thickness of the high-pressure chamber window was chosen as 30 mm so as not to break windows at 10 bar and make the system safer. The window's technical drawing can be seen in Figure A1.20 of Appendix 1.

The maximum load (pressure) that the high-pressure chamber window needs to carry is 10 bar, but this is the absolute pressure, and assuming ambient pressure as 1 bar, the maximum net pressure can be found as 9 bar. By taking thickness, unclamped length, and width of the window as 30 mm, 110 mm, and 90 mm, respectively, the safety factor for window at 9 bar was calculated by Equation 2.18 and found as 15.

2.4.11. High-Pressure Chamber Window Holder

The high-pressure chamber window holder is used to place the high-pressure chamber window on the setup and keep it steady. It is shown in Figure 2.17.

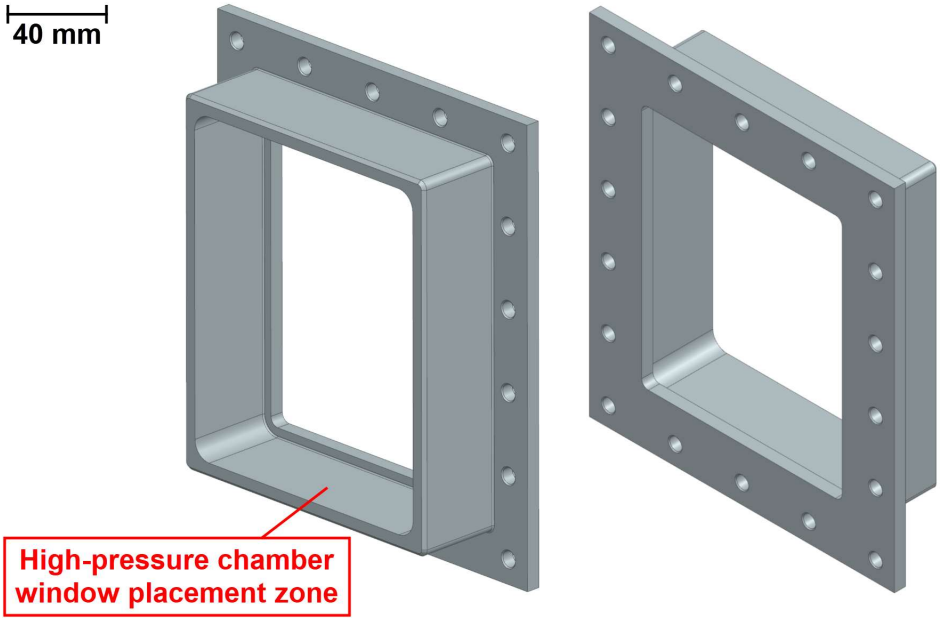

Figure 2.17. High-pressure chamber window holder (back and front views).

2.4.12. Gaskets

Gaskets are used to handle leakage problems between flange faces on test setup assemblies given in Figures 2.4 and 2.6. Two different dimensional gaskets were designed. One design (plenum chamber flange gasket) is used between the flange faces of the blind flange and plenum chamber assembly and between the flange faces of the plenum chamber assembly and preliminary acceleration section. The other design (high-pressure chamber flange gasket) is used between flange faces of the preliminary acceleration section and high-pressure chamber assemblies. The material of gaskets was chosen as graphite since it is durable at high temperatures and has good leakage prevention characteristics.

The plenum chamber flange gasket is given in Figure 2.18. Its dimensions are 218 mm (outer diameter), 169 mm (inner diameter), and 1.5 mm (thickness).

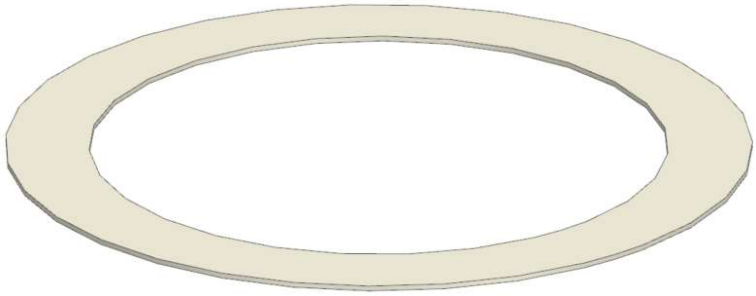

Figure 2.18. Plenum chamber flange gasket.

The high-pressure chamber flange gasket is given in Figure 2.19. Its dimensions are 340 mm (outer diameter), 207 mm (inner diameter), and 1.5 mm (thickness). It also has eight holes whose diameters are 22 mm diameter for screw passages of flange.

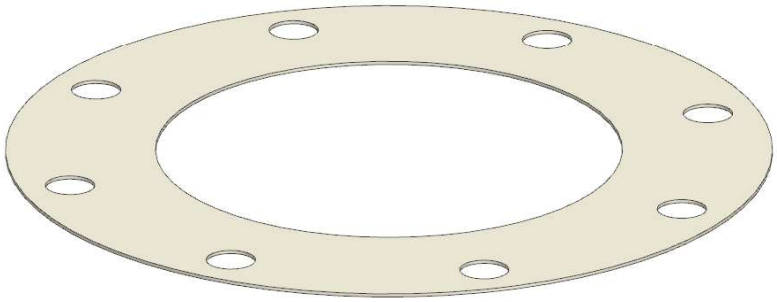

Figure 2.19. High-pressure chamber flange gasket.

2.5. CFD Analysis

Before starting the production process of the parts, the setup was analyzed with the help of computational fluid dynamic (CFD) analysis to check whether there was any problem with the setup, such as flow uniformity or separation problems, by checking the pressure, velocity or temperature results of the analysis or any other unknown issues. It is the ultimate purpose of the analysis. Then, the production processes were started. Therefore, in this section, governing equations used in the CFD analysis of the test setup, and numerical procedures are presented, and the CFD results' details are given in the "Results and Discussion" section. The simulations were done as single-phase analysis, and

only crossflow conditions were checked using ANSYS Fluent. Moreover, heat transfer between the setup and environment was not considered and ignored in the analysis since the temperature of the crossflow waits to be stabilized before capturing the data while conducting the tests, and then tests are performed. The temperature stabilization details are given in the “Results and Discussion” section. The software versions used in the simulations are provided in the following sections.

2.5.1. Governing Equations and Turbulence Model

Since the flow is mildly compressible, the compressible single-phase CFD analysis was done using ANSYS Fluent. Therefore, mass and momentum conversation equations, equation of state, and turbulence model equations had to be solved or calculated, and since the flow is compressible, the energy equation was also solved [63]. The governing equations used by ANSYS Fluent for the analysis are given below. These equations are transient. In the current case, the analysis was steady; therefore, the software dropped out the time-dependent parts of the equations for the analysis.

The mass conversation equation is given in Equation 2.19 [63].

$$\frac{\partial \rho}{\partial t} + \nabla \cdot (\rho \vec{v}) = S_m \tag{2.19}$$

where S_m is the mass source term [63]. The mass source term is zero since the current analysis is single-phase, and there is no chemical reaction.

The momentum conversation equation is given in Equation 2.20 [63].

$$\frac{\partial}{\partial t}(\rho\vec{v}) + \nabla \cdot (\rho\vec{v}\vec{v}) = -\nabla p + \nabla \cdot (\bar{\bar{\tau}}) + \rho\vec{g} + \vec{F} \tag{2.20}$$

where $\rho\vec{g}$ and $\vec{F}$ gravitational and external body forces, and $\bar{\bar{\tau}}$ is the stress tensor [63]. The stress tensor is given in Equation 2.21 [63].

$$\bar{\bar{\tau}} = \mu\left[(\nabla\vec{v} + \nabla\vec{v}^T) - \frac{2}{3}\nabla \cdot \vec{v}I\right] \tag{2.21}$$

The equation of state for the compressible flow is given in Equation 2.22 [63].

$$\rho = \frac{p_{op} + p}{\frac{R_u}{M_w}T} \tag{2.22}$$

where p_{op} is the operating pressure [63] and it was set to zero for the analysis.

The energy conversation equation is given in Equation 2.23 [63].

$$\begin{aligned}\frac{\partial}{\partial t}\left(\rho\left(e + \frac{v^2}{2}\right) + \nabla \cdot \left(\rho v\left(h + \frac{v^2}{2}\right)\right)\right) \\ = \nabla \cdot \left(k_{eff}\nabla T - \sum_i h_j\vec{J}_j + \left(\bar{\bar{\tau}}_{eff} \cdot \vec{v}\right)\right) + S_h\end{aligned} \tag{2.23}$$

The realizable k-ε model was used in ANSYS Fluent to model the turbulence in analysis. ANSYS Fluent uses the following equations for the model.

The transport equations for the model are given in Equations 2.24 and 2.25 [63].

$$\frac{\partial}{\partial t}(\rho k) + \frac{\partial}{\partial x_j}(\rho k u_j) = \frac{\partial}{\partial x_j}\left[\left(\mu + \frac{\mu_t}{\sigma_k}\right)\frac{\partial k}{\partial x_j}\right] + G_k + G_b - \rho\varepsilon - Y_M + S_k \qquad (2.24)$$

$$\frac{\partial}{\partial t}(\rho\varepsilon) + \frac{\partial}{\partial x_j}(\rho\varepsilon u_j) = \frac{\partial}{\partial x_j}\left[\left(\mu + \frac{\mu_t}{\sigma_\varepsilon}\right)\frac{\partial \varepsilon}{\partial x_j}\right] + \rho C_1 S\varepsilon - \rho C_2 \frac{\varepsilon^2}{k + \sqrt{\nu\varepsilon}} + C_{1\varepsilon}\frac{\varepsilon}{k}C_{3\varepsilon}G_b + S_\varepsilon \qquad (2.25)$$

Coefficient C_1 is found in Equation 2.25 by using the relations given in Equation 2.26 [63].

$$C_1 = max\left[0.43, \frac{\eta}{\eta + 5}\right] \ , \qquad \eta = S\frac{k}{\varepsilon} \ , \qquad S = \sqrt{2S_{ij}S_{ij}} \qquad (2.26)$$

where in Equations 2.24-2.26 [63], k, ε and μ_t represent turbulence kinetic energy, its dissipation rate, and turbulent viscosity, respectively. G_k and G_b are the generation of turbulence kinetic energy due to the mean velocity gradients and buoyancy. Y_M is the contribution of the fluctuating dilatation in compressible turbulence to the overall dissipation rate. S_k and S_ε are user-defined source terms. $C_{1\varepsilon}$, C_2 and C_3 are model constants. σ_k and σ_ε are the turbulent Prandtl numbers for k and ε, respectively.

The turbulent viscosity is modeled using the Equations 2.27 [63].

$$\mu_t = \rho C_\mu \frac{k^2}{\varepsilon} \tag{2.27}$$

where C_μ is calculated by Equations 2.28-2.31 [63].

$$C_\mu = \frac{1}{A_0 + A_s \frac{kU^*}{\varepsilon}} \tag{2.28}$$

$$U^* = \sqrt{S_{ij}S_{ij} + \widetilde{\Omega}_{ij}\widetilde{\Omega}_{ij}} \tag{2.29}$$

$$\widetilde{\Omega}_{ij} = \Omega_{ij} - 2\varepsilon_{ijk}\omega_k \tag{2.30}$$

$$\Omega_{ij} = \overline{\Omega_{ij}} - \varepsilon_{ijk}\omega_k \tag{2.31}$$

where $\overline{\Omega_{ij}}$ is the mean rate of rotation tensor viewed in a moving reference frame with the angular velocity ω_k [63]. A_0 and A_s are the model constants [63].

2.5.2. Geometry and Numerics

The analysis was done between crossflow inlet sections on the plenum chamber assembly and test section outlet on the test section; other parts were not considered. These parts are enough to analyze, and the flow after the test section is not essential to check with CFD for the production process. This simplification also had to be done to reduce computational cost since the whole setup is 1.4 m long. There is also a half symmetry condition on the test setup for CFD analysis, and this symmetry condition was also used to make computational cost less.

Therefore, the cleaned flow model for CFD can be seen in Figure 2.20. The model has two inlets, an outlet, and a symmetry plane, and the remaining faces are walls. Crossflow gas enters the test system via two inlets given in Figure 2.20, then is stored in the plenum chamber by passing through uniformity parts. Details can be seen in Figures 2.22, 2.25, and 2.26. Then, it goes to the preliminary acceleration and test section. Finally, it leaves the test section via the outlet given in Figure 2.20.

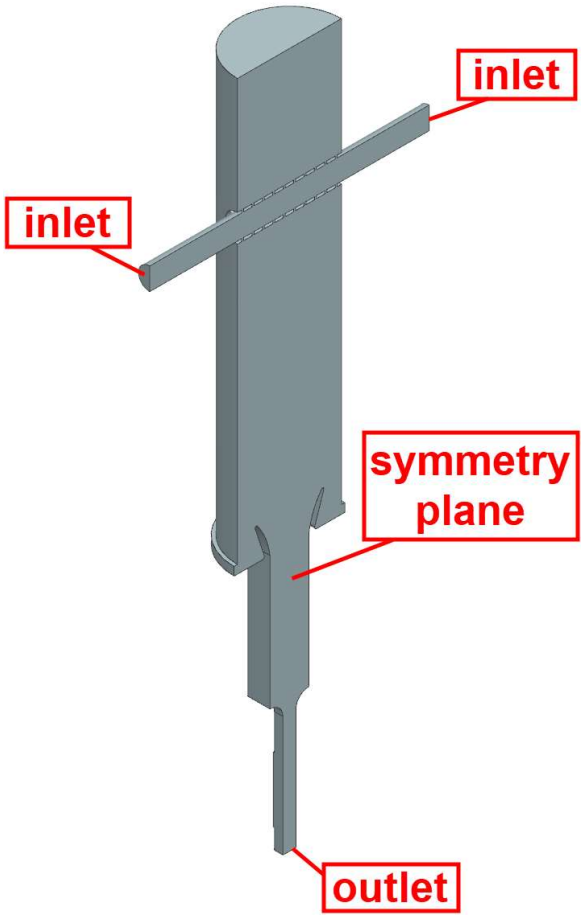

Figure 2.20. The geometry of the test system used in CFD analysis.

The settings of the model for analysis in ANSYS Fluent are given in Table 2.8.

Table 2.8. Settings of model for CFD analysis in Fluent.

Setup	General	Energy	On	
		Viscous	Model	k-epsilon (2 eqn.)
			k-epsilon Model	Realizable
			Near-Wall Treatment	Scalable Wall Functions
Solution	Methods	Pressure-Velocity Coupling	Scheme	Coupled
		Spatial Discretization	Gradient	Least Squares Cell-Based
			Pressure	Second Order
			Density	Second Order Upwind
			Momentum	Second Order Upwind
			Turbulent Kinetic Energy	Second Order Upwind
			Turbulent Dissipation Rate	Second Order Upwind
			Energy	Second Order Upwind

Analysis was done for three cases of crossflow conditions, as shown in Table 2.3. The case selection was done regarding mass flow rate to choose between minimum and maximum values as well as considering temperature and pressure. The chosen conditions are given in Table 2.9. Air was used for every analysis.

Table 2.9. CFD analysis conditions.

Mach Number	**Total Pressure [bar]**	**Static Pressure [bar]**	**Total Temperature [K]**	**Mass Flow rate [g/s]**
0.1	2.00	1.99	493.15	38
0.3	1.41	1.32	393.15	85
0.4	1.10	0.99	673.15	65

2.5.3. Mesh Sensitivity Analysis

Mesh sensitivity had to be checked for CFD to ensure that the CFD analysis results were independent of mesh quantity. Therefore, in this section, mesh sensitivity analysis is given. Four different quantity meshes were created: coarse, medium, fine, and very fine. To be sure of mesh independence, it was tried to be quantity of each mesh four times in each case, such as if coarse mesh has x mesh, medium, fine, and very fine mesh have 4x, 16x, and 64x mesh, respectively. The Fluent Mesher was used to create mesh. Information about the created mesh can be found in Table 2.10. Also, a mesh comparison is given in Figure 2.21.

Table 2.10. Mesh data.

			Volume Mesh				
	Surface Mesh					Boundary Layer	
Name	Quantity	Maximum Skewness	Quantity	Maximum Skewness	Type	First Layer Thickness [mm]	Layer Quantity
Coarse	48427	0.75795970	693111	0.89954402	Tetra	0.01	13
Medium	147778	0.72324691	2814228	0.89852268	Tetra	0.01	15
Fine	460067	0.72254924	10277313	0.89928899	Tetra	0.01	15
Very Fine	1477717	0.69927105	39539822	0.88761659	Tetra	0.01	15

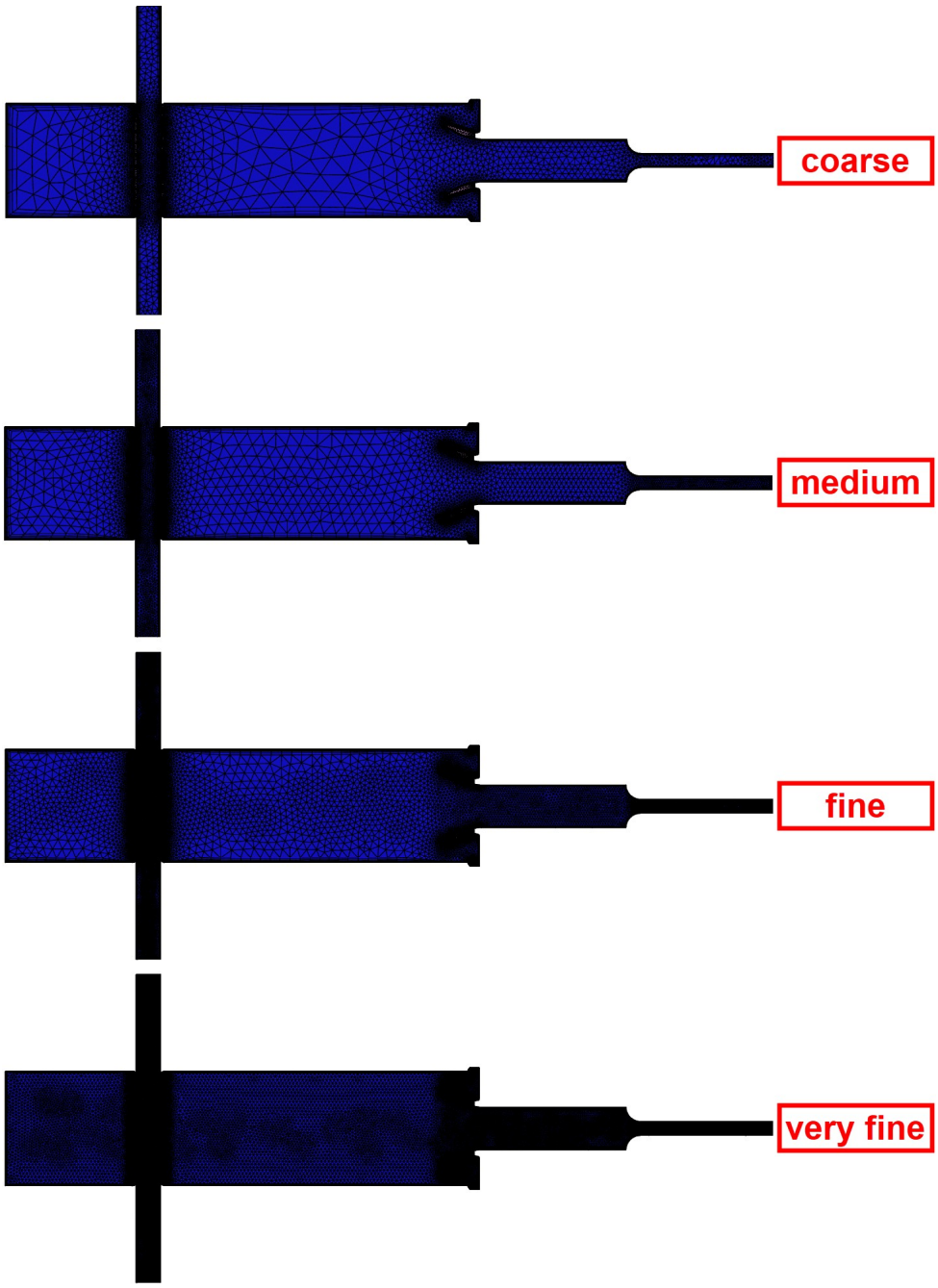

Figure 2.21. Mesh comparison.

Mesh sensitivity analysis was done for the case of 85 g/s flow rate given in Table 2.9. Since the half symmetry condition was used, the flow rate for inlet had to be divided by half. Also, the setup has two inlets, so the flow rate had to be divided by 4 to find the flow rate boundary condition for one inlet. In conclusion, the boundary conditions are given in Table 2.11.

Table 2.11. Mesh sensitivity analysis boundary condition.

Inlet (for each inlet given in Figure 2.20)	Mass Flow rate [g/s]	21.25
	Supersonic / Initial Gauge Pressure [bar]	3
	Total Temperature [K]	393.15
Outlet	Gauge Pressure [bar]	1.32
	Total Temperature [K]	393.15

Analysis was run using ANSYS Fluent 2022 R1 and 2023 R1 for meshes except for very fine mesh and very fine mesh, respectively. To compare the results for each mesh, the results in a plane passing through the injector, a parallel plane 115 mm from the outlet, and a line submerged 0.5 mm from the symmetry plane were checked. The plane and line can be seen in Figure 2.22.

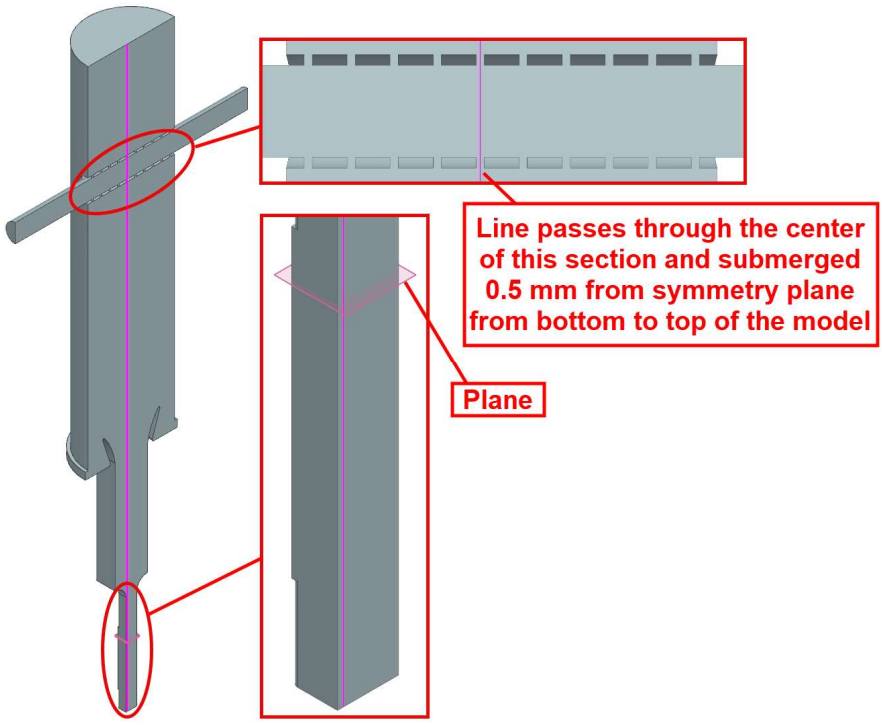

Figure 2.22. Control line and plane for results of mesh sensitivity analysis.

Mass-weighted average static pressure for each mesh on the plane given in Figure 2.22 and static pressure for each mesh on nodes passing through the line

shown in Figure 2.22 were checked and are presented in Figures 2.23 and 2.24. As shown in Figures 2.23 and 2.24, identical results were found nearly everywhere for each mesh, and it can be said that coarse mesh is not coarse enough to compare with other meshes. The reason for this situation is the usage of Fluent Mesher. Fluent Mesher creates meshes using the whole flow body, and when it was tried to mesh quantity below 600k to make the mesh coarser to see the difference with other meshes, Fluent Mesher gave an error and could not create a mesh. Therefore, the coarser mesh with mesh quantity below 600k could not be made with Fluent Mesher, and it was said that the solution was independent of the mesh. Moreover, as shown in Figure 2.24, there is some difference in static pressure in some sections, but other sections have similar results. For the section that has differences, it can be said that mesh is coarse for coarse mesh and affects the result, and this is on the small cylindrical section of the geometry (3 mm diameter). As a result, the fine mesh was chosen as the mesh for the solution since there was enough computational power for this quantity.

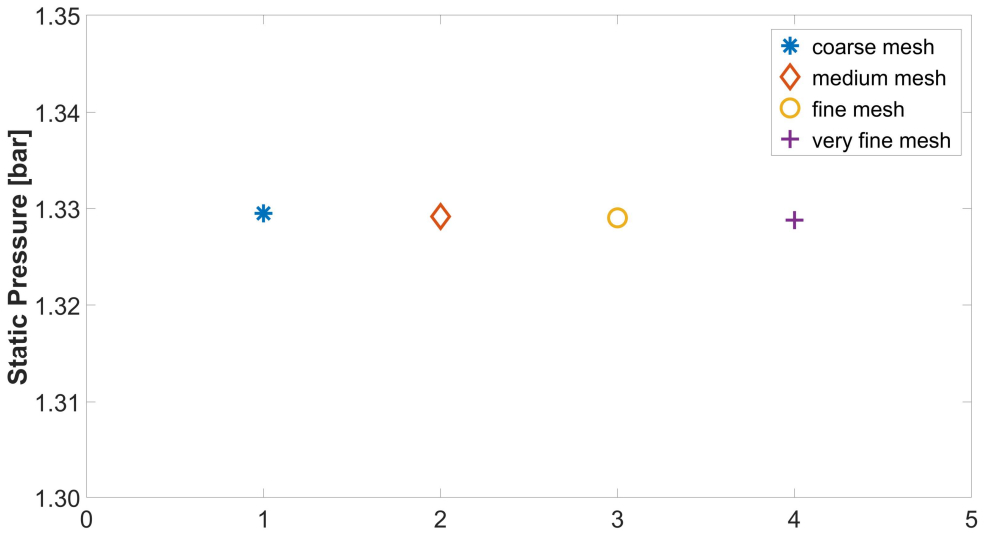

Figure 2.23. Mass-weighted average static pressure on the plane given in Figure 2.22 for analysis done using coarse, medium, fine, and very fine meshes.

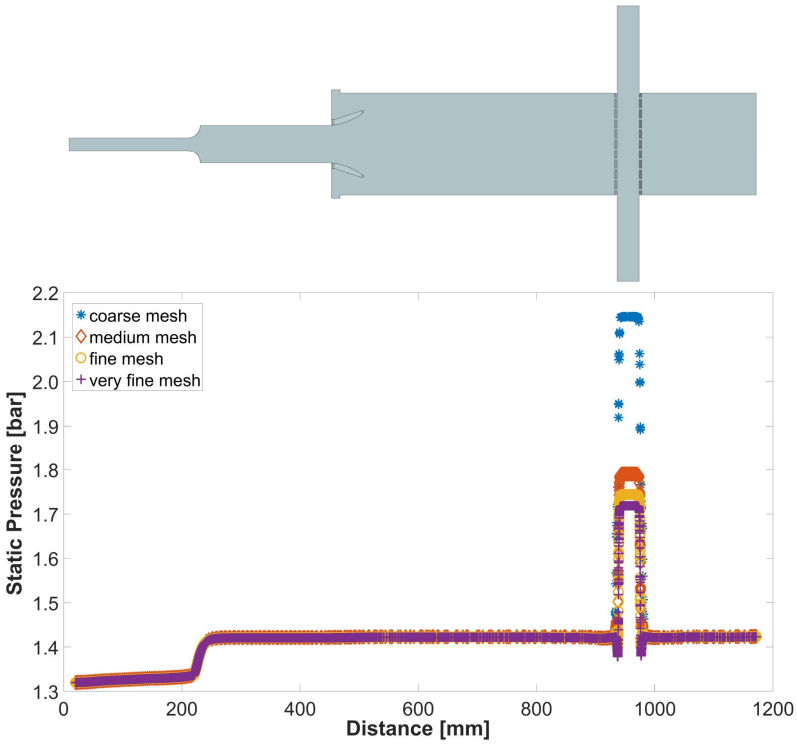

Figure 2.24. Static pressure on nodes passing through the line given in Figure 2.22 for analysis done using coarse, medium, fine, and very fine meshes.

Figures 2.25 and 2.26 show details of the fine mesh chosen for the analysis. Figure 2.26 shows a cross-sectional view of the fine mesh passing through a plane given by Figure 2.25.

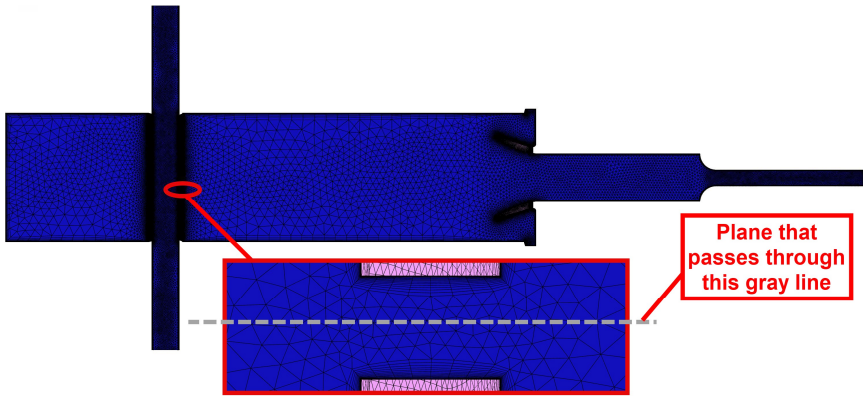

Figure 2.25. View of fine mesh and the plane for the cross-sectional view of some part of it.

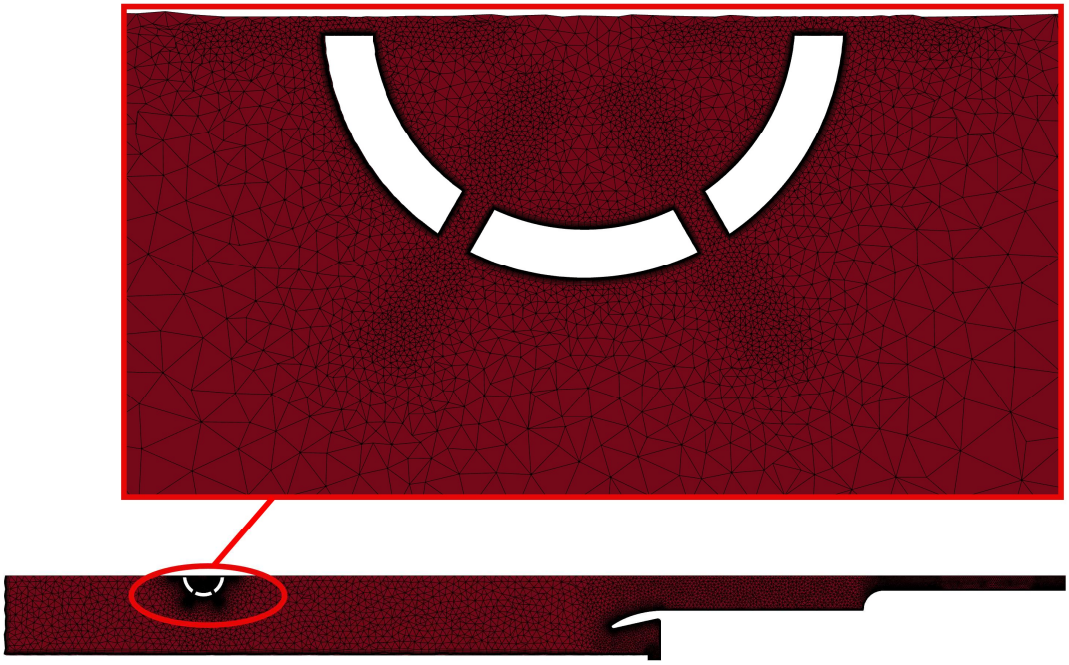

Figure 2.26. The cross-sectional view of the fine mesh that passes through the plane given in Figure 2.25.

The results of the CFD analysis are given in the "Results and Discussion" section. Based on the CFD analysis results, it was concluded that there was not any problem with the setup and that the designed setup was ready for production.

2.6. Production, Endurance, and Leakage Tests of the Setup

All parts of the designed test setup were either produced or taken off-the-shelf, and the setup was assembled at the production facility. Then, endurance and leakage tests were carried out at 10 bar by closing the related open section of the setup with plugs or blind flanges and it was seen that the produced setup is ready for use. The photo of produced test setup and test process are given in Figure 2.27.

Figure 2.27. View of produced test setup and testing process (endurance and leakage).

2.7. Integration of Test Setup to The Test Facility

The test setup was assembled and integrated into the test facility as the final part of the section. Its view and sub-parts can be seen in Figure 2.28 and Figures A1.21-A1.23 of Appendix 1.

Figure 2.28. Integrated shadowgraphy test setup assembly at the test facility at TÜBİTAK SAGE.

As Figure 2.28 shows, the plenum and some other parts are covered with insulation material to decrease the heat loss between the heater and the test section.

3. THEORY AND WORKING PRINCIPLE OF PHASE DOPPLER PARTICLE ANALYZER

This section gives the theory and working principle of the Phase Doppler Particle Analyzer (PDPA).

PDPA is a device for measuring particle size and velocity simultaneously. TÜBİTAK SAGE has TSI two-component PDPA System. It has green (λ = 514.5 nm) and blue (λ = 488 nm) laser beams. The green laser measures particle axial velocity and size, and the blue laser measures particle radial velocity. Its photos are given in Figure 3.1.

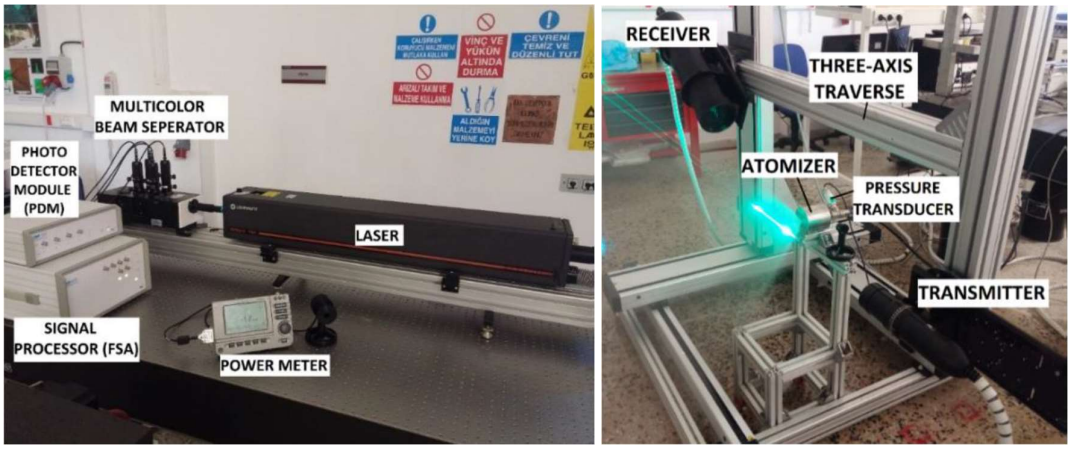

Figure 3.1. TSI two-component PDPA System at test facility at TÜBİTAK SAGE [64].

As can be seen in Figure 3.1, it consists of a 5-watt argon-ion laser that creates a single beam laser, a multicolor beam separator that separates the single laser beam coming from laser to 4 laser beams, which 2 of them are green (shifted and unshifted) and remaining 2 of them are blue (shifted and unshifted). Then, after beams are transmitted to the transmitter, they exit via optics, and all of them are focused on the focal point of the transmitter. This is where measurement takes place, and it is known as measurement/probe volume. Measurement volume and schematic view of the transmission side of PDPA can be seen in Figure 3.2.

Focused beams create bright and dark fringes in the measurement volume. It can be seen in Figure 3.3.

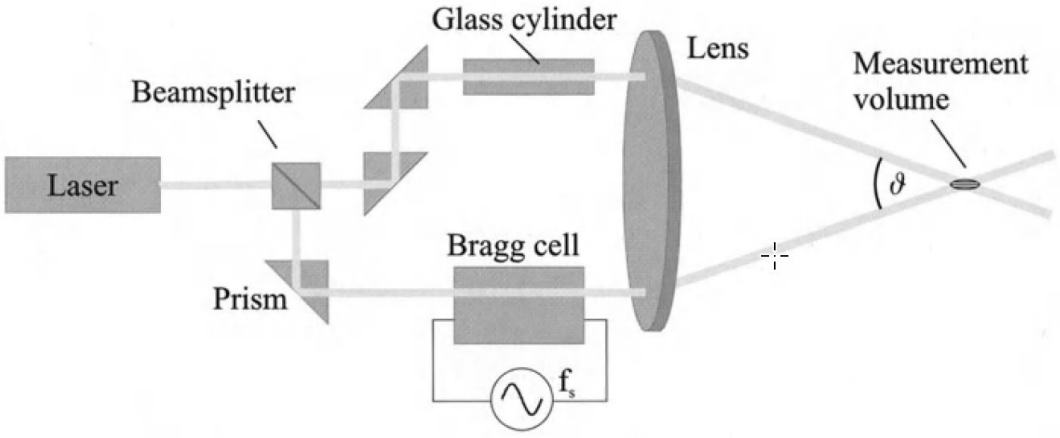

Figure 3.2. Schematic view of the transmission side of PDPA [65].

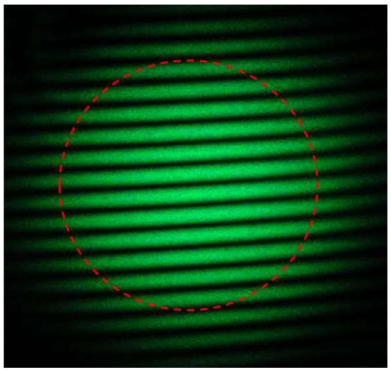

Figure 3.3. Measurement volume [66].

A particle passing through measurement volume scatters the light while passing through a bright fringe. Then, the photodetectors capture the scattered light in the receiver, and the detectors send the related signals to the photodetector module. The photodetector module creates an electrical signal by converting the signal coming from the photodetector. It sends the electrical signal to the signal processor, which filters and sends the signal to the computer, and the user can analyze data on the computer. The underlying theory is explained below.

The particle's velocity is determined using Doppler shift frequency captured by PDPA. When a particle passes through the bright fringe in the measurement volume, the light is scattered, and this scattering causes a frequency shift in beams (green and blue) in the measurement volume. This frequency shift is known as Doppler shift frequency, and photodetectors in the receiver detect it. The velocity is determined by using Doppler shift frequency via Equation 3.1 [65].

$$v = \frac{(f - f_0)\lambda}{2\sin(\vartheta/2)} \tag{3.1}$$

where, v is the related velocity component (axial velocity for green beam and radial velocity for blue beam), f is Doppler shift frequency measured by PDPA, f_0 is the frequency of the shifted beam coming from the transmitter, λ is the wavelength of the beam and ϑ is the intersection angle of the shifted and unshifted beams for exact color.

Using Equation 3.1, the magnitude and sign of the related velocity component are found. If the particle is stationary, the Doppler shift frequency detected by the photodetector is equal to f_0, and if the particle is moving in the positive direction, it causes a burst in Doppler shift frequency and makes it bigger than f_0. Therefore, the sign of the velocity is found to be positive. If it is moving in the negative direction, the Doppler shift frequency becomes smaller than f_0 and the sign of the velocity becomes negative. This is the reason why one of the beams shifted for each color.

On the other hand, the size measurement is done by using scattering mechanisms, such as reflection and 1st or 2nd-order refractions. There are also other components of the scattering mechanism, but they are not considered in PDPA since their intensity is not high [65]. Therefore, the most dominant modes of scattering for PDPA are reflection, 1st and 2nd order refractions [65]. The schematic view of scattering mechanisms can be seen in Figure 3.4.

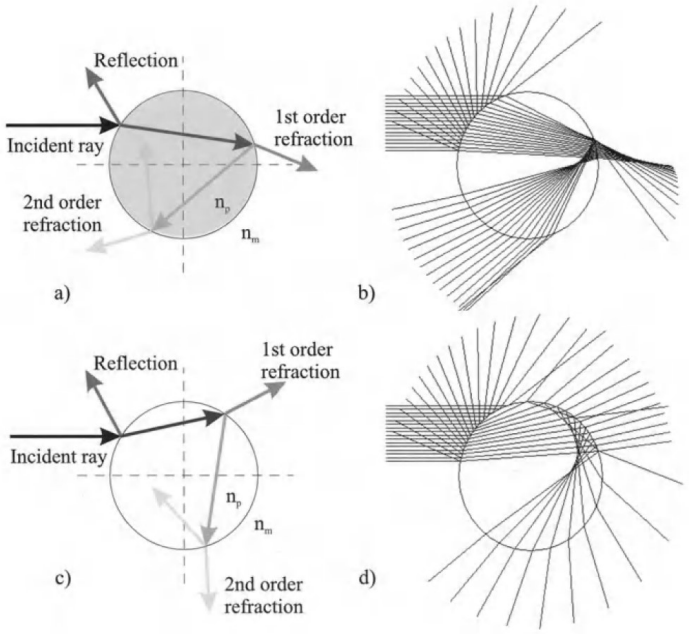

Figure 3.4. Schematic view of light scattering by droplets ($n_p > n_m$) and bubbles ($n_p < n_m$); general definitions and calculations with ray tracing software for a water droplet in air (a, b) and for an air bubble in water (c, d) [65].

The scattering mechanism depends on the intensity of the scattered light, and the intensity depends on the relative refractive index [65] and the intensity is not uniform in every direction. Therefore, the receiver's position must be chosen carefully to make one of the scattering modes dominant. The related angles can be seen in Figure 3.5.

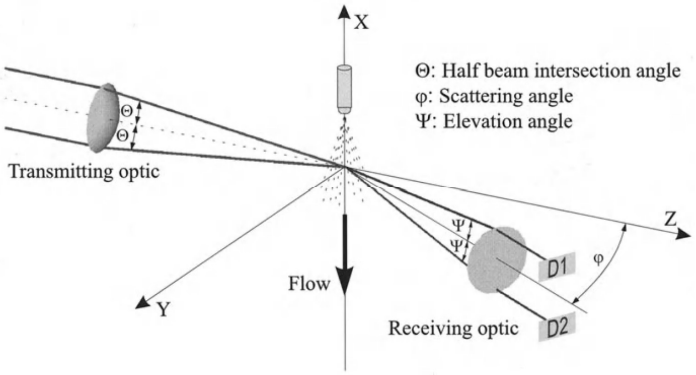

Figure 3.5. Schematic view of Phase Doppler measurement setup [65].

The particle size is measured when the related particle passes through the measurement volume and scatters the light. When it is scattered, the photodetectors in the receiver detect the phase difference in the Doppler burst. Using the phase difference value, the size of the particle can be calculated using Equations 3.2 and 3.3 for reflection-dominated mode and 1st-order refraction-dominated mode, respectively [65].

$$\Phi = \frac{2\pi d_p}{\lambda} \frac{\sin\Theta \sin\Psi}{\sqrt{2(1-q_c)}} \; ; \quad \sin\Theta \sin\Psi \ll q_c \tag{3.2}$$

where, Φ is the phase difference, d_p is particle diameter, λ is wavelength, Θ is half beam intersection angle, Ψ is elevation angle, q_c is coefficient and is calculated using Equation 3.4.

$$\Phi = \frac{-2\pi d_p}{\lambda} \frac{m \sin\Theta \sin\Psi}{\sqrt{2(1+q_c)\left(1+m^2-m\sqrt{2(1+q_c)}\right)}} \; ; \quad m > 1 \tag{3.3}$$

where, m is the relative refractive index.

$$q_c = \cos\Theta \cos\Psi \cos\varphi \tag{3.4}$$

where, φ is the scattering angle.

TSI's operating software (Flowsizer) of the PDPA system finds the scattering angle for the related measurements and warns the user to choose the angle correctly. The program lets the user choose by asking about the particles' relative

refractive index and attenuation level. The attenuation level can be selected from Table 3.1 for the related attenuation level coefficient.

Table 3.1. Attenuation level [67].

Attenuation Level	C_{level}
1	< 0.005
2	0.005 – 0.05
3	0.05 – 500
4	500 – 4000
5	> 4000

$$C_{level} = \alpha d_{pmax}/1000 \tag{3.4}$$

where C_{level} is the coefficient to find the attenuation level of the particle, α is the attenuation coefficient of the particle in mm^{-1} and d_{pmax} is the maximum expected particle diameter in μm.

In the current study, the particles are liquid droplets of the fuel JP-10, and to find its attenuation level, the attenuation coefficient of JP-10 was required, which was not available in the literature. Therefore, its attenuation coefficient was measured and found to be 0.0115 mm^{-1} for green and blue laser beams. The details of the measurement can be found in Section 4.3. Also, the expected maximum particle diameter was required to find the attenuation level, and it was assumed to be 400 μm. However, the assumed maximum diameter is high; it was considered a high value since it is unknown. Thus, its attenuation level was found to be 1.

After finding the attenuation level, the applicable scattering domains needed to be found. It was found by considering the relative refractive index, which is the

ratio of the particle's refractive index to the refractive index of the ambient where particles are created. Therefore, for the current study, it is the ratio of refractive index of JP-10 to air and its value is 1.4878 [68]. The scattering domains for related refractive index are 12, 11, 10, 9, and 13 from Figure 3.6. One of them is chosen by considering polarization in a beam that is used to make one of the scattering mechanisms dominant, which is given below.

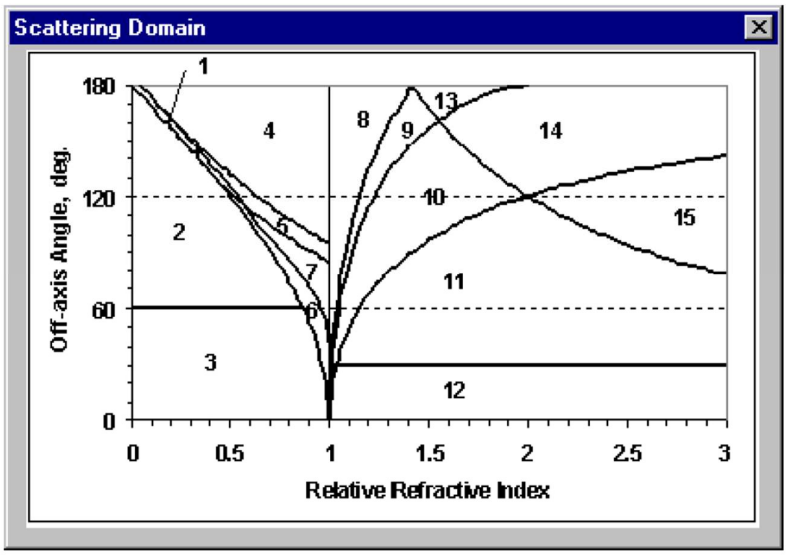

Figure 3.6. Scattering domain and off-axis angle (scattering angle) [67].

The dominant modes for related attenuation levels and domains are given in Figure 3.7. There are two different polarization methods: polarization in the beam plane and polarization perpendicular to the beam plane. The attenuation level was found to be 1, and applicable domains were seen as 12, 11, 10, 9, and 13. By checking Figure 3.7, the polarization in the beam plane is not applicable for attenuation level 1 due to no dominant mechanism for domains 12, 11, 10, 9, and 13. Therefore, polarization perpendicular to the beam plane is used, and the only applicable domain for the case is 11. Thus, an off-axis angle (scattering angle) in domain 11 can be chosen from Figure 3.6. Hence, the scattering angle is selected as 30 degrees by analyzing domain 11 in Figure 3.6. The reason for the decision is that in another setup at the test facility, 30 degrees is used as a scattering angle. It is known that the successful measurement can be achieved, PDPA is

ready for use, and if the angle is chosen as a different value rather than 30 degrees, the receiver and test setup cannot be easily integrated into the test facility. As a result, a 30-degree scattering angle was chosen for the test setup of PDPA, and the designs were completed with this angle.

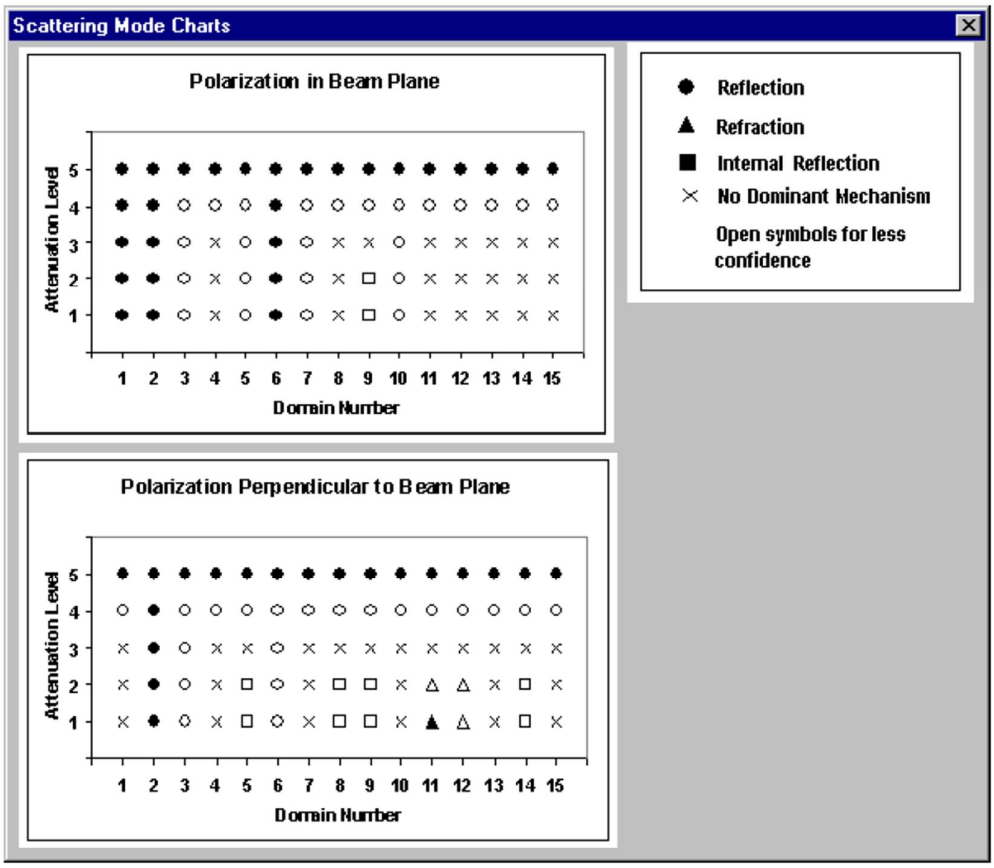

Figure 3.7. Feasible scattering modes for various domains, attenuation levels, and polarization [67].

4. RESULTS AND DISCUSSION

This section provides the results of CFD analysis, injector discharge coefficient measurements, JP-10 attenuation coefficient measurements, and liquid jet penetration measurements.

4.1. Results of CFD Analysis

The analysis using fine mesh was run on ANSYS Fluent 2021 R1 for the cases in Table 2.9. The mass-weighted average of total and static pressures, Mach number, and total and static temperatures on the plane, given in Figure 2.22, is compared with the results of 1-D isentropic equations in Section 2.2, which are given in Table 4.1. As can be seen in Table 4.1, similar results were found.

Table 4.1. Comparison of 1-D equation and CFD results.

	Case-1		Case-2		Case-3	
	1-D Equation	CFD	1-D Equation	CFD	1-D Equation	CFD
Total Pressure [bar]	2.00	2.01	1.41	1.42	1.10	1.12
Static Pressure [bar]	1.99	1.99	1.32	1.33	0.99	1.00
Mach Number	0.1	0.1	0.3	0.3	0.4	0.4
Total Temperature [K]	493.15	493.15	393.15	393.15	673.15	673.15
Static Temperature [K]	492.17	492.12	386.20	386.06	652.28	652.36

Also, the contours of the velocity magnitude on the plane given in Figure 2.22 and the contours of the total pressure and velocity magnitude on the symmetry plane were investigated and presented in Figures 4.1-4.3. As seen in the figures, there is no flow separation in the geometry.

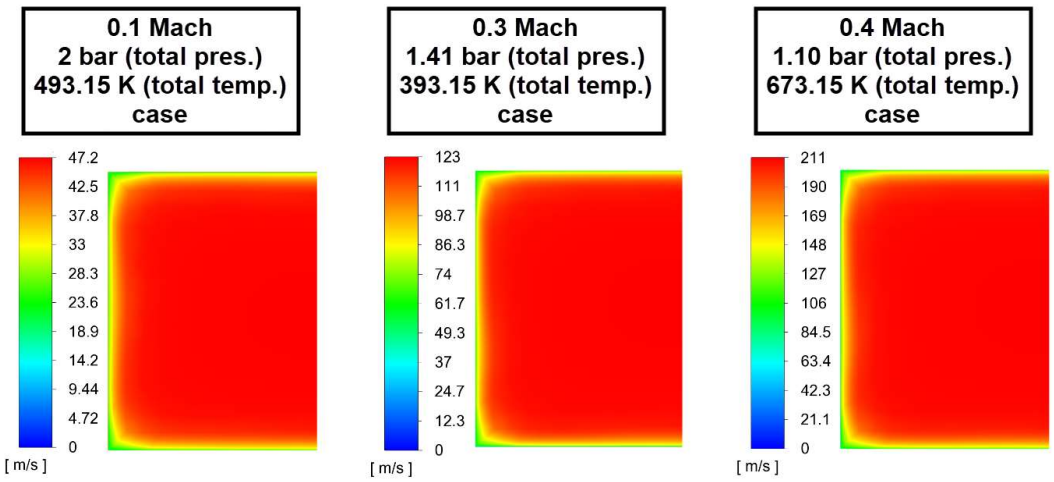

Figure 4.1. The contours of the velocity magnitude on the plane shown in Figure 2.22 for cases given in Table 2.9.

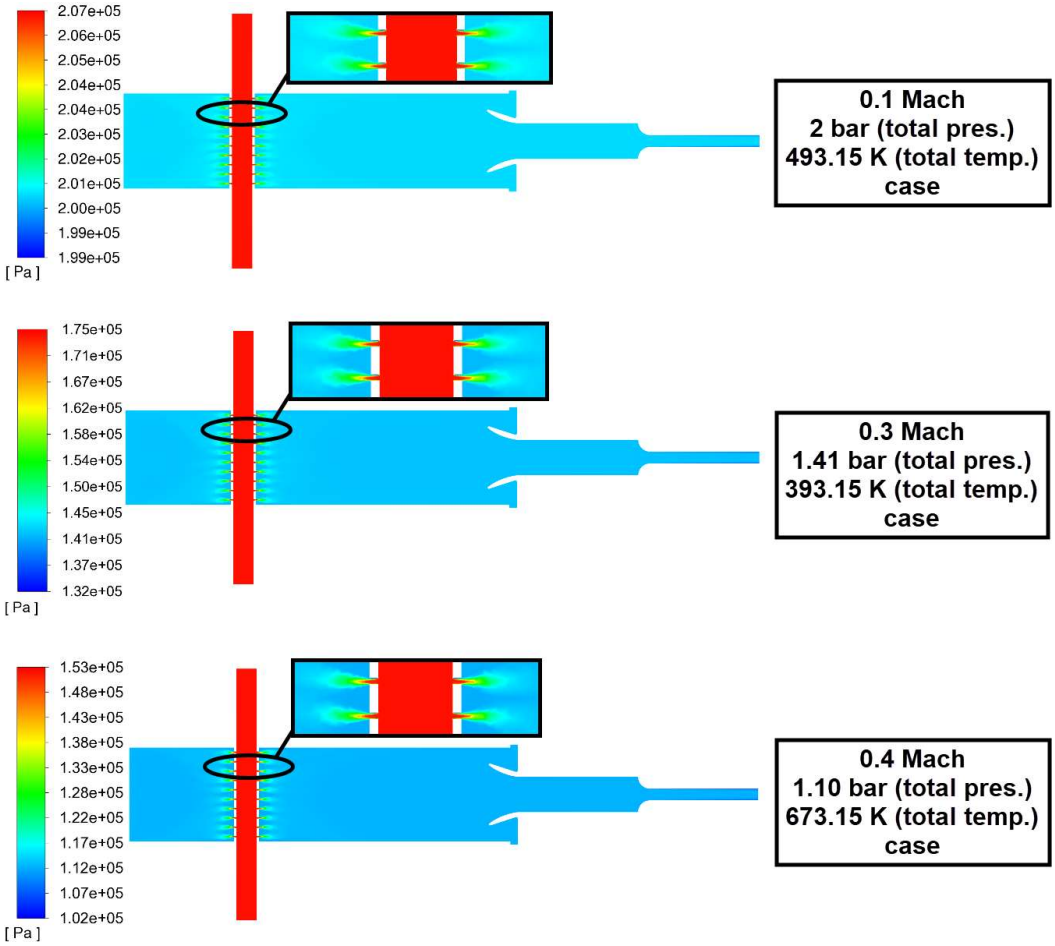

Figure 4.2. The contours of the total pressure on the symmetry plane for cases given in Table 2.9.

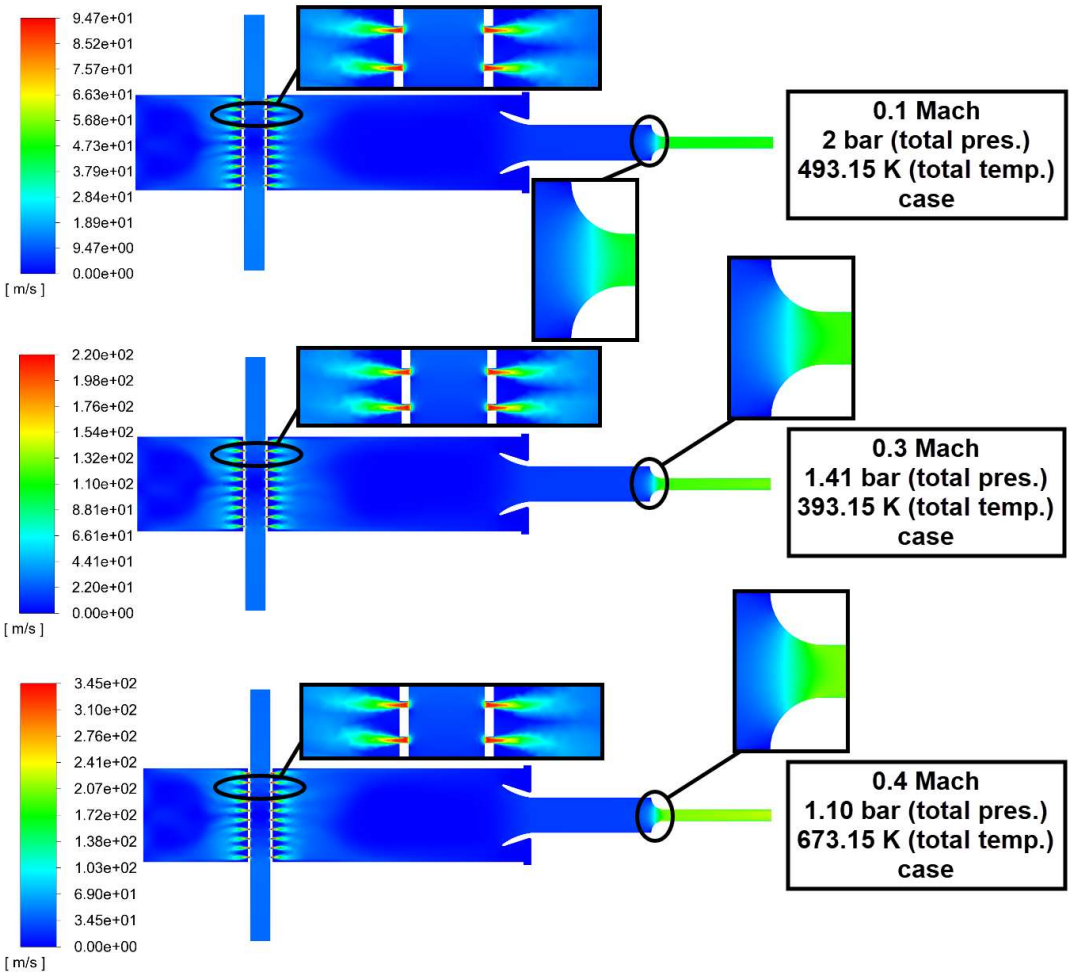

Figure 4.3. The contours of the velocity magnitude on the symmetry plane for cases given in Table 2.9.

4.2. Discharge Coefficient Measurement of Injectors

Ten injectors were produced: three with a 0.4 mm exit orifice diameter, three with a 0.5 mm exit orifice diameter, and four with a 0.6 mm exit orifice diameter. This section describes the measurement procedure for the discharge coefficients of the injectors and gives the results. Measured orifice diameters are also presented in this section.

The mass flow rate through an orifice can be calculated using Equation 4.1.

$$\dot{m} = C_D A_2 \left(2\rho(P_1 - P_2)\right)^{1/2} \tag{4.1}$$

The indices in Equation 4.1 were modified for the injector dynamics, and the modified version is given in Equation 4.2.

$$\dot{m}_j = C_D A_{exit} \left(2\rho_j \left(P_{flow} - P_{amb}\right)\right)^{1/2} \tag{4.2}$$

where $\dot{m}_j$ is the mass flow rate of the jet through the injector, C_D is the discharge coefficient of the injector, A_{exit} is the exit area of the injector, ρ_j is the density of the jet through the injector, P_{flow} is the pressure of the flow and P_{amb} is the pressure of the ambient. Equation 4.2 can be rearranged to solve for the discharge coefficient:

$$C_D = \frac{\dot{m}_j}{A_{exit}} \left(2\rho_j \left(P_{flow} - P_{amb}\right)\right)^{-1/2} \tag{4.3}$$

The term "$P_{flow} - P_{amb}$" in Equation 4.3 is called pressure loss in the injector and is denoted as "ΔP". The modified version of the Equation 4.3 is presented in the Equation 4.4.

$$C_D = \frac{\dot{m}_j}{A_{exit}} \left(2\rho_j \Delta P\right)^{-1/2} \tag{4.4}$$

In the discharge coefficient experiment, the mass flow rate through the injector, flow pressure, and ambient pressure for calculating the pressure drop through

the injector, and the temperature of the jet in the injector for the density calculation of the jet are measured to calculate the discharge coefficient.

The schematic view and the photos of the experimental test setup can be seen in Figures 4.4-4.7. The fuel supply tank is used to supply fuel (JP-10) to the pump, the pump pressurizes and adjusts the flow rate and transfers it to the injector, the pressure sensor between the pump and injector is used to measure the flow pressure, and fuel storage tank is used to store the fuel that exits the injector, pressure sensor for the ambient pressure is used to measure the ambient pressure and its inlet is open to the ambient, DAQ is data acquisition system and used to convert analog data to digital data and send digital data to the computer, the computer is used to collect data from the DAQ.

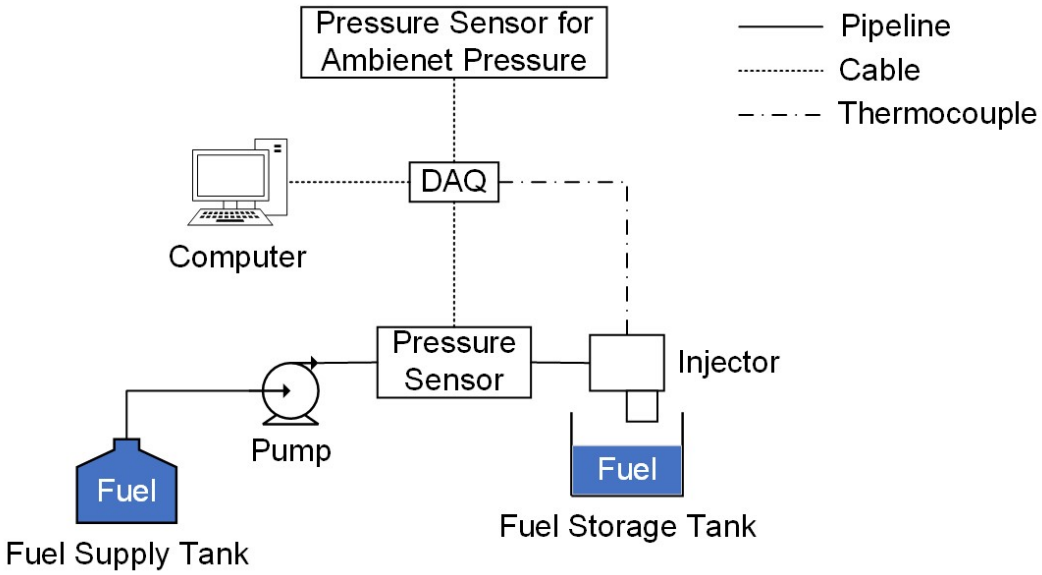

Figure 4.4. Schematic view of the discharge coefficient measurement test setup.

Figure 4.5 shows the tip of the thermocouple that measures the flow temperature through the injector. In order not to affect the flow in the injector, the tip is not fully submerged in the injector; it is submerged near the wall of the injector, which can be seen in Figure 4.5.

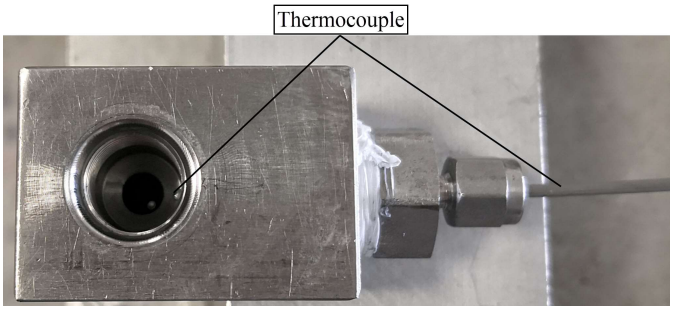

Figure 4.5. View of thermocouple inside the injector.

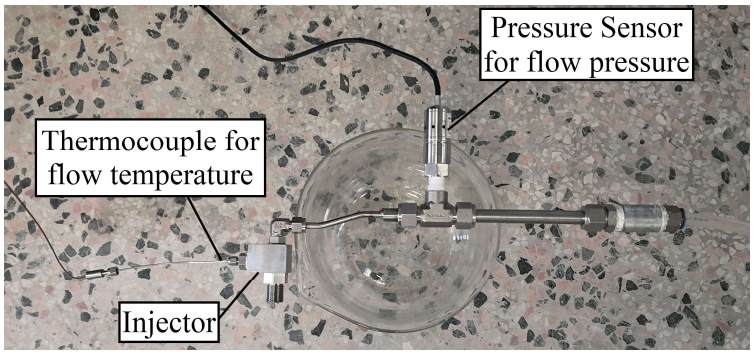

Figure 4.6. Injector and sensor part view of discharge coefficient measurement test setup.

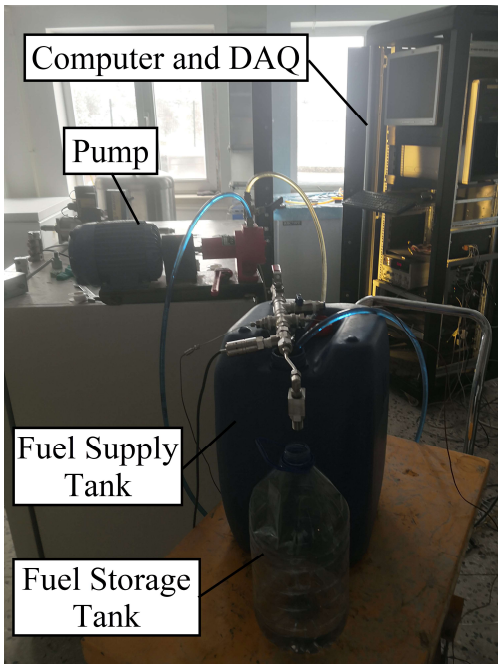

Figure 4.7. Discharge coefficient measurement test setup.

Before starting the discharge coefficient experiments, the injector was not connected to the setup given in Figure 4.7 to measure the pressure drop between the flow pressure measurement point and the pipe outlet. It was observed that the pressure loss is negligible between these points since the flow rate is too low, which is between 3 and 5 g/s. Therefore, it is assumed that pressure is only lost in the injector.

The test procedure is as follows:

1. Adjust the pump for the desired flow rate. (Note that the test is done at 3 g/s, 4 g/s, and 5 g/s fuel flow rates for each injector.)
2. Place the fuel storage tank on the scale and adjust it to zero at this position.
3. Place the fuel storage tank under the injector.
4. Power on the fuel pump and start recording the test duration, the fuel flow temperature, the fuel flow pressure, and the ambient pressure.
5. Continue the experiment for 30 seconds.
6. Power off the fuel pump and stop recording the test duration, the fuel flow temperature, the fuel flow pressure, and the ambient pressure.
7. Measure the mass of the fuel storage tank filled with the fuel and note it.
8. Repeat the experiment for each flow rate and injector.

After the experiment, the calculations were done using the Equations 4.5-4.13 and the test results. The results of the experiment are given next.

The mass flow rate of the jet through the injector is determined using:

$$\dot{m}_j = \frac{m_{fuel\ storage\ tank}}{t_{test}} \tag{4.5}$$

where $m_{fuel\ storage\ tank}$ is the mass of the fuel storage tank after the experiment and t_{test} is test duration.

The pressure drop in the injector is:

$$\Delta P = P_{flow} - P_{amb} \tag{4.6}$$

where P_{flow} and P_{amb} are the pressure of the flow and the ambient, respectively.

The standard deviation of the pressure drop can be calculated as:

$$S_{\Delta P} = \left(S_{P_{flow}}^2 + S_{P_{amb}}^2\right)^{1/2} \tag{4.7}$$

where $S_{P_{flow}}$ and $S_{P_{amb}}$ are the standard deviation of the flow pressure and the ambient pressure, respectively.

The reduced absolute temperature is given as [58]:

$$T_r = \frac{T_{flow}}{273.15} \tag{4.8}$$

where T_{flow} is the temperature of the flow.

$$S_{T_r} = \frac{S_{T_{flow}}}{273.15} \tag{4.9}$$

where S_{T_r} and $S_{T_{flow}}$ are standard deviations in the reduced absolute and flow temperatures, respectively.

$$\rho_j = a_0 + a_1 T_r + a_2 T_r^2 \tag{4.10}$$

where ρ_j is the density of the jet through the injector, a_0, a_1 and a_2 are parameters for density calculation [58]. The values and standard deviation of the parameters are given in Table 4.2.

Table 4.2. Parameter values and associated standard deviations for Equation 4.10 [58].

Parameter	Parameter Value	Standard Deviation
a_0	1153.0412	1.020
a_1	-192.47447	1.868
a_2	-9.3825928	0.8485

$$S_{\rho_j} = \left[S_{a_0}^2 + \left(a_1 T_r \left[\left(\frac{S_{a_1}}{a_1} \right)^2 + \left(\frac{S_{T_r}}{T_r} \right)^2 \right]^{1/2} \right)^2 + \left(a_2 T_r^2 \left[\left(\frac{S_{a_2}}{a_2} \right)^2 + \left(2\frac{S_{T_r}}{T_r} \right)^2 \right]^{1/2} \right)^2 \right]^{1/2} \tag{4.11}$$

where S_{ρ_j}, S_{a_0}, S_{a_1} and S_{a_2} are the standard deviations in the density of the jet through the injector and in the parameters for density calculation, respectively.

$$C_D = \frac{\dot{m}_j}{A_{exit}}\left(2\rho_j \Delta P\right)^{-1/2} \tag{4.12}$$

where C_D is the discharge coefficient of the injector.

$$S_{C_D} = C_D\left[\left(-\frac{1}{2}\frac{S_{\rho_j}}{\rho_j}\right)^2 + \left(-\frac{1}{2}\frac{S_{\Delta P}}{\Delta P}\right)^2\right]^{1/2} \tag{4.13}$$

where S_{C_D} is the standard deviation in the discharge coefficient.

The diameter of injectors is given in Table A1.14 of Appendix 1. Data taken during the discharge coefficient measurement experiment are given in Table A1.15 of Appendix 1.

Using the data in Tables A1.14 and A1.15 and Equations 4.5-4.13, the results in Table 4.3 were determined, and they are given below.

Table 4.3. Discharge coefficient experiment calculation results.

Part Number	A_0 [mm^2]	$\dot{m}_j$ [g/s]	ΔP [bar]	$S_{\Delta P}$ [bar]	T_r	S_{T_r} x10^{-5}	ρ_j [kg/m^3]	S_{ρ_j} [kg/m^3]	C_D	S_{C_D}
109665-R00-LS001_0001 (3 g/s experiment)	0.144	2.90	2.590	0.180	1.043	4.796	942.19	2.38	0.91	0.032
109665-R00-LS001_0001 (4 g/s experiment)	0.144	4.04	4.947	0.181	1.083	6.817	933.64	2.47	0.92	0.017
109665-R00-LS001_0001 (5 g/s experiment)	0.144	4.95	7.862	0.217	1.075	8.688	935.26	2.46	0.90	0.012
109665-R00-LS001_0002 (3 g/s experiment)	0.121	2.94	3.302	0.202	1.040	2.338	942.79	2.38	0.98	0.030

Table 4.3. Continued.

Part Number	A_0 [mm^2]	$\dot{m}_j$ [g/s]	ΔP [bar]	$S_{\Delta P}$ [bar]	T_r	S_{T_r} x10^{-5}	ρ_j [kg/m^3]	S_{ρ_j} [kg/m^3]	C_D	S_{C_D}
109665-R00-LS001_0002 (4 g/s experiment)	0.121	3.79	5.014	0.184	1.077	5.822	934.86	2.46	1.03	0.019
109665-R00-LS001_0002 (5 g/s experiment)	0.121	4.85	7.930	0.216	1.075	9.017	935.38	2.46	1.04	0.014
109665-R00-LS001_0003 (3 g/s experiment)	0.139	3.03	3.128	0.192	1.043	4.626	942.17	2.38	0.90	0.028
109665-R00-LS001_0003 (4 g/s experiment)	0.139	3.92	4.977	0.192	1.081	4.594	934.10	2.47	0.92	0.018
109665-R00-LS001_0003 (5 g/s experiment)	0.139	5.02	7.866	0.218	1.077	3.509	934.97	2.46	0.94	0.013
111007-R00-LS001_0001 (3 g/s experiment)	0.216	2.99	1.423	0.197	1.045	6.174	941.56	2.39	0.85	0.059
111007-R00-LS001_0001 (4 g/s experiment)	0.216	3.87	2.272	0.159	1.047	5.043	941.19	2.39	0.87	0.030
111007-R00-LS001_0001 (5 g/s experiment)	0.216	5.26	3.878	0.157	1.073	3.212	935.62	2.45	0.91	0.018
111007-R00-LS001_0002 (3 g/s experiment)	0.213	3.10	1.418	0.171	1.046	21.593	941.47	2.39	0.89	0.054
111007-R00-LS001_0002 (4 g/s experiment)	0.213	4.05	2.269	0.156	1.047	6.142	941.22	2.39	0.92	0.032
111007-R00-LS001_0002 (5 g/s experiment)	0.213	5.40	3.783	0.163	1.076	5.453	935.15	2.46	0.95	0.021
111007-R00-LS001_0003 (3 g/s experiment)	0.212	3.08	1.401	0.142	1.039	3.768	942.89	2.38	0.89	0.045
111007-R00-LS001_0003 (4 g/s experiment)	0.212	4.05	2.258	0.174	1.039	5.630	943.02	2.38	0.92	0.036
111007-R00-LS001_0003 (5 g/s experiment)	0.212	5.02	3.493	0.183	1.041	2.456	942.58	2.38	0.92	0.024

Table 4.3. Continued.

Part Number	A_0 [mm^2]	$\dot{m}_j$ [g/s]	ΔP [bar]	$S_{\Delta P}$ [bar]	T_r	S_{T_r} x10^{-5}	ρ_j [kg/m^3]	S_{ρ_j} [kg/m^3]	C_D	S_{C_D}
111013-R00-LS001_0001 (3 g/s experiment)	0.288	2.89	0.736	0.031	1.044	10.921	941.85	2.39	0.85	0.018
111013-R00-LS001_0001 (4 g/s experiment)	0.288	3.93	1.324	0.169	1.048	4.922	940.96	2.40	0.86	0.055
111013-R00-LS001_0001 (5 g/s experiment)	0.288	5.20	2.108	0.127	1.070	4.878	936.44	2.44	0.91	0.027
111013-R00-LS001_0002 (3 g/s experiment)	0.311	2.89	0.757	0.032	1.043	6.921	942.14	2.38	0.78	0.017
111013-R00-LS001_0002 (4 g/s experiment)	0.311	4.10	1.396	0.122	1.072	7.001	935.95	2.45	0.82	0.036
111013-R00-LS001_0002 (5 g/s experiment)	0.311	5.14	2.075	0.116	1.071	7.974	936.12	2.45	0.84	0.024
111013-R00-LS001_0003 (3 g/s experiment)	0.304	2.88	0.720	0.035	1.041	10.218	942.47	2.38	0.81	0.020
111013-R00-LS001_0003 (4 g/s experiment)	0.304	4.11	1.403	0.142	1.079	4.775	934.38	2.47	0.84	0.042
111013-R00-LS001_0003 (5 g/s experiment)	0.304	5.20	2.089	0.134	1.069	5.136	936.49	2.44	0.87	0.028
111013-R00-LS001_0004 (3g/s experiment)	0.306	2.92	0.757	0.025	1.042	3.971	942.27	2.38	0.80	0.013
111013-R00-LS001_0004 (4 g/s experiment)	0.306	4.05	1.342	0.166	1.050	13.207	940.53	2.40	0.83	0.052
111013-R00-LS001_0004 (5 g/s experiment)	0.306	5.27	2.093	0.129	1.067	2.198	936.96	2.44	0.87	0.027

Considering the discharge coefficient results given in Table 4.3, it can be said that injectors were produced finely, and their pressure loss characteristics are at a reasonable level. For the part having number 109665-R00-LS001_0002, the discharge coefficient value is close to 1 for each case (3 g/s, 4 g/s, and 5 g/s

experiments). As a result, it can be concluded that it has the lowest pressure loss characteristic. On the other hand, its discharge coefficient is slightly higher than 1 for 4 g/s and 5 g/s experiments. However, this is not possible for real applications, and it might be possibly due to the errors during the experiment.

4.3. Attenuation Coefficient Measurement of JP-10

Accurate measurement of droplet diameter with PDPA requires correct polarization of laser beams. To correctly polarize the beams, Flowsizer, which is the operating program of TSI Inc.'s PDPA system, needs the attenuation coefficient of the droplets [67]. The attenuation coefficient is defined as how strong a material absorbs the light at a given wavelength. In this case, the droplets are made of JP-10, and in the literature, the attenuation coefficient of JP-10 was not seen. Therefore, it had to be measured in the working wavelength region. SAGE has a Lamba 950 Spectrophotometer of PerkinElmer that can do such measurements.

Using a quartz cuvette that has a thickness (l) of 10 mm, the transmittance measurement of JP-10 was made in the spectrophotometer. Firstly, the spectrophotometer measured the incident intensity of light using an empty cuvette. Then, the spectrophotometer measured the transmitted intensity of light using the cuvette filled with JP-10. Finally, transmittance results were taken from the device and transformed into the attenuation coefficient using Equation 4.17.

Using The Bouguer-Beer-Lambert Law [69], the relations below can be written.

$$T_l = \frac{I_l}{I_0} \times 100 \tag{4.14}$$

where T_l is the transmittance of the light in percentage, I_l is transmitted intensity of the light and I_0 is the incident intensity of the light.

$$Ab = log_{10}\left(\frac{100}{T_l}\right) \tag{4.15}$$

where Ab is absorbance.

The Bouguer-Beer-Lambert Law states that $Ab = \epsilon lc$, where ϵ and c are molar extinction coefficient and molarity, respectively [69]. Therefore, $\alpha = \epsilon c$ is the attenuation/extinction coefficient. As a result, $Ab = \alpha l$ (4.16). Using the Equations 4.15 and 4.16, the Equation 4.17 is found and given below.

$$\alpha = \frac{log_{10}\left(\frac{100}{T_l}\right)}{l} \tag{4.17}$$

Transmittance values measured by the spectrophotometer between 300 and 1100 nm wavelength are given in Table A1.16 of Appendix 1. Using the relation above, attenuation coefficients were calculated and provided in the same table. Figure 4.8 provides a graphical view of the results.

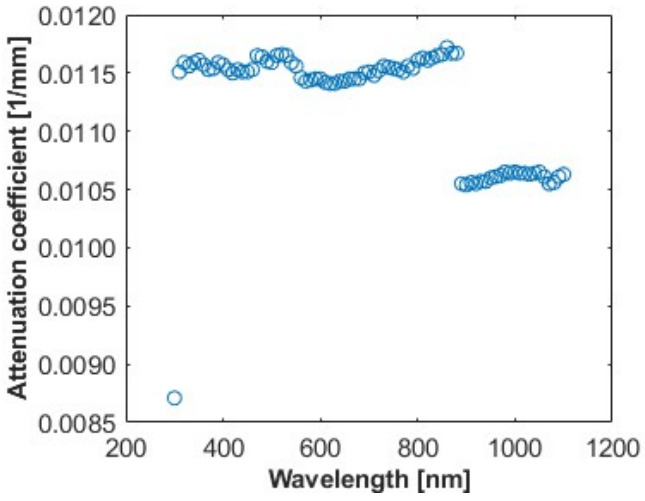

Figure 4.8. Attenuation Coefficient of JP-10 between 300 and 1100 nm wavelength.

As can be seen in Figure 4.8, the attenuation coefficient at 300 nm behaves as an outlier when compared with the other results at different wavelengths. Moreover, the mean of the attenuation coefficient is 0.0115 and 0.0106 mm-1 at wavelengths between 310 and 880 nm and between 890 and 1100 nm, respectively. Therefore, the following correlation is presented.

$$\alpha = \begin{cases} 0.00871\ at\ 300\ nm \\ 0.0115 \pm 7.89\times10^{-5}\ at\ 310-880\ nm \\ 0.0106 \pm 3.92\times10^{-5} at\ 890-1100\ nm \end{cases} \quad (4.18)$$

where α is the attenuation coefficient of JP-10 in mm^{-1}.

In conclusion, the attenuation coefficient of JP-10 for the wavelengths between 300 and 1100 nm was measured to be used for the measurements by PDPA since it was not available in the literature, and it is a required parameter for PDPA measurements. Its value was found to be between 0.00871 and 0.0115 mm^{-1}. As a comparison, water, Mil-C, and Jet-A fuels have attenuation coefficients of 0, 0.05, and 50 mm^{-1}, respectively [67]. Considering the findings here and the given values for related liquids, the attenuation coefficient of JP-10 is within a reasonable range.

4.4. Penetration Measurement of JP-10 Liquid Jet (Shadowgraphy Test)

In this section, the penetration measurement of the jet is presented, and the experiment results are compared with the data in the literature.

The tests were conducted in the shadowgraphy test setup assembly in Section 2.3.2. In the setup, there are five thermocouples: one is used to measure the crossflow temperature on the plenum chamber assembly, and two are used to measure the temperature inside the high-pressure chamber to check the temperature of crossflow coming from the test section. The other two

thermocouples are used to measure the surface temperature of the high-pressure chamber and the temperature of the jet placed in the injector. A pressure transducer is placed on the plenum chamber assembly to measure the pressure of the crossflow. Moreover, there are some other sensors in the test facility given in Section 2.1, which are three Coriolis flowmeters, of which two of them are used to measure flow rate in line-1 and 2, and one of them is used to flow rate through injector which is placed inside the conditioned fuel feeding system, and a pressure transducer and a thermocouple placed on the conditioned fuel feeding system to measure pressure and temperature of the fuel before entering the injector. The details of the placement of the sensors can be found in Sections 2.1 and 2.3.2 and in the section of the related sub-parts. In the experiments, all these sensors were used to measure data for the investigation of the penetration of the jet, and the data are presented in the upcoming parts.

In the experiments, the injector with part number 111007-R00-LS001_0001 was used. More information about the injector can be found in Sections 2.4.4 and 4.2. The injector's diameter was measured as 0.524 mm.

The shadowgraphy tests were tried to be completed for the case of M = 0.2, 2 bar, 493.15 K, and 74 g/s crossflow condition given in Table 2.3, and nitrogen was used as crossflow medium. The same crossflow condition was applied to 2, 3, and 4 g/s jet flow rate conditions, and the jet was not conditioned; in other words, it was not heated or chilled. Therefore, there were three separate conditions, and the tests were repeated twice for each condition to check the repeatability of the experiment. Time-averaged and standard deviation values of the data obtained from all sensors during the experiment can be found in Table 4.4 and Tables A1.17 and A1.18 of Appendix 1. The data in Table 4.4 are used to calculate correlations and non-dimensional numbers required for the shadowgraphy test. Additionally, there are extra data recorded during the experiments, which are presented in Tables A1.17 and A1.18 of Appendix 1, and these data were not used in any calculations and only checked during the experiments to get the proper results and for the safety of the experiments.

Table 4.4. Sensor data 1.

Case		P_g [bar]	T_g [K]	$\dot{m}_g$ [g/s]	T_j [K]	$\dot{m}_j$ [g/s]
2 g/s [1st]	Average	2.030	496.36	75.15	385.90	2.06
	Deviation	±1.331x10^{-3}	±1.4104x10^{-2}	±4.267x10^{-1}	±1.8697x10^{-1}	±6.47x10^{-2}
2 g/s [2nd]	Average	1.998	496.62	74.56	376.60	2.12
	Deviation	±2.066x10^{-3}	±1.7218x10^{-2}	±4.273x10^{-1}	±1.0432x10^{-1}	±6.64x10^{-2}
3 g/s [1st]	Average	2.060	496.71	75.30	377.37	3.05
	Deviation	±1.471x10^{-3}	±2.5002x10^{-2}	±5.227x10^{-1}	±3.0053x10^{-1}	±6.88x10^{-2}
3 g/s [2nd]	Average	2.036	496.94	72.94	376.13	3.00
	Deviation	±1.496x10^{-3}	±2.0448x10^{-2}	±5.656x10^{-1}	±5.8742x10^{-1}	±8.12x10^{-2}
4 g/s [1st]	Average	2.072	497.59	75.90	372.56	3.86
	Deviation	±1.679x10^{-3}	±9.9267x10^{-3}	±5.749x10^{-1}	±3.1732x10^{-1}	±6.39x10^{-2}
4 g/s [2nd]	Average	2.034	497.33	72.79	382.39	3.95
	Deviation	±1.629x10^{-3}	±1.0789x10^{-2}	±4.355x10^{-1}	±2.4441x10^{-1}	±1.16x10^{-1}

In the experiment, a Phantom V2640 high-speed camera was used to take photos of the jet. The camera data taken during the experiment can be found in Table 4.5. The data in the table apply to all the separate measurements.

Table 4.5. Camera data.

Camera	Sensor	Sensor	Acquired Resolution	FPS	Image Quantity	Test Duration [s]
Phantom V2640	RGB Cine	Mono	512x1024	14080	93022	6.607

The photos were not taken until the temperatures of crossflow, high-pressure chamber, and the surface of high-pressure chamber were stabilized. After stabilization, the experiments were carried out and photos of the jet in crossflow were taken.

Before presenting the penetration experiment's results, some formulations must be given to compare the findings with the literature. The experiment's findings are compared with the correlations' results in Table 1.3. The related parameters and their standard deviations were found using Equations 2.4, 2.5, 2.8-2.16, 4.8-4.11, and 4.19-4.38.

$$S_q = q\left[\left(\frac{S_{\rho_j}}{\rho_j}\right)^2 + \left(2\frac{S_{v_j}}{v_j}\right)^2 + \left(-\frac{S_{\rho_g}}{\rho_g}\right)^2 + \left(-2\frac{S_{u_g}}{u_g}\right)^2\right]^{1/2} \tag{4.19}$$

where S_q, S_{ρ_j}, S_{v_j}, S_{ρ_g} and S_{u_g} are the standard deviations in the momentum flux ratio, in the density of the jet, in the velocity of the jet, in the density of crossflow and the velocity of the crossflow, respectively, q is the momentum flux ratio, ρ_j is the density of the jet, v_j is the velocity of the jet, ρ_g is the density of the crossflow and u_g is the velocity of the crossflow.

$$S_{v_j} = v_j\left[\left(\frac{S_{\dot{m}_j}}{\dot{m}_j}\right)^2 + \left(-\frac{S_{\rho_j}}{\rho_j}\right)^2\right]^{1/2} \tag{4.20}$$

where $S_{\dot{m}_j}$ is the standard deviation in the mass flow rate of the jet and $\dot{m}_j$ is the mass flow rate of the jet.

$$S_{\rho_g} = \rho_g \left[\left(\frac{S_{P_g}}{P_g} \right)^2 + \left(-\frac{S_{T_g}}{T_g} \right)^2 \right]^{1/2} \tag{4.21}$$

where S_{P_g} and S_{T_g} are the standard deviations in the crossflow pressure and the crossflow temperature, respectively, P_g the crossflow pressure and T_g is the crossflow temperature.

$$u_g = \frac{\dot{m}_g}{\rho_g A_c} \tag{4.22}$$

where $\dot{m}_g$ is the mass flow rate of the crossflow and A_c is the cross-sectional area of the test section. The dimensions of the produced test section were 20.03 x 30.03 mm.

$$S_{u_g} = u_g \left[\left(\frac{S_{\dot{m}_g}}{\dot{m}_g} \right)^2 + \left(-\frac{S_{\rho_g}}{\rho_g} \right)^2 \right]^{1/2} \tag{4.23}$$

where $S_{\dot{m}_g}$ is the standard deviation in the mass flow rate of the crossflow.

$$S_{We_g} = We_g \left[\left(\frac{S_{\rho_g}}{\rho_g} \right)^2 + \left(2\frac{S_{u_g}}{u_g} \right)^2 + \left(-\frac{S_\sigma}{\sigma} \right)^2 \right]^{1/2} \tag{4.24}$$

where S_{We_g} and S_σ are the standard deviations in the crossflow Weber number and the surface tension of the jet, respectively, We_g is the crossflow Weber number and σ is the surface tension of the jet.

The surface tension of the jet (JP-10) can be found using the Eotvos rule, which is given in Equation 4.25 [70, 71].

$$\sigma = k_{eotvos}(T_c - T_j)\left(\frac{M_j}{\rho_j}\right)^{-2/3} \tag{4.25}$$

where k_{eotvos} is Eotvos-Ramsay coefficient (2.1 x 10^{-7} J/K.mole$^{2/3}$) [70], T_c is the critical temperature of the jet [JP-10] (698 K [58]), T_j is the temperature of the jet and M_j is the molecular weight of the jet [JP-10].

$$S_\sigma = \sigma\left[\left(\frac{S_{T_j}}{T_c - T_j}\right)^2 + \left(\frac{2}{3}\frac{S_{\rho_j}}{\rho_j}\right)^2\right]^{1/2} \tag{4.26}$$

where S_{T_j} is the standard deviation in the temperature of the jet.

$$S_{We_{aero}} = We_{aero}\left[\left(\frac{S_{\rho_g}}{\rho_g}\right)^2 + \left(2\frac{S_{v_j}}{v_j}\right)^2 + \left(-\frac{S_\sigma}{\sigma}\right)^2\right]^{1/2} \tag{4.27}$$

where $S_{We_{aero}}$ is the standard deviation in the aerodynamic Weber number and We_{aero} is the aerodynamic Weber number.

$$S_{Re_g} = Re_g\left[\left(\frac{S_{\rho_g}}{\rho_g}\right)^2 + \left(\frac{S_{u_g}}{u_g}\right)^2 + \left(-\frac{S_{\mu_g}}{\mu_g}\right)^2\right]^{1/2} \tag{4.28}$$

where S_{Re_g} and S_{μ_g} are the standard deviations in the crossflow Reynolds number and the dynamic viscosity of the crossflow, respectively, Re_g is the crossflow Reynolds number, and μ_g is the dynamic viscosity of the crossflow.

$$S_{\mu_g} = \mu_g \left[\left(\frac{3}{2} \frac{S_{T_g}}{T_g} \right)^2 + \left(- \frac{S_{T_g}}{T_g + 110.4} \right)^2 \right]^{1/2} \tag{4.29}$$

$$S_{Re_{ch}} = Re_{ch} \left[\left(\frac{S_{\rho_g}}{\rho_g} \right)^2 + \left(\frac{S_{u_g}}{u_g} \right)^2 + \left(- \frac{S_{\mu_g}}{\mu_g} \right)^2 \right]^{1/2} \tag{4.30}$$

where $S_{Re_{ch}}$ is the standard deviation in the channel Reynolds number, and Re_{ch} is the channel Reynolds number.

$$S_{Re_j} = Re_j \left[\left(\frac{S_{\rho_j}}{\rho_j} \right)^2 + \left(\frac{S_{v_j}}{v_j} \right)^2 + \left(- \frac{S_{\mu_j}}{\mu_j} \right)^2 \right]^{1/2} \tag{4.31}$$

where S_{Re_j} and S_{μ_j} are the standard deviations in the jet Reynolds number and the dynamic viscosity of the jet, respectively, Re_j is the jet Reynolds number, and μ_j is the dynamic viscosity of the jet.

$$\mu_j = exp \left(\frac{\beta_1}{T_r + \beta_2} + \beta_3 T_r + \beta_4 T_r^2 \right) \times 10^{-3} \tag{4.32}$$

where β_1, β_2, β_3 and β_4 are parameters for viscosity calculation [58], T_r is the reduced absolute temperature, which is given in Equation 4.8. The values and standard deviation of the parameters are presented in Table 4.6.

Table 4.6. Parameter values and associated standard deviations for Equation 4.32 [58].

Parameter	Parameter Value	Standard Deviation
β_1	1.82400	0.0099
β_2	-0.430094	0.0013
β_3	-1.99450	0.025
β_4	0.370442	0.014

$$S_{\mu_j} = \mu_j \left[\left(\frac{S_{\beta_1}}{T_r + \beta_2} \right)^2 + \left(S_{T_r} \times \left[-\frac{\beta_1}{(T_r + \beta_2)^2} + \beta_3 + 2\beta_4 T_r \right] \right)^2 + \left(-\frac{S_{\beta_2} \times \beta_1}{(T_r + \beta_2)^2} \right)^2 + \left(S_{\beta_3} \times T_r \right)^2 + \left(S_{\beta_4} \times T_r^2 \right)^2 \right]^{1/2} \quad (4.33)$$

where S_{β_1}, S_{β_2}, S_{β_3} and S_{β_4} are the standard deviations in the parameters for viscosity calculation and S_{T_r} is the standard deviation in the reduced absolute temperature.

Equations 4.34-4.38 represent the formulas for finding the standard deviation in penetration height for the penetration correlations given in Table 1.3. Equations 4.34, 4.35, 4.36, 4.37, and 4.38 are used for the correlations of “Masuda and McDonell,” “Bellofiore et al.,” “Ragucci et al.,” “Li et al.,” and “Eslamian et al.” given in Table 1.3, respectively. The calculation results are presented in Tables 4.10 and 4.11.

$$S_z = z \left[\left(0.5 \frac{S_q}{q} \right)^2 + \left(-0.41 \frac{S_{We_g}}{We_g} \right)^2 + \left(-0.027 \frac{S_{\mu_j}}{\mu_j} \right)^2 \right]^{1/2} \quad (4.34)$$

where S_z is the standard deviation in the penetration height and z is the penetration height.

$$S_z = z\left[\left(0.476\frac{S_q}{q}\right)^2 + \left(-0.128\frac{S_{We_{aero}}}{We_{aero}}\right)^2 + \left(0.135\frac{S_{Re_g}}{Re_g}\right)^2\right]^{1/2} \quad (4.35)$$

$$S_z = z\left[\left(0.422\frac{S_q}{q}\right)^2 + \left(-0.015\frac{S_{We_{aero}}}{We_{aero}}\right)^2 + \left(0.186\frac{S_{\mu_g}}{\mu_g}\right)^2\right]^{1/2} \quad (4.36)$$

$$S_z = z\left[\left(0.4356\frac{S_q}{q}\right)^2 + \left(0.01147\frac{S_{We_g}}{We_g}\right)^2 + \left(0.295\frac{S_{T_g}}{T_g}\right)^2\right]^{1/2} \quad (4.37)$$

$$S_z = z\left[\left(0.3\frac{S_q}{q}\right)^2 + \left(0.12\frac{S_{Re_{ch}}}{Re_{ch}}\right)^2 + \left(0.14\frac{S_{Re_j}}{Re_j}\right)^2\right]^{1/2} \quad (4.38)$$

Time-averaged and standard deviation values of non-dimensional numbers and velocities of the experiments can be found in Tables 4.7 and 4.8.

Table 4.7. Non-dimensional numbers of the penetration experiment 1.

Case	u_g [m/s]		q		We_g		We_{aero}	
	Avg.	Dev.	Avg.	Dev.	Avg.	Dev.	Avg.	Dev.
2 g/s [1st]	90.67	±0.52	9.30	±0.60	264.63	±3.11	3.93	±0.25
2 g/s [2nd]	91.47	±0.53	9.84	±0.63	255.71	±3.06	3.92	±0.25
3 g/s [1st]	89.61	±0.63	20.58	±0.99	253.75	±3.61	8.39	±0.38
3 g/s [2nd]	87.82	±0.68	20.89	±1.19	239.75	±3.81	7.95	±0.43
4 g/s [1st]	89.96	±0.69	32.30	±1.21	252.24	±3.90	13.09	±0.45
4 g/s [2nd]	87.82	±0.53	36.42	±2.22	244.96	±3.03	14.21	±0.85

Table 4.8. Non-dimensional numbers of the penetration experiment 2.

Case	Re_g		Re_{ch}		Re_j	
	Avg.	Dev.	Avg.	Dev.	Avg.	Dev.
2 g/s [1st]	2.46E+03	±14.2	1.30E+05	±749	6.24E+03	±351
2 g/s [2nd]	2.44E+03	±14.5	1.29E+05	±763	5.84E+03	±321
3 g/s [1st]	2.47E+03	±17.3	1.30E+05	±914	8.46E+03	±429
3 g/s [2nd]	2.39E+03	±18.7	1.26E+05	±987	8.20E+03	±435
4 g/s [1st]	2.48E+03	±19.0	1.31E+05	±1005	1.01E+04	±483
4 g/s [2nd]	2.38E+03	±14.5	1.26E+05	±766	1.15E+04	±632

As Table 4.5 shows, 93022 photos were taken for each case. These photos were averaged and processed using an image processor tool. The averaged and processed photos are shown in Figures 4.9-4.11.

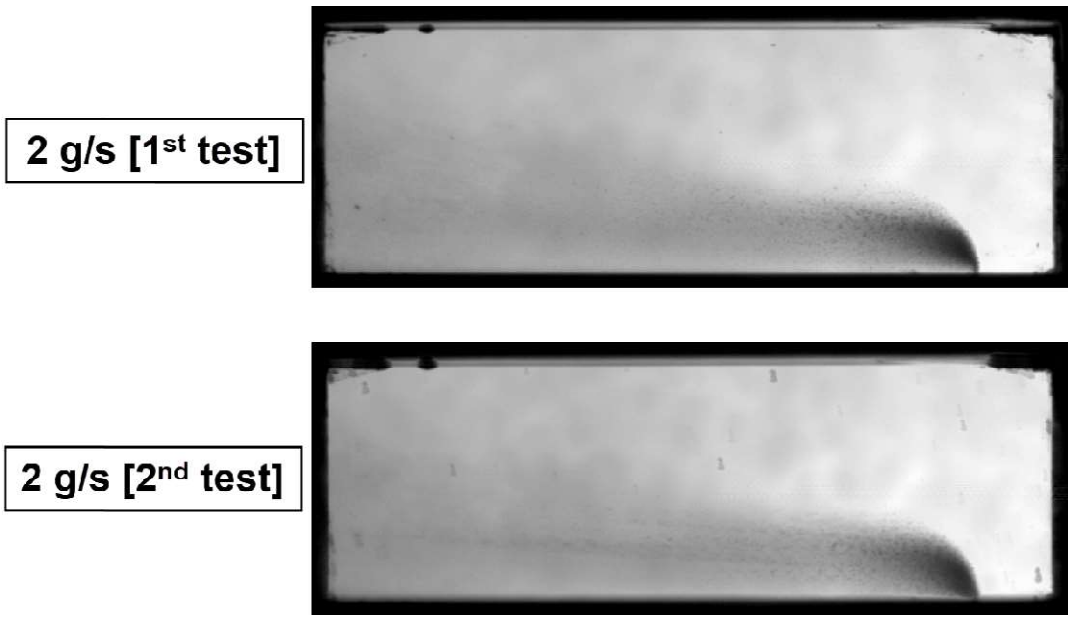

Figure 4.9. Penetration of the jet for 2 g/s jet flow rate case.

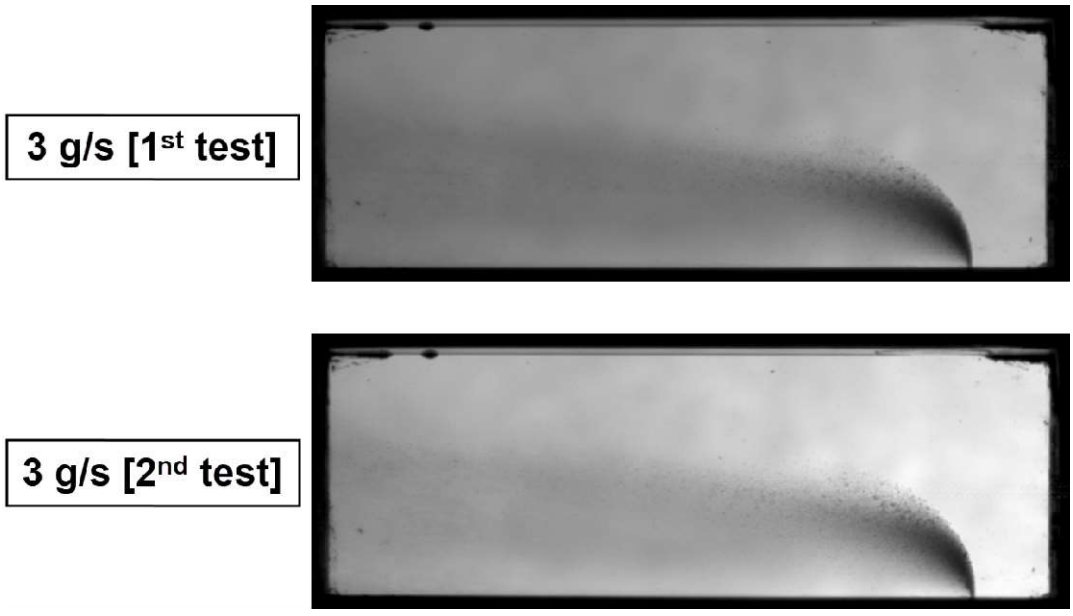

Figure 4.10. Penetration of the jet for 3 g/s jet flow rate case.

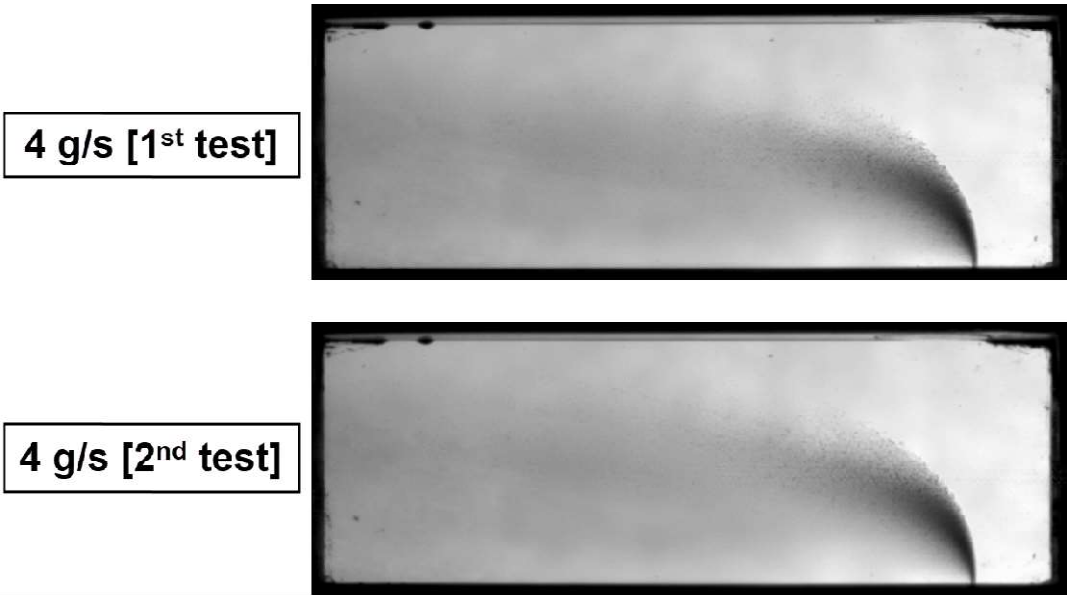

Figure 4.11. Penetration of the jet for 4 g/s jet flow rate case.

Using the averaged photos, penetration length and height were measured by analyzing the grey value of pixels on the images, and they are given in Table 4.9. The normalized penetration length and height values are also given in Table 4.9 since they are compared with normalized values in the literature. Analysis of the grey value of pixels on photos is explained below for the 2 g/s [1st] case, and the same methodology is used for other cases, too.

Firstly, a line was inserted in the photo in the crossflow direction, starting from the injector's exit, to find the jet's penetration length. The inserted line in the photo of the 2 g/s [1st] case is shown as a yellow line in Figure 4.12. The grey value of pixels on this yellow line was found using an image processing tool and is given in Figure 4.13. The grey values were analyzed, and it was concluded that the penetration length of the jet was not so clear due to the brightness of the photo, and its value is set as an interval between 20-65 mm.

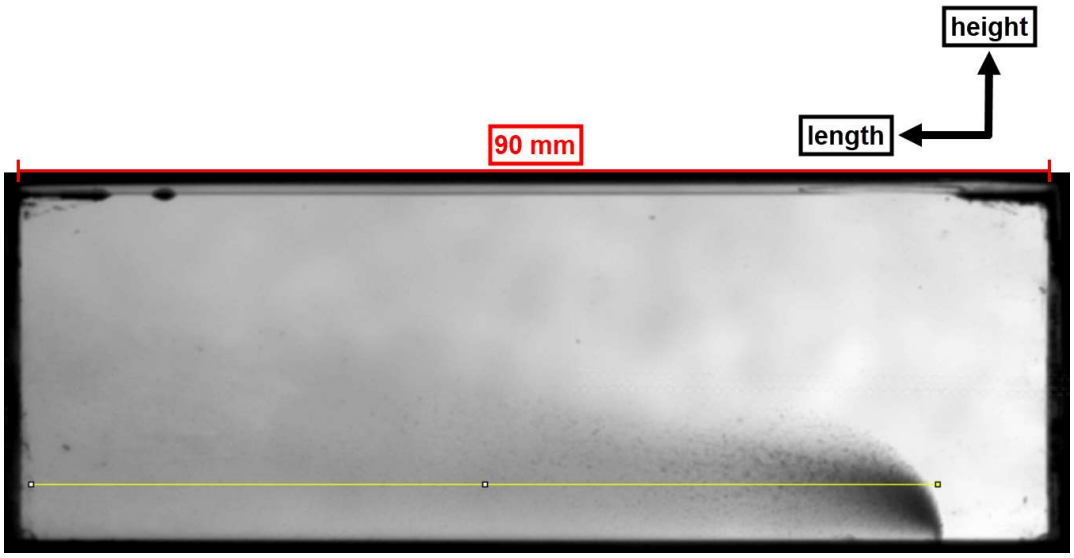

Figure 4.12. The line inserted in the photo of the 2 g/s [1st] case in the direction of the crossflow starting from the exit of the injector to find the penetration length of the jet.

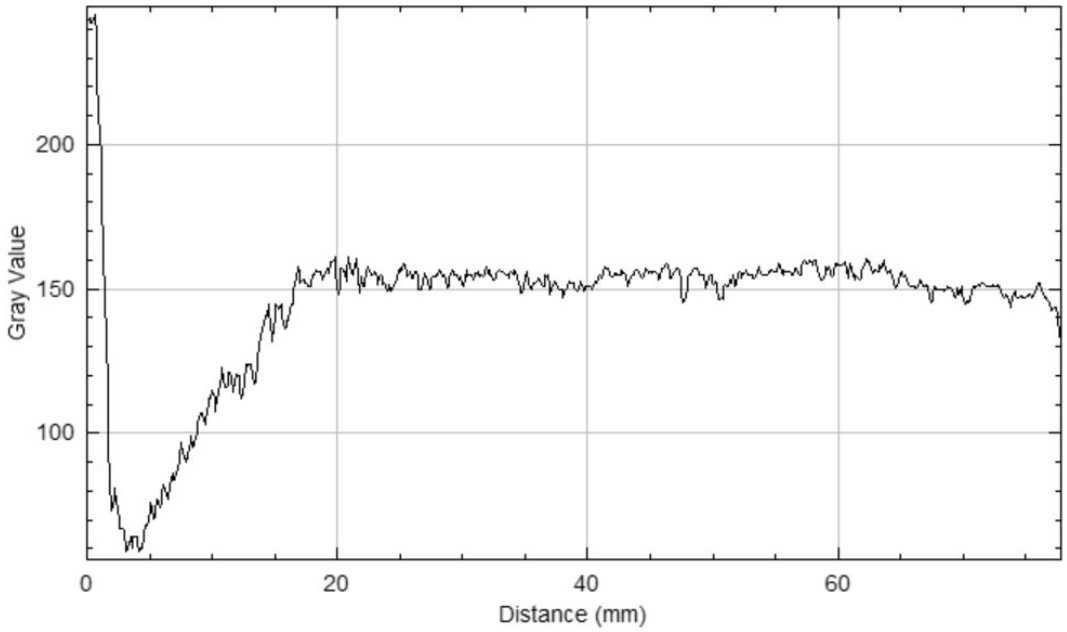

Figure 4.13. The grey value of pixels on the line given in Figure 4.12 to find the penetration length of the jet.

After finding the penetration length value, a line was inserted on the photo in the middle point of the penetration length interval, which is 42.5 mm from the exit of

the injector in the jet direction starting from the wall, to find the penetration length of the jet. The inserted line in the photo of the 2 g/s [1st] case is shown as a yellow line in Figure 4.14. The grey value of pixels on this yellow line was found using an image processing tool and is given in Figure 4.15. Grey values of the photo were analyzed, and the droplets' starting and ending points are provided by red arrow arrows in Figure 4.15. Therefore, the penetration height of the jet is found, which is the distance from the wall to the ending point of the droplets, as 12.9 mm.

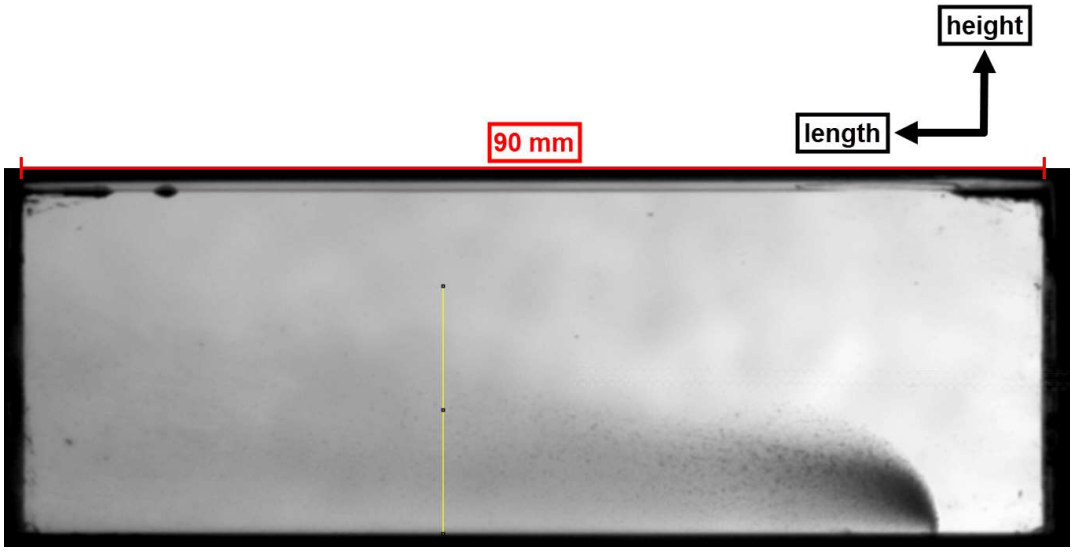

Figure 4.14. The line inserted in the photo of the 2 g/s [1st] case in the middle point of the penetration length interval, which is 42.5 mm from the exit of the injector in the direction of the jet starting from the wall to find the penetration length of the jet.

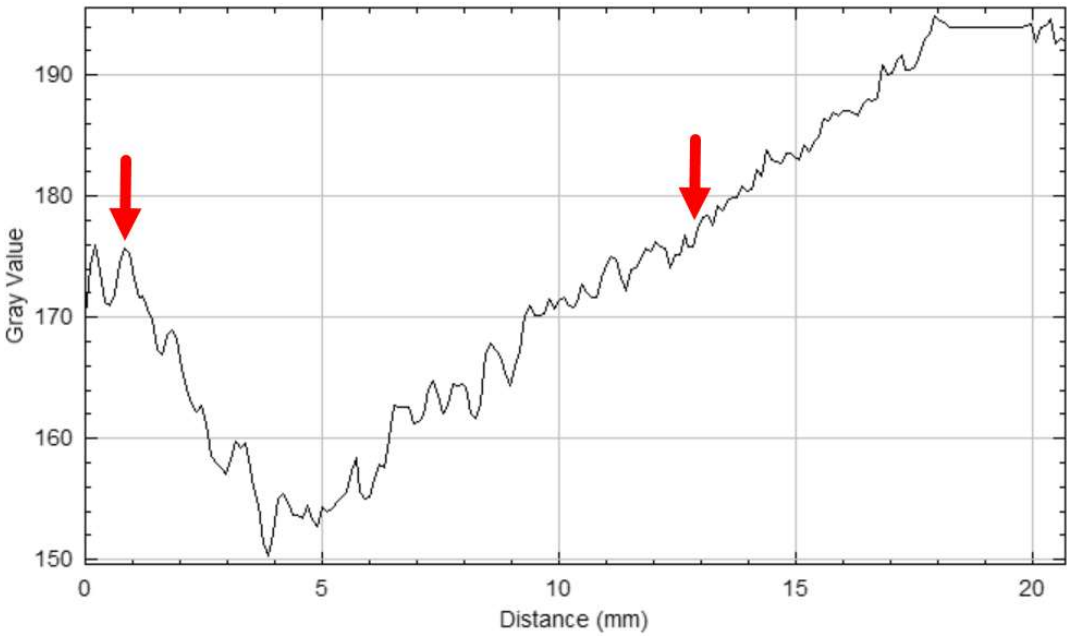

Figure 4.15. The grey value of pixels on the line given in Figure 4.14 to find the penetration height of the jet.

Table 4.9. Penetration length and height results.

Case	x [mm]	x/d_j	z [mm]	z/d_j
2 g/s [1st]	20-65	38-124	12.9	24.6
2 g/s [2nd]	20-65	38-124	13.1	25.0
3 g/s [1st]	20-65	38-124	19.0	36.3
3 g/s [2nd]	20-65	38-124	19.5	37.2
4 g/s [1st]	20-65	38-124	25.5	48.7
4 g/s [2nd]	20-65	38-124	25.9	49.4

Before discussing the results and comparing them with values given in the literature, it was expected the results found in the current study to be different from the values given in the literature since the experimental conditions of the

current research, such as Weber number, crossflow temperature and pressure, and the liquid jet type (JP-10), are different from the literature. The comparison of the conditions of the current study and works in the literature can be seen in Tables 4.4, 4.7, 4.8, and 4.12.

By analyzing the results given in Table 4.9, it can be said that penetration length is identical for all cases. In the literature, the normalized value of the penetration length is given constant for each case. In the current study, similar behavior was observed where the normalized value of the penetration length of the jet was found between 38-124. However, the normalized value of the penetration length differs from the values in the literature, as seen in Tables 4.10 and 4.11. This was an expected result since the current study's conditions differ from the literature. The normalized values of the penetration length are between 12 and 40 in the literature.

Moreover, as seen in Table 4.9, penetration height gets larger when the jet flow rate is increased, and this result is reasonable since the momentum flux ratio increases when the flow rate is increased. A higher momentum flux ratio makes the jet penetrate further into the crossflow; the same trend was also observed in the literature. Normalized values of the penetration height were found between 24.6 and 49.4 in the current study. On the other hand, they were calculated between 15 and 33 using the correlation given in the literature (see Tables 4.10 and 4.11). As for the penetration length situation, the penetration height results were also found to be different from the literature, which was also the expected result.

Table 4.10. Penetration calculations in the literature for the comparison with the current study 1.

Case	Masuda			Bellofiore			Ragucci		
	x/d_j	z/d_j		x/d_j	z/d_j		x/d_j	z/d_j	
		Avg.	Dev.		Avg.	Dev.		Avg.	Dev.
2 g/s [1st]	12	10.6	±0.3	12	15.1	±0.5	12	15.2	±0.4
2 g/s [2nd]	12	11.0	±0.4	12	15.5	±0.5	12	15.6	±0.4
3 g/s [1st]	12	16.0	±0.4	12	20.0	±0.5	12	21.1	±0.4
3 g/s [2nd]	12	16.5	±0.5	12	20.2	±0.6	12	21.2	±0.5
4 g/s [1st]	12	20.1	±0.4	12	23.4	±0.4	12	25.3	±0.4
4 g/s [2nd]	12	21.7	±0.7	12	24.4	±0.7	12	26.6	±0.7

Table 4.11. Penetration calculations in the literature for the comparison with the current study 2.

Case	Li			Eslamian		
	x/d_j	z/d_j		x/d_j	z/d_j	
		Avg.	Dev.		Avg.	Dev.
2 g/s [1st]	40	18.1	±0.5	17	17.6	±0.4
2 g/s [2nd]	40	18.6	±0.5	17	17.7	±0.4
3 g/s [1st]	40	25.6	±0.5	17	23.3	±0.4
3 g/s [2nd]	40	25.7	±0.6	17	23.2	±0.4
4 g/s [1st]	40	31.1	±0.5	17	27.4	±0.4
4 g/s [2nd]	40	32.8	±0.9	17	28.8	±0.6

In conclusion, the difference in penetration length and height measurement in the current study from the literature might be the Weber number difference. In the current work, crossflow and aerodynamic Weber numbers are between 239.75 and 264.63, and between 3.92 and 14.21, respectively (see Tables 4.7 and 4.8 for the details). On the other hand, the correlations in the literature were developed for the crossflow and aerodynamic Weber numbers between 20 and 1630, and between 7 and 410.5, respectively (see Table 4.12 for the details). Therefore, it can be said that Weber number values for the cases considered in the literature are higher than those of the current study. Weber number is the ratio of the crossflow's inertial forces to the jet's surface tension forces. Since the lower Weber number values are analyzed in the current study, it might have caused the jet to penetrate further into the crossflow.

Table 4.12. Non-dimensional numbers and conditions for the jet penetration in the literature [4].

Reference	q	We_g	P_g [bar]	T_g [K]
Masuda and McDonell [45]	2.2-75	700-1580	3.8-6.5	350-475
Bellofiore et al. [44]	12.2-71.4	We_{aero} = 10.4-410.5	10, 20	300, 600
Ragucci et al. [46]	5-280	We_{aero} = 7-340	20	600
Li et al. [47]	16-76	399-1630	5-20	280-650
Eslamian et al. [19]	10-80	20-487	2.1-5.2	298-573

To understand the penetration of the jet at HTP conditions, further experiments are required, and a correlation needs to be developed for JP-10 with these experiments and conditions.

5. CONCLUSION

The injectors and atomizers are essential elements in today's world. They are used in a wide range of applications, from home appliances (shower heads) to fuel injectors of any type of engine. Their applications can be as pressure swirl atomizers of gas turbines and industrial furnaces, plain orifice atomizers of internal combustion engines, ramjet/scramjet engines, fan spray atomizers of disinfection devices for agriculture, rotary atomizers of paint lines, etc. Their physical characteristics have not been fully understood, and therefore, they still require deep research to develop system efficiencies.

In the context of this thesis, the liquid jet in subsonic crossflow was investigated experimentally using plain orifice atomizers at HTP conditions. Two different test setups were designed for penetration measurements via a high-speed camera, velocity and diameter distributions measurement of droplets created in crossflow and jet's far-field region by PDPA. The designed setups were produced, endurance and leakage tests were performed for the produced parts, and it was seen that they were ready for the usage of the tests. The produced test setups were integrated into the test facility at TÜBİTAK SAGE, and preliminary tests with shadowgraphy test setup assembly were conducted. It was seen that the shadowgraphy test setup assembly works properly and is ready to use for future work.

In the design phase of the test setups, 1-D isentropic calculations and numerical analysis with CFD tools were used to design the setup correctly, and the results of 1-D isentropic calculations and CFD analysis were found to be similar.

Ten different injectors were produced, and their discharge coefficient was measured and found to be between 0.78 and 0.98.

An essential parameter for PDPA measurements, the attenuation coefficient for JP-10 was measured and found to be between 0.00871 and 0.0115 mm^{-1} at

between 300 and 1100 nm wavelength, which was not given in the literature before.

In the shadowgraphy test setup assembly, the penetration measurements of the jet were conducted for three different cases using JP-10 as the jet's medium, which was not presented in the literature before. There was a discrepancy between the jet penetration results obtained in the experiments and those calculated using the correlations. This was attributed to the different conditions of the correlations compared to experimental conditions. Apparently, there is not a single correlation in the literature that fully covers the conditions of this current experimental study, and it was concluded that a new correlation is required for the JP-10 jet and cases given in this study.

In the open literature, there is not much work by PDPA on the topic of liquid jets in subsonic crossflow. Moreover, there are a few works on the topic by PDPA and high-speed imaging at HTP. The designed test setups can be used in this region to cover related problems. The findings of this thesis can also be used to develop the associated systems further and understand the underlying physics. Once the PDPA measurements are completed, the results can be utilized as validation data sets for numerical models. Also, the produced and integrated test setups to the test facility at TÜBİTAK SAGE are valuable contributions to TÜBİTAK SAGE’s infrastructure, enabling more comprehensive studies about developing related propulsion systems in the near future.

5.1. Recommendations for Future Work

The liquid jet in crossflow needs to be further investigated experimentally and numerically. There is not much numerical work on the topic since the related models are currently being developed due to the requirement for high computational power. Since computational power has been significantly improved lately, in the upcoming years, there will be a lot of work on the topic by

numerical analysis, and they are deeply required. Therefore, recommendations for future work can be listed as follows:

- For the given crossflow conditions in Table 2.3, experimentation of all points needs to be completed,
- Other types of fuels or liquids could be used for the same conditions, and the finding of each liquid can be compared,
- The conditions given in the literature could be repeated at the integrated test setups, and results could be compared,
- Since the crossflow flow rate in the current study is 85 g/s at max, high-speed subsonic conditions (>0.4 Mach) and high-pressure (>4 bar) could not be included in the study. Therefore, the investigation for high-speed and high-pressure conditions is required using JP-10 as a test liquid,
- Other injectors, e.g., pressure swirl atomizers, can be designed and connected to the designed setup to investigate liquid sheets in subsonic crossflow applications. The results can be compared with the current study,
- Tests using PDPA on the setup need to be run to check the PDPA test setup assembly works properly. Afterward, tests with PDPA for all conditions need to be completed to contribute to the literature and develop related system efficiencies,
- Numerical analysis for the liquid jet in subsonic crossflow for the conditions given in this study needs to be done to understand further the underlying physics, and the result of the analysis needs to be compared with the results of tests done by PDPA,
- The designed setups can be further revised to investigate liquid jets in supersonic crossflow applications.

6. REFERENCES

[1] R. S. Fry, "A Century of Ramjet Propulsion Technology Evolution," *Journal of Propulsion and Power,* vol. 20, no. 1, pp. 27-58, 2004, doi: 10.2514/1.9178.

[2] I. Singh, "Design, Manufacture and Testing of Subsonic Ramjet Engine," Master of Technology, Department of Mechanical Engineering, Indian Institute of Technology Bombay, 2014.

[3] A. H. Lefebvre and V. G. McDonell, *Atomization and Sprays*, 2nd Edition ed. Boca Raton: CRC Press, 2017.

[4] M. Broumand and M. Birouk, "Liquid jet in a subsonic gaseous crossflow: Recent progress and remaining challenges," *Progress in Energy and Combustion Science,* vol. 57, pp. 1-29, 2016.

[5] P.-K. Wu, K. A. Kirkendall, R. P. Fuller, and A. S. Nejad, "Breakup processes of liquid jets in subsonic crossflows," *Journal of Propulsion and power,* vol. 13, no. 1, pp. 64-73, 1997.

[6] J. Mazallon, Z. Dai, and G. Faeth, "Primary breakup of nonturbulent round liquid jets in gas crossflows," *Atomization and Sprays,* vol. 9, no. 3, 1999.

[7] K. A. Sallam, C. Aalburg, and G. M. Faeth, "Breakup of Round Nonturbulent Liquid Jets in Gaseous Crossflow," *AIAA Journal,* vol. 42, no. 12, pp. 2529-2540, 2004, doi: 10.2514/1.3749.

[8] J. Becker and C. Hassa, "Breakup and atomization of a kerosene jet in crossflowat elevated pressure," *Atomization and Sprays,* vol. 12, no. 1-3, 2002.

[9] S. Tambe, S.-M. Jeng, H. Mongia, and G. Hsiao, "Liquid jets in subsonic crossflow," in *43rd AIAA aerospace sciences meeting and exhibit*, 2005, p. 731.

[10] G. Vich and M. Ledoux, "Investigation of a liquid jet in a subsonic cross-flow," *International Journal of Fluid Mechanics Research,* vol. 24, no. 1-3, 1997.

[11] M. Birouk, B. J. Azzopardi, and T. Stäbler, "Primary Break-up of a Viscous Liquid Jet in a Cross Airflow," *Particle & Particle Systems Characterization: Measurement and Description of Particle Properties and Behavior in Powders and Other Disperse Systems,* vol. 20, no. 4, pp. 283-289, 2003.

[12] C.-L. Ng, R. Sankarakrishnan, and K. Sallam, "Bag breakup of nonturbulent liquid jets in crossflow," *International Journal of Multiphase Flow,* vol. 34, no. 3, pp. 241-259, 2008.

[13] R. K. Madabhushi, M. Y. Leong, M. Arienti, C. T. Brown, and V. G. McDonell, "On the breakup regime map of liquid jet in crossflow," in *ILASS Americas, 19th Annual Conference on Liquid Atomization and Spray Systems, Toronto, Canada*, 2006.

[14] C. T. Brown and V. G. McDonell, "Near field behavior of a liquid jet in a crossflow," in *Proceedings of the ILASS Americas, 19th Annual Conference on Liquid Atomization and Spray Systems*, 2006.

[15] L. R and J. SM, "Liquid jet breakup in subsonic air stream at elevated temperatures," in *ILASS-Americas*, Irvine (CA), 2005.

[16] O. M. Elshamy and S.-M. Jeng, "A Study of Liquid Jet in Crossflow at Elevated Ambient Pressures," in *Proceedings of the 18th International*

Conference on Liquid Atomization and Spray System, Madison, Irvine, CA, 2005.

[17] J. Song, C. Cary Cain, and J. Guen Lee, "Liquid Jets in Subsonic Air Crossflow at Elevated Pressure," *Journal of Engineering for Gas Turbines and Power,* vol. 137, no. 4, 2014, doi: 10.1115/1.4028565.

[18] M. Birouk, T. Stäbler, and B. J. Azzopardi, "An Experimental Study of Liquid Jets Interacting with Cross Airflows," *Particle & Particle Systems Characterization,* vol. 20, no. 1, pp. 39-46, 2003, doi: https://doi.org/10.1002/ppsc.200390003.

[19] M. Eslamian, A. Amighi, and N. Ashgriz, "Atomization of Liquid Jet in High-Pressure and High-Temperature Subsonic Crossflow," *AIAA Journal,* vol. 52, no. 7, pp. 1374-1385, 2014, doi: 10.2514/1.J052548.

[20] R. P. Fuller, P.-K. Wu, K. A. Kirkendall, and A. S. Nejad, "Effects of Injection Angle on Atomization of Liquid Jets in Transverse Airflow," *AIAA Journal,* vol. 38, no. 1, pp. 64-72, 2000, doi: 10.2514/2.923.

[21] K. Sallam, C. Ng, R. Sankarakrishnan, C. Aalburg, and K. Lee, "Breakup of Turbulent and Non-Turbulent Liquid jets in Gaseous Crossflows," in *44th AIAA Aerospace Sciences Meeting and Exhibit*.

[22] A. Osta and K. Sallam, "Effect of Nozzle Length/Diameter Ratio on the Breakup of Round Liquid Jets in Crossflow," in *46th AIAA Aerospace Sciences Meeting and Exhibit*.

[23] A. R. Osta and K. A. Sallam, "Nozzle-Geometry Effects on Upwind-Surface Properties of Turbulent Liquid Jets in Gaseous Crossflow," *Journal of Propulsion and Power,* vol. 26, no. 5, pp. 936-946, 2010, doi: 10.2514/1.49737.

[24] C. Aalburg, G. Faeth, and K. Sallam, "Primary Breakup of Round Turbulent Liquid Jets in Uniform Gaseous Crossflows," in *43rd AIAA Aerospace Sciences Meeting and Exhibit*.

[25] R. Sankarakrishnan, K. A. Sallam, and F. W. Chambers, "Effects of Turbulence on the Breakup of Round Liquid Jets in Gaseous Crossflow," in *ASME 2005 Fluids Engineering Division Summer Meeting*, 2005, vol. Volume 2: Fora, pp. 281-285, doi: 10.1115/fedsm2005-77407. [Online]. Available: https://doi.org/10.1115/FEDSM2005-77407

[26] K. Lee, C. Aalburg, F. J. Diez, G. M. Faeth, and K. A. Sallam, "Primary Breakup of Turbulent Round Liquid Jets in Uniform Crossflows," *AIAA Journal,* vol. 45, no. 8, pp. 1907-1916, 2007, doi: 10.2514/1.19397.

[27] Y. Zheng and A. W. Marshall, "Characterization of the initial spray from low-Weber-number jets in crossflow," *Atomization and Sprays,* vol. 21, no. 7, 2011.

[28] C. D. Bolszo, V. G. McDonell, G. A. Gomez, and G. S. Samuelsen, "Injection of water-in-oil emulsion jets into a subsonic crossflow: An experimental study," *Atomization and Sprays,* vol. 24, no. 4, 2014.

[29] E. Farvardin, M. Johnson, H. Alaee, A. Martinez, and A. Dolatabadi, "Comparative Study of Biodiesel and Diesel Jets in Gaseous Crossflow," *Journal of Propulsion and Power,* vol. 29, no. 6, pp. 1292-1302, 2013, doi: 10.2514/1.B34743.

[30] P.-K. Wu, K. A. Kirkendall, R. P. Fuller, M. R. Gruber, and A. S. Nejad, "Spray Trajectories of Liquid Fuel Jets in Subsonic Crossflows," vol. 24, no. 1-3, pp. 128-137, 1997-06-01 1997, doi: 10.1615/InterJFluidMechRes.v24.i1-3.130.

[31] L. CK, K. JP, and J. TA, "A review on penetration heights of transverse liquid jets in high-speed flows," in *15th annual conference on liquid atomization and spray systems*, 2003, pp. 345–349.
[32] J. Stenzler, J. Lee, and D. Santavicca, "Penetration of Liquid Jets in a Crossflow," in *41st Aerospace Sciences Meeting and Exhibit*.
[33] J. Kim, Y. Yoon, and K. Ahn, "EFFECTS OF ORIFICE INTERNAL FLOW ON TRANSVERSE INJECTION INTO SUBSONIC CROSSFLOWS: CAVITATION AND HYDRAULIC FLIP," vol. 16, no. 1, pp. 15-34, 2006-01-01 2006, doi: 10.1615/AtomizSpr.v16.i1.20.
[34] C. O. Iyogun, M. Birouk, and N. Popplewell, "TRAJECTORY OF WATER JET EXPOSED TO LOW SUBSONIC CROSS-FLOW," vol. 16, no. 8, pp. 963-980, 2006-08-01 2006, doi: 10.1615/AtomizSpr.v16.i8.70.
[35] J. N. Stenzler, J. G. Lee, D. A. Santavicca, and W. Lee, "PENETRATION OF LIQUID JETS IN A CROSS-FLOW," vol. 16, no. 8, pp. 887-906, 2006-08-01 2006, doi: 10.1615/AtomizSpr.v16.i8.30.
[36] M. Birouk, C. O. Iyogun, and N. Popplewell, "ROLE OF VISCOSITY ON TRAJECTORY OF LIQUID JETS IN A CROSS-AIRFLOW," vol. 17, no. 3, pp. 267-287, 2007-01-20 2007, doi: 10.1615/AtomizSpr.v17.i3.30.
[37] C. T. Brown, U. Mondragon, and V. G. McDonell, "Investigation of the effect of injector discharge coefficient on penetration of a plain liquid jet into a subsonic crossflow," in *ILASS-Americas 20th annual conference on liquid atomization and spray systems*, 2007, pp. 15–18.
[38] S. M. Thawley, U. Mondragon, C. T. Brown, and V. G. McDonell, "Evaluation of column breakpoint and trajectory for a plain liquid jet injected into a crossflow," in *ILASS-Americas 21st annual conference on liquid atomization and spray systems*, 2008, pp. 1-11.
[39] Q. Wang, U. M. Mondragon, C. T. Brown, and V. G. McDonell, "CHARACTERIZATION OF TRAJECTORY, BREAK POINT, AND BREAK POINT DYNAMICS OF A PLAIN LIQUID JET IN A CROSSFLOW," vol. 21, no. 3, pp. 203-219, 2011-11-17 2011, doi: 10.1615/AtomizSpr.2011002848.
[40] H. J. Yoon, J. G. Hong, and C.-W. Lee, "CORRELATIONS FOR PENETRATION HEIGHT OF SINGLE AND DOUBLE LIQUID JETS IN CROSS FLOW UNDER HIGH-TEMPERATURE CONDITIONS," vol. 21, no. 8, pp. 673-686, 2012-02-24 2011, doi: 10.1615/AtomizSpr.2012004212.
[41] R. Ragucci, A. Bellofiore, and A. Cavaliere, "TRAJECTORY AND MOMENTUM COHERENCE BREAKDOWN OF A LIQUID JET IN HIGH-DENSITY AIR CROSS-FLOW," vol. 17, no. 1, pp. 47-70, 2006-10-01 2007, doi: 10.1615/AtomizSpr.v17.i1.20.
[42] S. Freitag and C. Hassa, "Spray characteristics of a kerosene jet in cross flow of air at elevated pressure," in *Proceedings ILASS-Europe*, 2008, pp. 8-10.
[43] E. Lubarsky, D. Shcherbik, O. Bibik, Y. Gopala, J. W. Bennewitz, and B. T. Zinn, "Fuel jet in cross flow-experimental study of spray characteristics," in *23rd annual conference on liquid atomization and spray systems*, Ventura, Canada, 2011.
[44] A. Bellofiore, A. Cavaliere, and R. Ragucci, "AIR DENSITY EFFECT ON THE ATOMIZATION OF LIQUID JETS IN CROSSFLOW," *Combustion*

Science and Technology, vol. 179, no. 1-2, pp. 319-342, 2007/01/01 2007, doi: 10.1080/00102200600809563.
[45] B. J. Masuda and V. G. McDonell, "Penetration of a recessed distillate liquid jet into a crossflow at elevated pressure and temperature," in *ICLASS*, Kyoto, Japan, 2006.
[46] R. Ragucci, A. Bellofiore, and A. Cavaliere, "Breakup and breakdown of bent kerosene jets in gas turbine conditions," *Proceedings of the Combustion Institute,* vol. 31, no. 2, pp. 2231-2238, 2007/01/01/ 2007, doi: https://doi.org/10.1016/j.proci.2006.07.204.
[47] L. Li, Y. Lin, X. Xue, W. Gao, and C.-J. Sung, "Injection of liquid kerosene into a high-pressure subsonic air crossflow from normal temperature to elevated temperature," in *Proceedings of ASME turbo expo*, Copenhagen, Denmark, 2012.
[48] I. T, N. N, H. T, and A. H, "Disintegration phenomena of metalized slurry fuel jets in high speed air stream," in *Proceedings of 5th international conference on liquid atomization and spray systems*, Gaithersburg (MD), 1991.
[49] M. Costa, M. J. Melo, J. M. M. Sousa, and Y. Levy, "Spray Characteristics of Angled Liquid Injection into Subsonic Crossflows," *AIAA Journal,* vol. 44, no. 3, pp. 646-653, 2006.
[50] M.-K. Kim, J. Song, J. Hwang, and Y. Yoon, "EFFECTS OF CANTED INJECTION ANGLES ON THE SPRAY CHARACTERISTICS OF LIQUID JETS IN SUBSONIC CROSSFLOWS," vol. 20, no. 9, pp. 749-762, 2010.
[51] K. Sallam, C. Aalburg, and G. Faeth, "Primary Breakup of Round Nonturbulent Liquid Jets in Gaseous Crossflows," in *41st aerospace sciences meeting and exhibit.*, Reno, Nevada, 2003.
[52] M. Rachner, J. Becker, C. Hassa, and T. Doerr, "Modelling of the atomization of a plain liquid fuel jet in crossflow at gas turbine conditions," *Aerospace Science and Technology,* vol. 6, no. 7, pp. 495-506, 2002.
[53] T. Inamura and N. Nagai, "Spray Characteristics of Liquid Jet Traversing Subsonic Airstreams," *Journal of Propulsion and Power,* vol. 13, no. 2, pp. 250-256, 1997.
[54] P.-K. Wu, K. A. Kirkendall, R. P. Fuller, and A. S. Nejad, "Spray Structures of Liquid Jets Atomized in Subsonic Crossflows," *Journal of Propulsion and Power,* vol. 14, no. 2, pp. 173-182, 1998.
[55] E. Lubarsky, J. R. Reichel, B. T. Zinn, and R. McAmis, "Spray in Crossflow: Dependence on Weber Number," *Journal of Engineering for Gas Turbines and Power,* vol. 132, no. 2, 2009.
[56] R. Surya Prakash, A. Sinha, G. Tomar, and R. V. Ravikrishna, "Liquid jet in crossflow – Effect of liquid entry conditions," *Experimental Thermal and Fluid Science,* vol. 93, pp. 45-56, 2018.
[57] E. Rathakrishnan, "Steady One-Dimensional Flow," in *Applied Gas Dynamics*, 2019, pp. 43-112.
[58] T. J. Bruno, Huber, M. L., Laesecke, A., Lemmon, E. W., Perkins, R. A., "Thermochemical and Thermophysical Properties of JP-10," NIST Interagency/Internal Reports (NISTIR), Boulder, 2006.
[59] CRC, "Handbook of aviation fuel properties, Report No. 635, Third Edition," Alpharetta, GA, 2004.
[60] CRYSTRAN, "The Design of Pressure Windows," 2014.

[61] CRYSTRAN, "Quartz Crystal (SiO2)."
[62] Swagelok, "Gaugeable Tube Fittings and Adapter Fittings," 2023.
[63] ANSYS, "ANSYS Fluent Theory Guide," 2021.
[64] T. TOKGÖZ, "Investigation of The Effect of Geometrical Parameters of Pressure Swirl Atomizer on The Hollow Cone Spray," Master of Science, The Graduate School of Natural and Applied Sciences, Middle East Technical University, 2019.
[65] F. Mayinger and O. Feldmann, *Optical Measurements*, 2nd ed. Springer, 2001.
[66] J. Shakal, "Phase Doppler Particle Analyzer," 2007.
[67] TSI, "Phase Doppler Particle Analyzer (PDPA) / Laser Doppler Velocimeter (LDV) Operations Manual, P/N 1990048, Revision G, Chapter 5," July 2011.
[68] X. Qin, X. Cao, Y. Guo, L. Xu, S. Hu, and W. Fang, "Density, Viscosity, Surface Tension, and Refractive Index for Binary Mixtures of 1,3-Dimethyladamantane with Four C10 Alkanes," *Journal of Chemical & Engineering Data,* vol. 59, no. 3, pp. 775-783, 2014/03/13 2014, doi: 10.1021/je4008926.
[69] T. G. Mayerhöfer, S. Pahlow, and J. Popp, "The Bouguer-Beer-Lambert Law: Shining Light on the Obscure," *ChemPhysChem,* vol. 21, no. 18, pp. 2029-2046, 2020, doi: https://doi.org/10.1002/cphc.202000464.
[70] S. Gangopadhyay, C. R. Landis, M. W. Pleil, W. L. Borst, and P. K. Mukhopadhyay, "Time-resolved fluorescence spectroscopy of crude oils and condensates," *Fuel,* vol. 67, no. 12, pp. 1674-1679, 1988/12/01/ 1988, doi: https://doi.org/10.1016/0016-2361(88)90214-1.
[71] T. E. Parker, D. Blair, H. Du, M. E. Fraser, L. G. Piper, and W. T. Rawlins, "Optical Instrumentation for High Temperature and Pressure Fuel Fouling Systems," U.S. Air Force Technical Report No. WL-TR-94-1037, 1994.

APPENDICES

APPENDIX 1 – Extras

Table A1.1. The required cross-sectional area of the test section.

Mach Number	Total Pressure [bar]	Total Temperature [K]	Required Cross-Sectional Area of the Test Section [mm^2]
0.1	2	393.15	1213.80
		493.15	1359.44
		593.15	1490.91
		673.15	1588.27
	5	393.15	485.52
		493.15	543.77
		593.15	596.36
		673.15	635.31
	8	393.15	303.45
		493.15	339.86
		593.15	372.73
		673.15	397.07
0.2	2	393.15	617.87
		493.15	692.00
		593.15	758.93
		673.15	808.49
	5	393.15	247.15
		493.15	276.80
		593.15	303.57
		673.15	323.40
	8	393.15	154.47
		493.15	173.00
		593.15	189.73
		673.15	202.12

Table A1.1. Continued.

Mach Number	Total Pressure [bar]	Total Temperature [K]	Required Cross-Sectional Area of the Test Section [mm^2]
0.3	2	393.15	424.29
		493.15	475.20
		593.15	521.16
		673.15	555.19
	5	393.15	169.72
		493.15	190.08
		593.15	208.46
		673.15	222.08
	8	393.15	106.07
		493.15	118.80
		593.15	130.29
		673.15	138.80
0.4	2	393.15	331.53
		493.15	371.31
		593.15	407.22
		673.15	433.81
	5	393.15	132.61
		493.15	148.52
		593.15	162.89
		673.15	173.52
	8	393.15	82.88
		493.15	92.83
		593.15	101.80
		673.15	108.45

Table A1.1. Continued.

Mach Number	Total Pressure [bar]	Total Temperature [K]	Required Cross-Sectional Area of the Test Section [mm^2]
0.5	2	393.15	279.35
		493.15	312.86
		593.15	343.12
		673.15	365.53
	5	393.15	111.74
		493.15	125.14
		593.15	137.25
		673.15	146.21
	8	393.15	69.84
		493.15	78.22
		593.15	85.78
		673.15	91.38
0.6	2	393.15	247.73
		493.15	277.45
		593.15	304.29
		673.15	324.16
	5	393.15	99.09
		493.15	110.98
		593.15	121.71
		673.15	129.66
	8	393.15	61.93
		493.15	69.36
		593.15	76.07
		673.15	81.04

Table A1.1. Continued.

Mach Number	Total Pressure [bar]	Total Temperature [K]	Required Cross-Sectional Area of the Test Section [mm^2]
0.7	2	393.15	228.17
		493.15	255.54
		593.15	280.26
		673.15	298.56
	5	393.15	91.27
		493.15	102.22
		593.15	112.10
		673.15	119.42
	8	393.15	57.04
		493.15	63.89
		593.15	70.06
		673.15	74.64

Table A1.2. Total pressure corresponding to 600 mm^2 cross-sectional area.

Mach Number	Total Temperature [K]	Cross-Sectional Area of the Test Section [mm^2]	Total Pressure [bar]
0.1	393.15	600	4.046
	493.15	600	4.531
	593.15	600	4.970
	673.15	600	5.294
0.2	393.15	600	2.060
	493.15	600	2.307
	593.15	600	2.530
	673.15	600	2.695

Table A1.2. Continued.

Mach Number	Total Temperature [K]	Cross-Sectional Area of the Test Section [mm^2]	Total Pressure [bar]
0.3	393.15	600	1.414
	493.15	600	1.584
	593.15	600	1.737
	673.15	600	1.851
0.4	393.15	600	1.105
	493.15	600	1.238
	593.15	600	1.357
	673.15	600	1.446
0.5	393.15	600	0.931
	493.15	600	1.043
	593.15	600	1.144
	673.15	600	1.218
0.6	393.15	600	0.826
	493.15	600	0.925
	593.15	600	1.014
	673.15	600	1.081
0.7	393.15	600	0.761
	493.15	600	0.852
	593.15	600	0.934
	673.15	600	0.995

Table A1.3. The updated crossflow conditions.

Mach Number	Total Pressure [bar]	Total Temperature [K]	Required Cross-Sectional Area of the Test Section [mm^2]
0.1	2.00	393.15	1213.80
		493.15	1359.44
		593.15	1490.91
		673.15	1588.27
	4.00	393.15	606.90
		493.15	679.72
		593.15	745.45
		673.15	794.14
0.2	2.00	393.15	617.87
		493.15	692.00
		593.15	758.93
		673.15	808.49
0.3	1.41	393.15	601.84
		493.15	674.04
		593.15	739.23
		673.15	787.51
0.4	1.10	393.15	602.78
		493.15	675.11
		593.15	740.40
		673.15	788.75

Table A1.4. Maximum penetration height for HTP conditions for Bellofiore and Ragucci when d_j is 0.4 mm and $\dot{m}_j$ is 4 g/s.

M	P_t [bar]	Tt [K]	P_g [bar]	T_g [K]	q	We_{aero}	z [mm] (Bellofiore)	z [mm] (Ragucci)
0.1	2.00	393.15	1.99	392.37	389.44	26.34	25.54	27.80
0.1	2.00	493.15	1.99	492.17	389.44	21.00	25.35	28.73
0.1	2.00	593.15	1.99	591.97	389.44	17.46	25.21	29.48
0.1	2.00	673.15	1.99	671.81	389.44	15.38	25.12	29.99
0.1	4.00	393.15	3.97	392.37	194.72	52.67	18.46	20.53
0.1	4.00	493.15	3.97	492.17	194.72	41.99	18.31	21.22
0.1	4.00	593.15	3.97	591.97	194.72	34.91	18.21	21.78
0.1	4.00	673.15	3.97	671.81	194.72	30.76	18.15	22.15
0.2	2.00	393.15	1.94	390.03	99.42	25.95	14.65	15.62
0.2	2.00	493.15	1.94	489.24	99.42	20.68	14.53	16.14
0.2	2.00	593.15	1.94	588.44	99.42	17.20	14.45	16.56
0.2	2.00	673.15	1.94	667.81	99.42	15.15	14.40	16.85
0.3	1.41	393.15	1.32	386.20	64.88	17.85	12.60	13.10
0.3	1.41	493.15	1.32	484.43	64.88	14.23	12.50	13.54
0.3	1.41	593.15	1.32	582.66	64.88	11.83	12.43	13.89
0.3	1.41	673.15	1.32	661.25	64.88	10.42	12.39	14.13

Table A1.5. Maximum penetration height for HTP conditions for Masuda, Li, and Eslamian when d_j is 0.4 mm and $\dot{m}_j$ is 4 g/s.

M	P_t [bar]	Tt [K]	P_g [bar]	T_g [K]	q	We_g	z [mm] (Masuda)	z [mm] (Li)	z [mm] (Eslamian)
0.1	2.00	393.15	1.99	392.37	389.44	35.88	60.10	33.59	19.40
0.1	2.00	493.15	1.99	492.17	389.44	35.88	60.10	35.92	18.78
0.1	2.00	593.15	1.99	591.97	389.44	35.88	60.10	37.93	18.29
0.1	2.00	673.15	1.99	671.81	389.44	35.88	60.10	39.37	17.98
0.1	4.00	393.15	3.97	392.37	194.72	71.75	31.98	25.04	17.12
0.1	4.00	493.15	3.97	492.17	194.72	71.75	31.98	26.77	16.57
0.1	4.00	593.15	3.97	591.97	194.72	71.75	31.98	28.27	16.15
0.1	4.00	673.15	3.97	671.81	194.72	71.75	31.98	29.34	15.87
0.2	2.00	393.15	1.94	390.03	99.42	140.54	17.35	18.79	13.97
0.2	2.00	493.15	1.94	489.24	99.42	140.54	17.35	20.09	13.52
0.2	2.00	593.15	1.94	588.44	99.42	140.54	17.35	21.22	13.18
0.2	2.00	673.15	1.94	667.81	99.42	140.54	17.35	22.02	12.95
0.3	1.41	393.15	1.32	386.20	64.88	215.36	11.76	15.64	12.34
0.3	1.41	493.15	1.32	484.43	64.88	215.36	11.76	16.72	11.95
0.3	1.41	593.15	1.32	582.66	64.88	215.36	11.76	17.65	11.64
0.3	1.41	673.15	1.32	661.25	64.88	215.36	11.76	18.32	11.44

Table A1.6. Maximum penetration height for HTSP conditions for Stenzler-1 and Lakhamraju when d_j is 0.4 mm and $\dot{m}_j$ is 4 g/s.

M	P_t [bar]	T_t [K]	P_g [bar]	T_g [K]	q	We_g	z [mm] (Stenzler-1)	z [mm] (Lakhamraju)
0.4	1.10	393.15	0.99	380.96	49.07	284.75	20.90	9.52
0.4	1.10	493.15	0.99	477.86	49.07	284.75	20.90	9.27
0.4	1.10	593.15	0.99	574.76	49.07	284.75	20.90	9.07
0.4	1.10	673.15	0.99	652.28	49.07	284.75	20.90	8.94

Table A1.7. Maximum penetration height for HTSP conditions for Stenzler-2 and Yoon when d_j is 0.4 mm and $\dot{m}_j$ is 4 g/s.

M	P_t [bar]	T_t [K]	P_g [bar]	T_g [K]	q	We_g	z [mm] (Stenzler-2)	z [mm] (Yoon)
0.4	1.10	393.15	0.99	380.96	49.07	284.75	26.78	16.56
0.4	1.10	493.15	0.99	477.86	49.07	284.75	26.78	16.56
0.4	1.10	593.15	0.99	574.76	49.07	284.75	26.78	16.56
0.4	1.10	673.15	0.99	652.28	49.07	284.75	26.78	16.56

Table A1.8. Parts of test setup assemblies.

Name	Part/Standard Code	Material	Quantity	Note
Blind flange	EN-1092-1/05(B)/DN150/PN16	Stainless steel	1	-
Screw, M20X80	ISO 4017 M20X80 A2	Stainless steel	24	-
Nut, M20	ISO 4032 M20 A2	Stainless steel	24	-
Washer, 20	ISO 7089 20 A2	Stainless steel	48	-
Plenum chamber flange gasket	-	Graphite	2	-

Table A1.8. Continued.

Name	Part/Standard Code	Material	Quantity	Note
Pressure sensor	Kistler 4260A 300BRBA10B1	-	1	-
Thermocouple	OM04-T115-16 2K-TT and OM04-T115-50 2K-TT	T type	4	-
Surface thermocouple	-	K type	1	-
Plug, NPT-1/8	-	Stainless steel	2	-
Male connector, NPT-1/8	Swagelok SS-100-1-2BT	Stainless steel	3	-
Plenum chamber assembly	-	See Section 2.4.1	1	-
Preliminary acceleration section	-	Stainless steel	1	-
Male connector, BSP-1/8-28	Swagelok SS-100-1-2RSBT	Stainless steel	2	-
Fuel supply line 1	-	See Section 2.4.7	1	-
Male connector, UNF-3/4-16	Swagelok SS-810-1-8ST	Stainless steel	2	-
High-pressure chamber flange gasket	-	Graphite	1	-
Fuel supply line 2	-	See Section 2.4.7	1	-
Positionable elbow	Swagelok SS-400-2-4ST	Stainless steel	1	-
Injector	-	Stainless steel	1	There are three different injectors. They are given in Section 2.4.4.
Screw, M5X25	ISO 4762 M5X25 A2-70	Stainless steel	16	-
Washer, 5	ISO 7089 5 A2	Stainless steel	52	-

Table A1.8. Continued.

Name	Part/Standard Code	Material	Quantity	Note
Screw, M3X8	ISO 4762 M3X8 A2-70	Stainless steel	32	-
Washer, 3	ISO 7089 3 A2	Stainless steel	32	-
Plug, M16	-	Stainless steel	1	-
Test section window	-	Optical grade fused quartz	2	-
Test section window holder	-	Stainless steel	2	-
Test section	-	Stainless steel	1	-
Screw, M5X12	ISO 4762 M5X12 A2-70	Stainless steel	36	-
High-pressure chamber window	-	Optical grade fused quartz	2	-
High-pressure chamber window holder	-	Stainless steel	2	-
High-pressure chamber assembly, PDPA	-	See Section 2.4.8	1	It is only used in PDPA test setup assembly.
High-pressure chamber assembly, shadowgraphy	-	See Section 2.4.9	1	It is only used in shadowgraphy test setup assembly.
Liquid sealant	Loctite SI 5910	RTV silicone	-	It is used as a sealant element for required sections.
Teflon tape	-	PTFE	-	It is used as a sealant element for required sections.

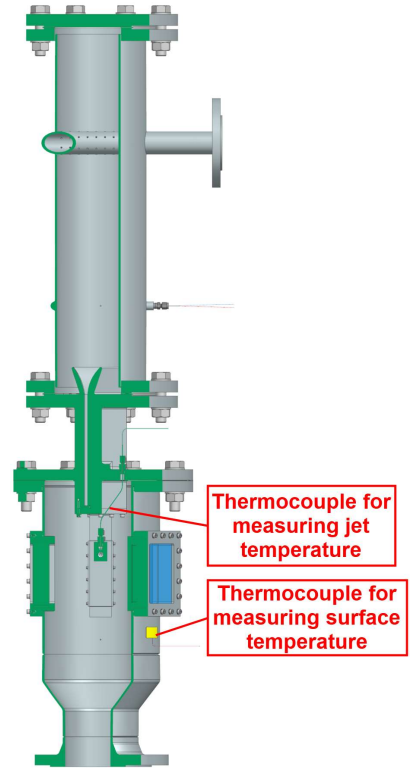

Figure A1.1. PDPA Test setup assembly (cross-sectional view 3).

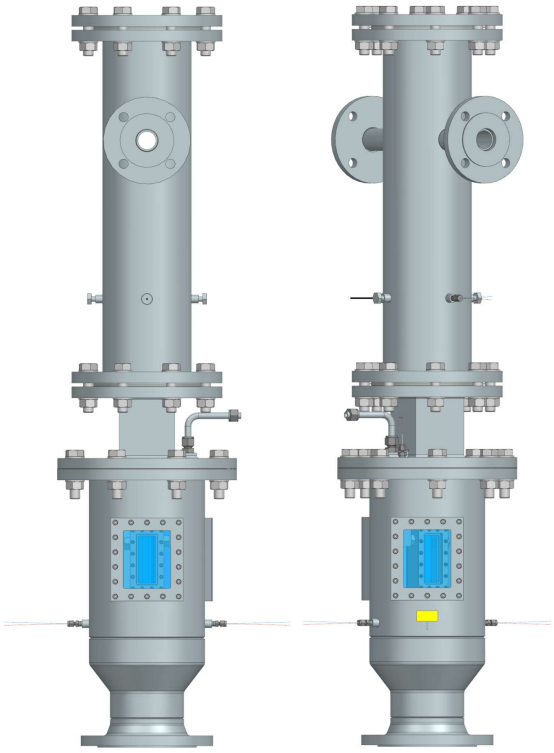

Figure A1.2. PDPA Test setup assembly (view from both windows on the setup).

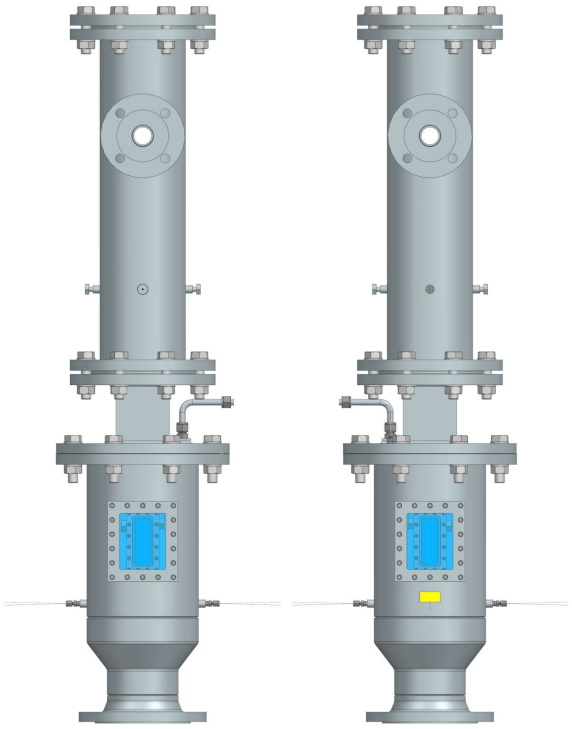

Figure A1.3. Shadowgraphy test setup assembly (view from both windows on the setup).

Table A1.9. Parts of plenum chamber assembly.

Name	Part/Standard Code	Material	Quantity
Plenum flange	EN-1092-1/01(B)/DN150/PN10-16	Stainless steel	2
Plenum chamber	EN ISO 1127 (outer dia.: 168.3 mm, thickness: 4 mm)	Stainless steel	1
Flow uniformity pipe flange	EN-1092-1/05(B)/DN50/PN10-16	Stainless steel	2
Flow uniformity pipe	EN ISO 1127 (outer dia.: 42.4 mm, thickness: 4 mm)	Stainless steel	1
Pressure sensor fitting	-	Stainless steel	1
Thermocouple Fitting	-	Stainless steel	3

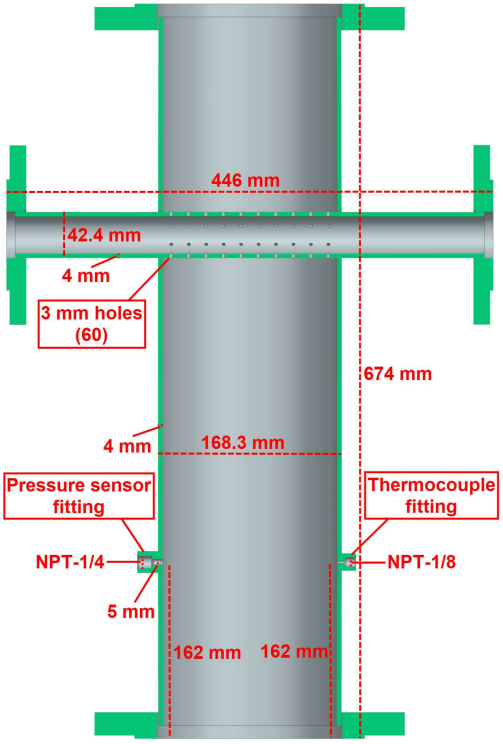

Figure A1.4. Plenum chamber assembly (cross-sectional view 1).

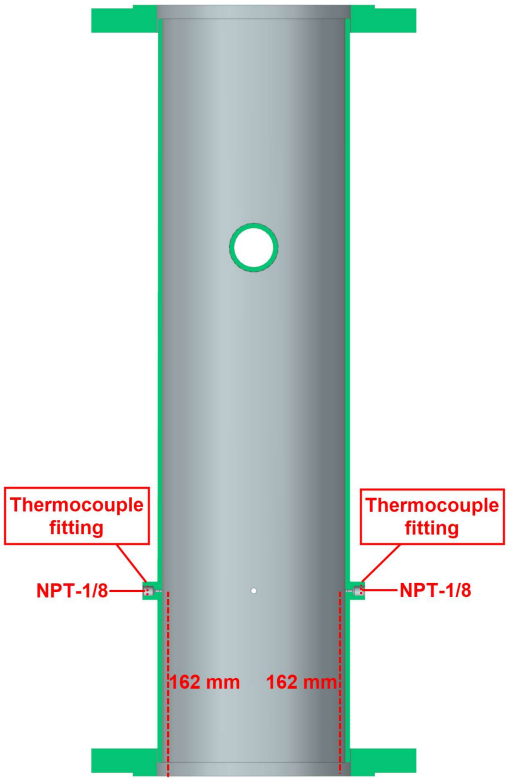

Figure A1.5. Plenum chamber assembly (cross-sectional view 2).

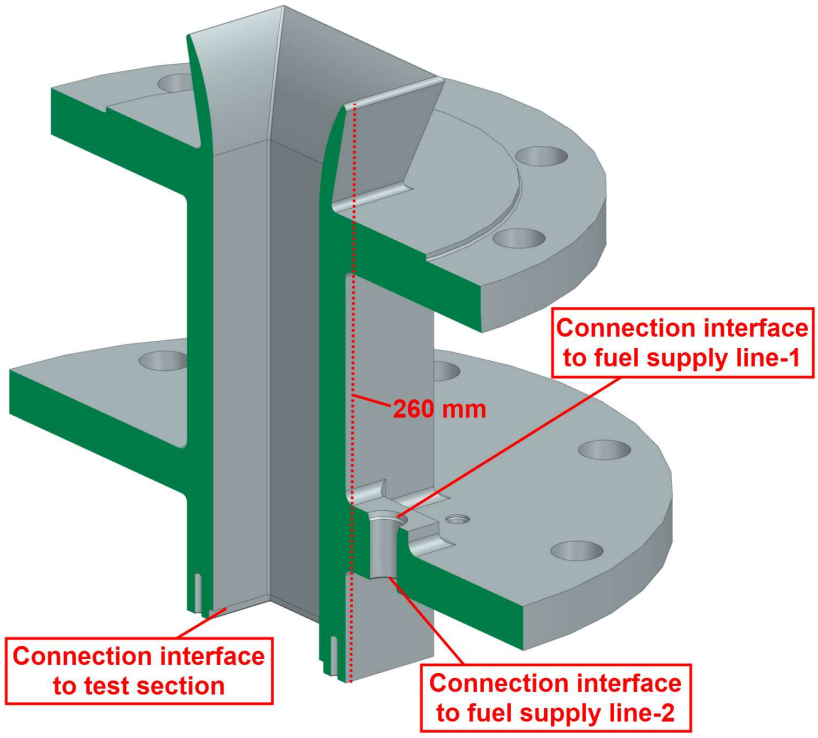

Figure A1.6. Preliminary acceleration section (cross-sectional view).

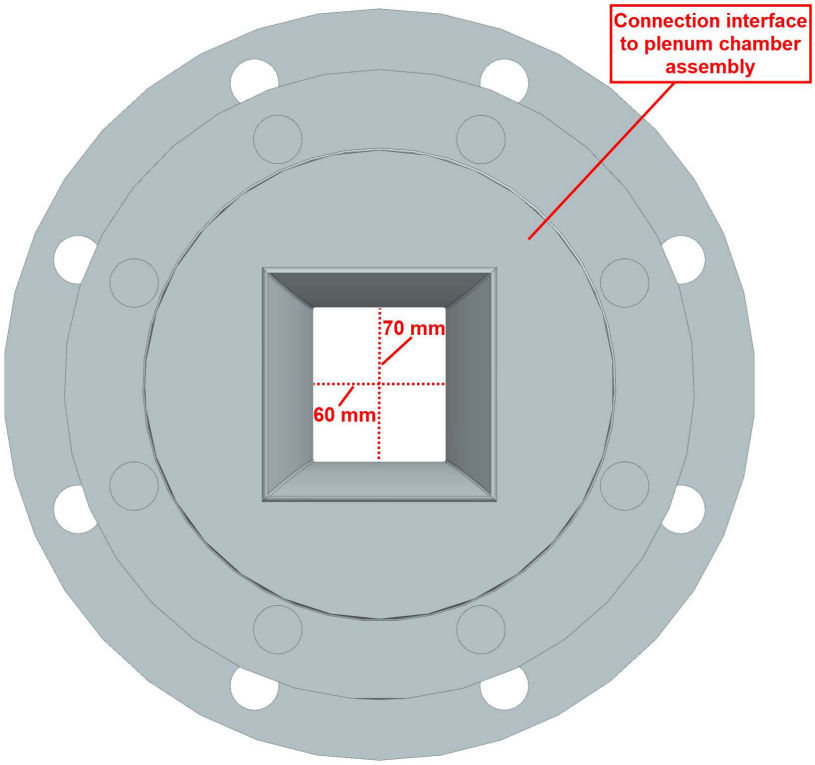

Figure A1.7. Preliminary acceleration section (top view).

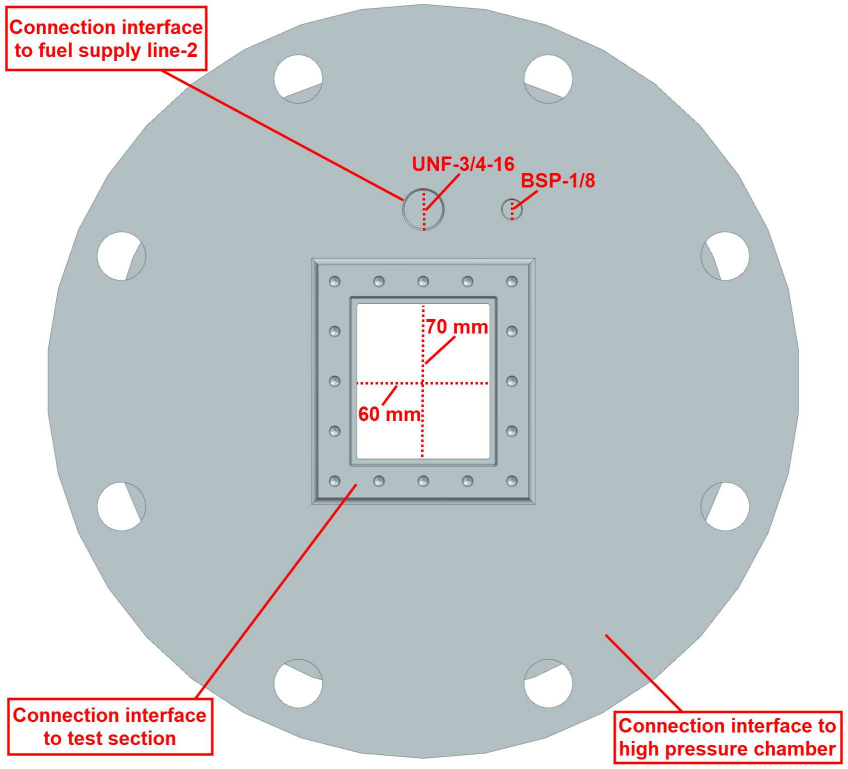

Figure A1.8. Preliminary acceleration section (bottom view).

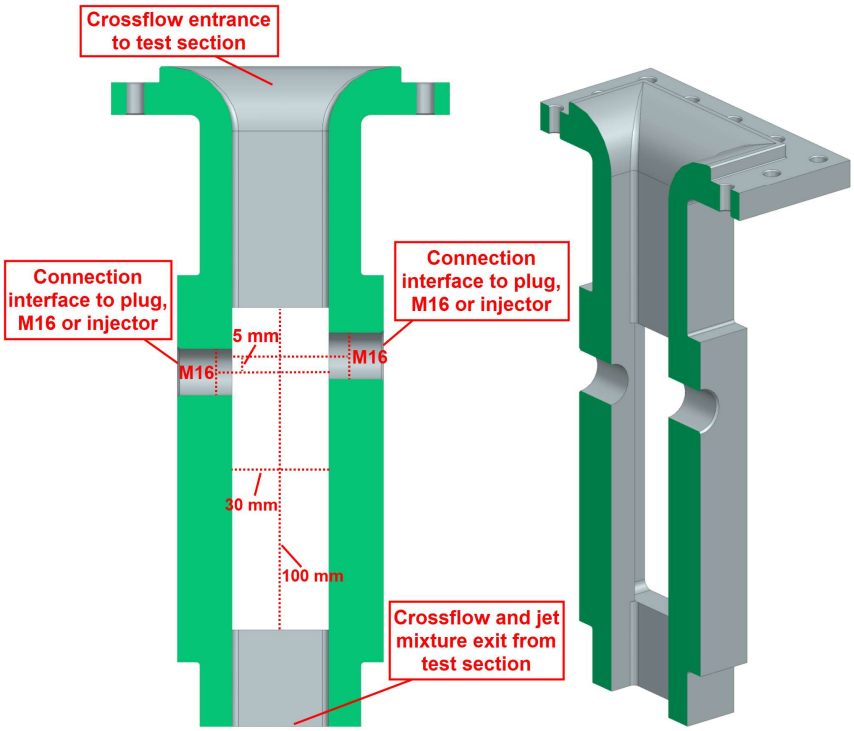

Figure A1.9. Test section (cross-sectional view 1).

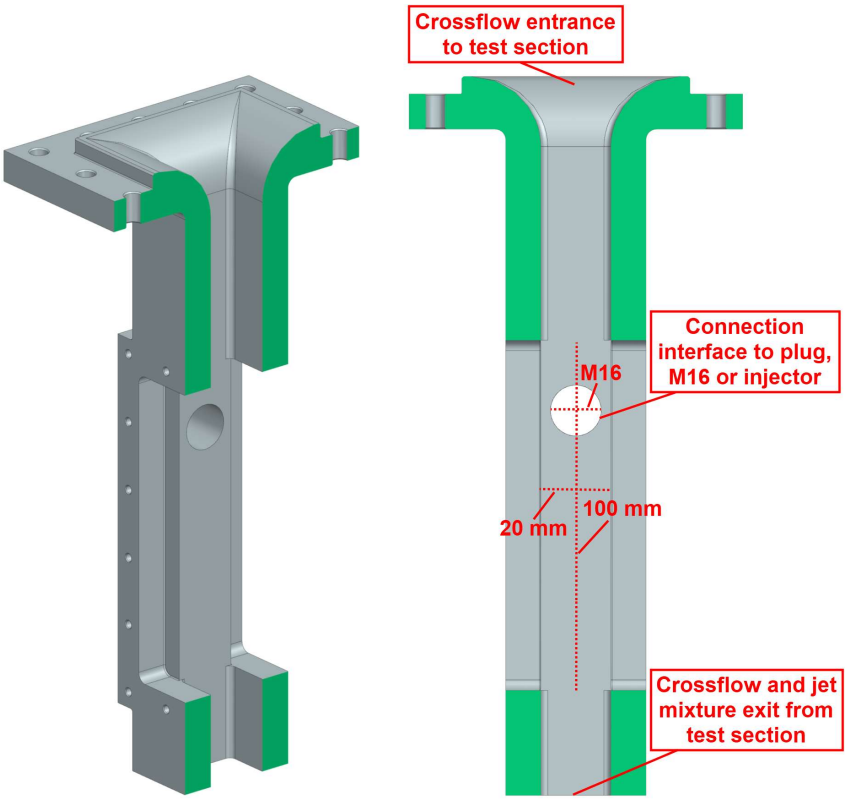

Figure A1.10. Test section (cross-sectional view 2).

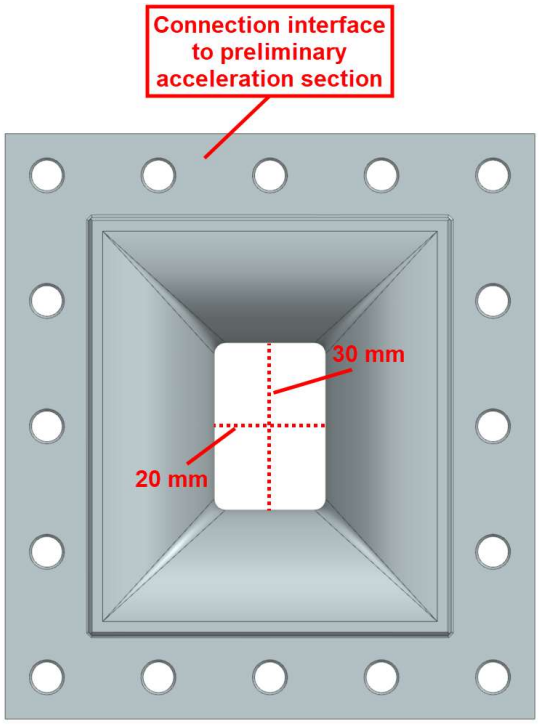

Figure A1.11. Test section (top view).

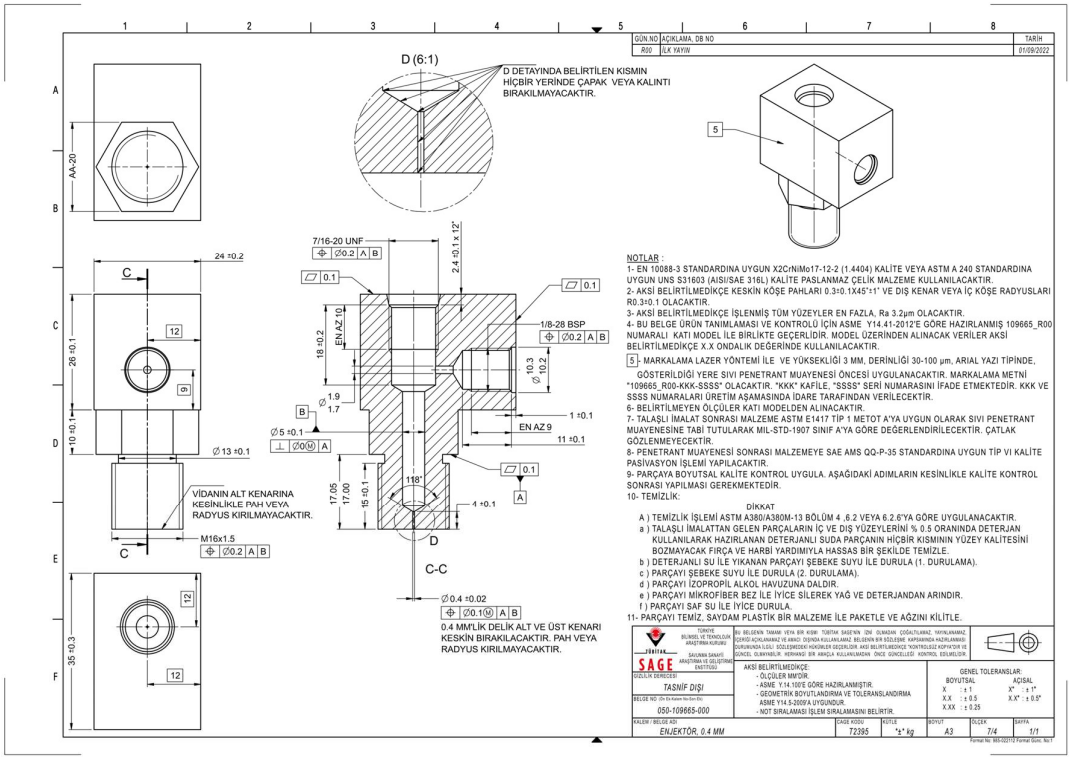

Figure A1.12. Technical drawing of injector, 0.4 mm.

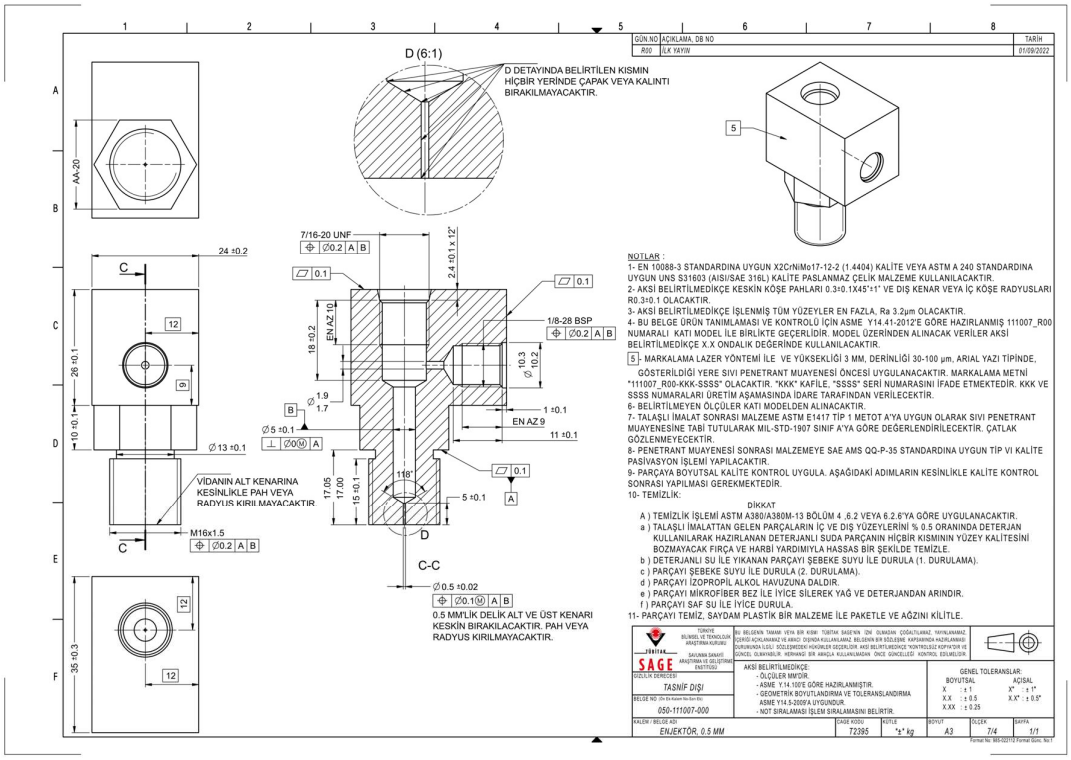

Figure A1.13. Technical drawing of injector, 0.5 mm.

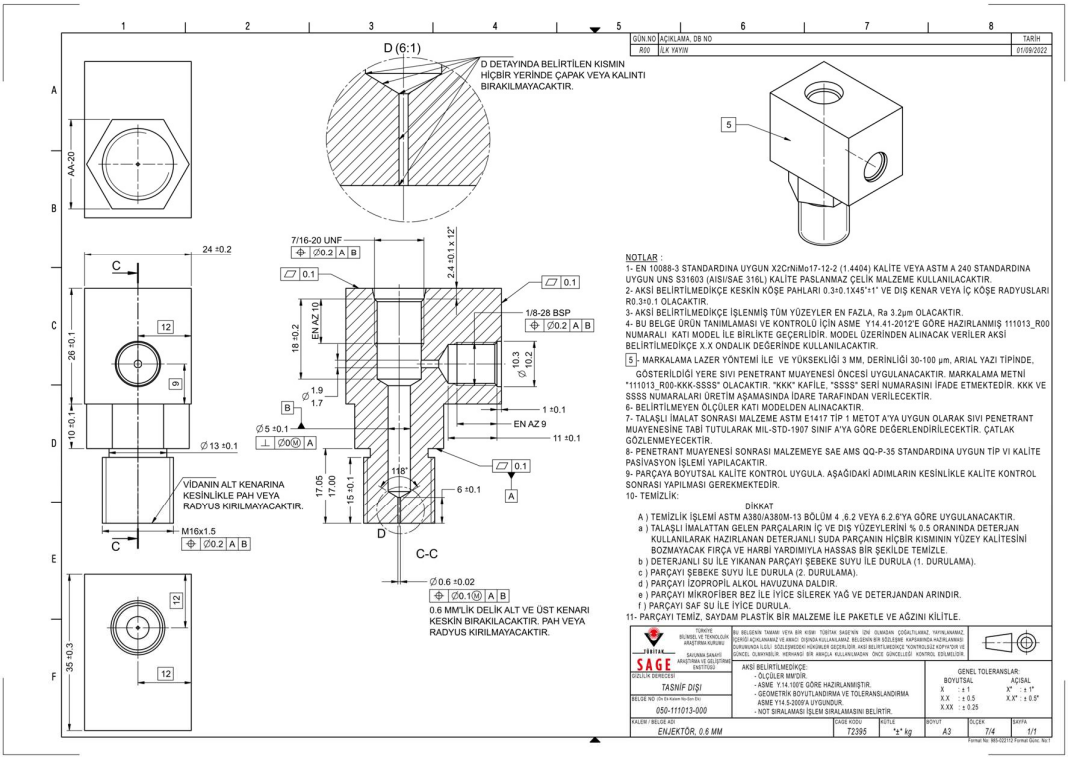

Figure A1.14. Technical drawing of injector, 0.6 mm.

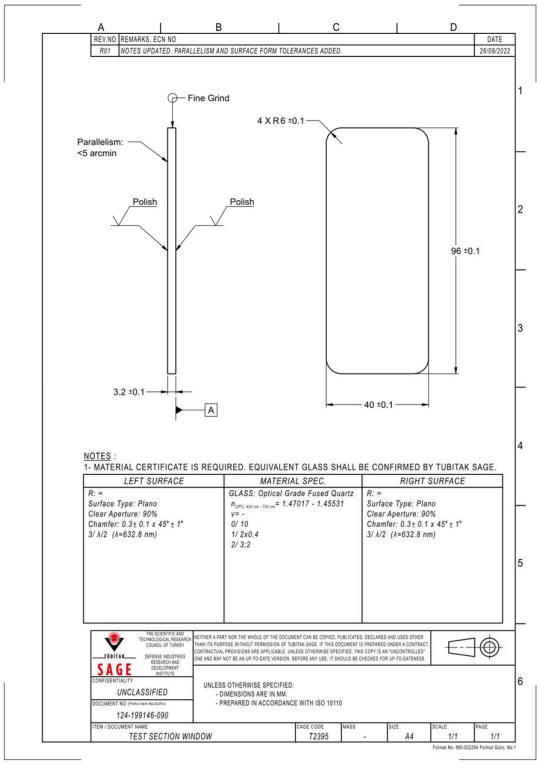

Figure A1.15. Technical drawing of test section window.

Table A1.10. Parts of fuel supply line 1.

Name	Part/Standard Code	Material	Quantity
Fuel pipe 1	CFP TUBE-12.7x1.35-EN 10216-5-D4-T4	Stainless steel	1
Nut, 810	Swagelok SS-812-1	Stainless steel	2
Ferrule set, 810	Swagelok SS-810-SET	Stainless steel	2

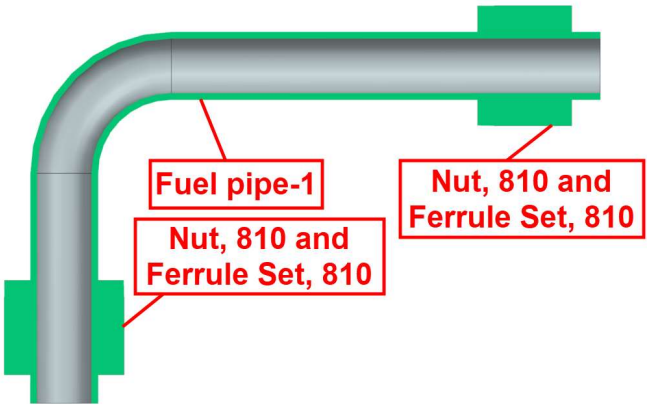

Figure A1.16. Fuel supply line-1 (cross-sectional view).

Table A1.11. Parts of fuel supply line 2.

Name	Part/Standard Code	Material	Quantity
Fuel pipe-2	CFA TUBE-6.35x0.89-EN 10216-5-D4-T3	Stainless steel	1
Adaptor	-	Stainless steel	1
Nut, 400	Swagelok SS-402-1	Stainless steel	1
Ferrule set, 400	Swagelok SS-400-SET	Stainless steel	1
Nut, 810	Swagelok SS-812-1	Stainless steel	1
Ferrule set, 810	Swagelok SS-810-SET	Stainless steel	1

Table A1.12. Parts of high-pressure chamber assembly, PDPA.

Name	Part/Standard Code	Material	Quantity
High-pressure chamber flange top	-	Stainless steel	1
High-pressure chamber flange bottom	EN-1092-1/11(B)/DN125/PN10-16	Stainless steel	1
High-pressure chamber window connection wall	-	Stainless steel	2
High-pressure chamber, PDPA	EN ISO 1127 (outer dia.: 219.1 mm, thickness: 5 mm)	Stainless steel	1
Reducer	200 concentric reducer/EN 10253-3 /219.1 x 5.0/139.7 x 4.0	Stainless steel	1
Thermocouple fitting	-	Stainless steel	2

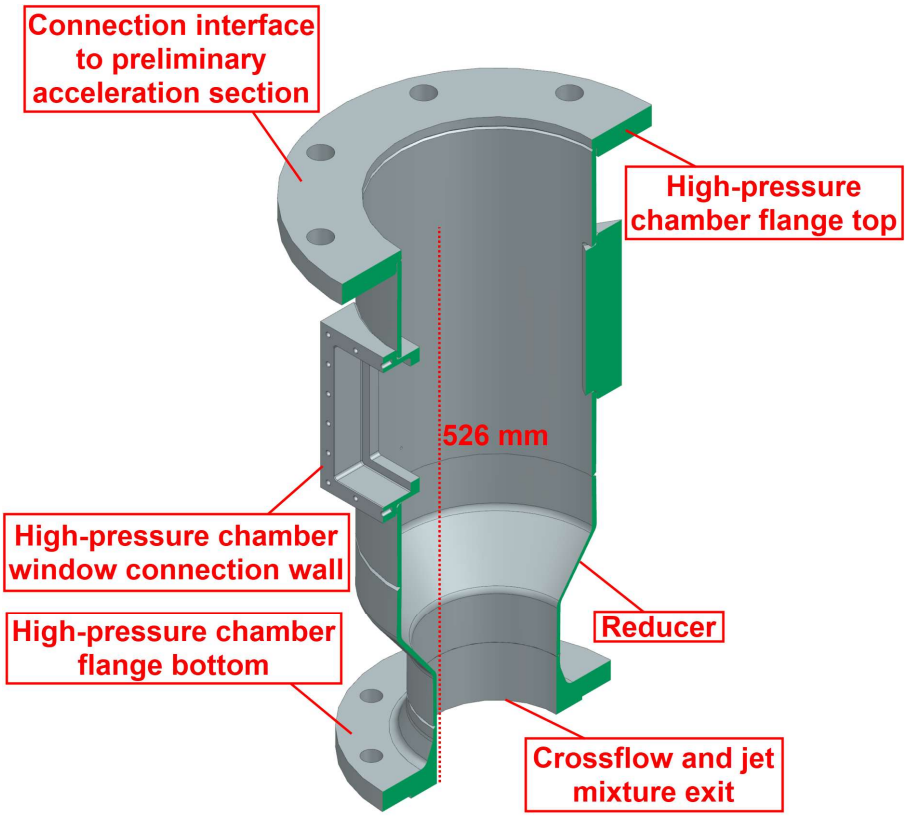

Figure A1.17. High-pressure chamber assembly, PDPA (cross-sectional view 1).

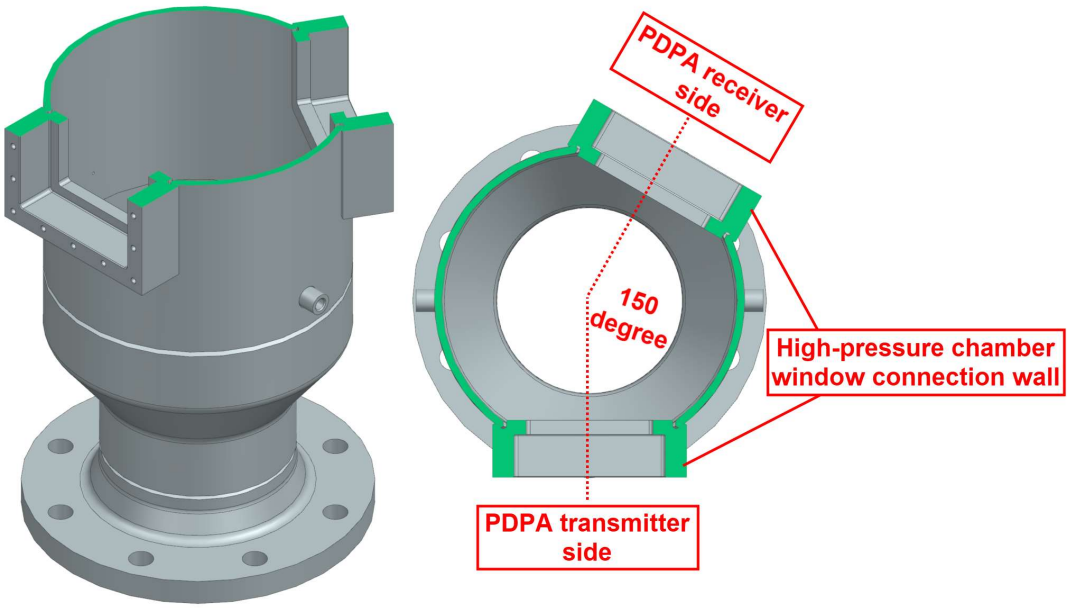

Figure A1.18. High-pressure chamber assembly, PDPA (cross-sectional view 2).

Table A1.13. Parts of high-pressure chamber assembly, shadowgraphy.

Name	Part/Standard Code	Material	Quantity
High-pressure chamber flange top	-	Stainless steel	1
High-pressure chamber flange bottom	EN-1092-1/11(B)/DN125/PN10-16	Stainless steel	1
High-pressure chamber window connection wall	-	Stainless steel	2
High-pressure chamber, shadowgraphy	EN ISO 1127 (outer dia.: 219.1 mm, thickness: 5 mm)	Stainless steel	1
Reducer	200 concentric reducer/EN 10253-3 /219.1 x 5.0/139.7 x 4.0	Stainless steel	1
Thermocouple fitting	-	Stainless steel	2

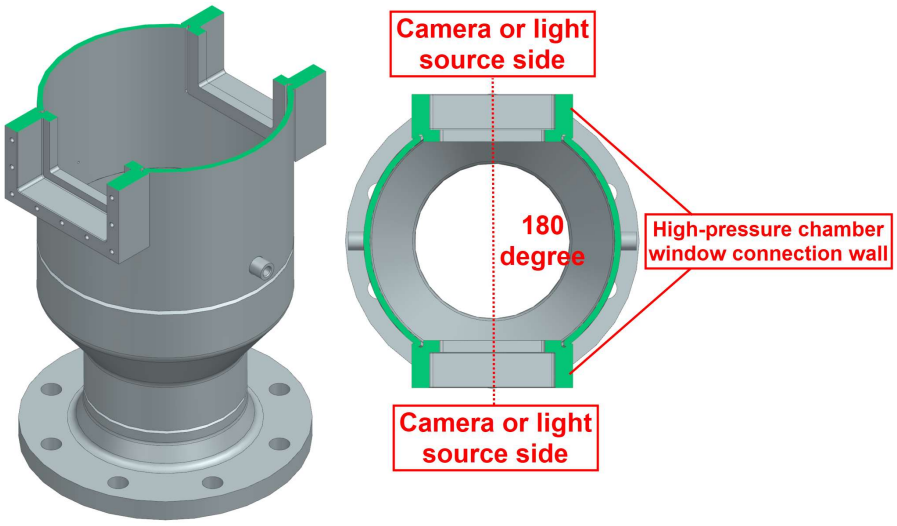

Figure A1.19. High-pressure chamber assembly, shadowgraphy (cross-sectional view).

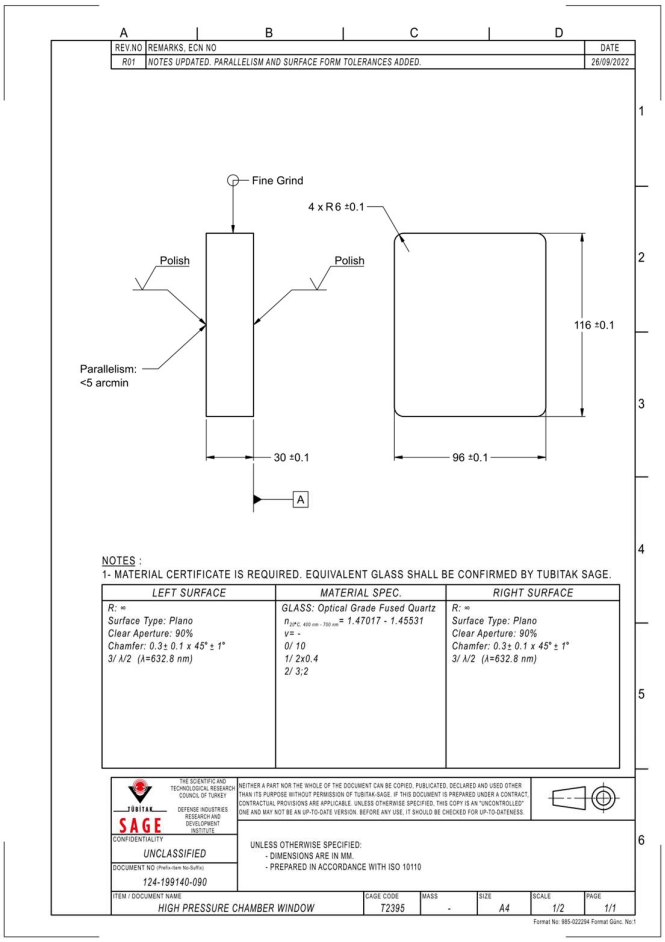

Figure A1.20. Technical drawing of the high-pressure chamber window.

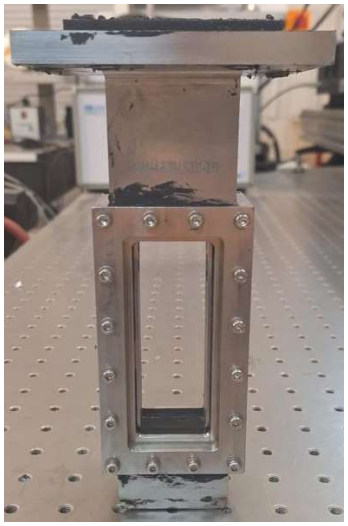

Figure A1.21. Test section with window assembled.

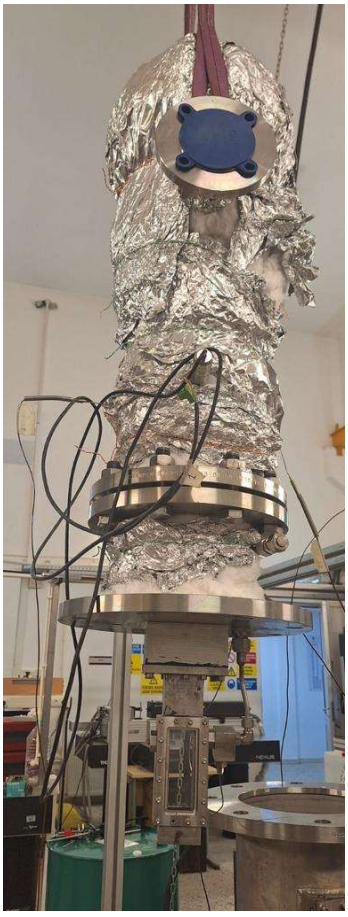

Figure A1.22. Test setup sub-assembly view.

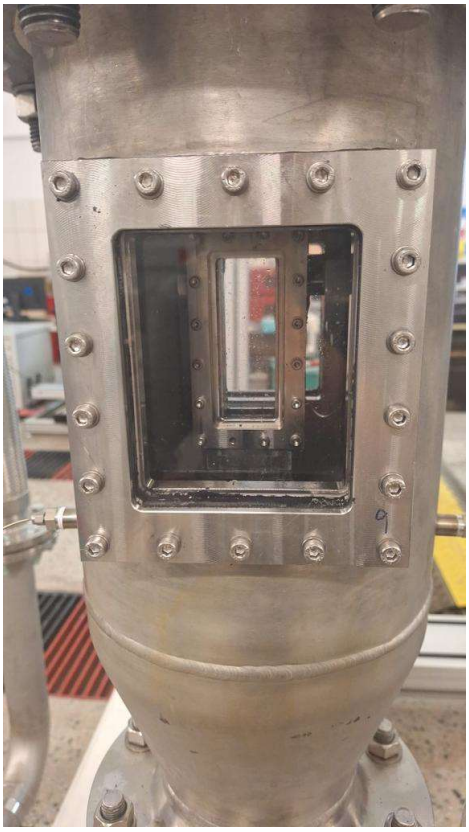

Figure A1.23. Test section view from windows.

Table A1.14. The diameter of produced injectors.

Part Number	Injector Diameter [mm]
109665-R00-LS001_0001	0.428
109665-R00-LS001_0002	0.392
109665-R00-LS001_0003	0.421
111007-R00-LS001_0001	0.524
111007-R00-LS001_0002	0.521
111007-R00-LS001_0003	0.520
111013-R00-LS001_0001	0.606
111013-R00-LS001_0002	0.629
111013-R00-LS001_0003	0.622
111013-R00-LS001_0004	0.624

Table A1.15. Data of the discharge coefficient measurement experiment.

Part Number	P_{flow} [bar]	$S_{P_{flow}}$ [bar]	P_{amb} [bar]	$S_{P_{amb}}$ [bar]	T_{flow} [ºC]	$S_{T_{flow}}$ [ºC]	$m_{fuel\ storage\ tank}$ [g]	t_{test} [s]
109665-R00-LS001_0001 (3 g/s experiment)	3.454	0.180	0.865	0.001	11.610	0.013	90.69	31.22
109665-R00-LS001_0001 (4 g/s experiment)	5.806	0.181	0.859	0.001	22.608	0.019	123.89	30.66
109665-R00-LS001_0001 (5 g/s experiment)	8.721	0.217	0.859	0.001	20.521	0.024	160.99	32.50
109665-R00-LS001_0002 (3 g/s experiment)	4.166	0.202	0.864	0.001	10.833	0.006	95.39	32.40
109665-R00-LS001_0002 (4 g/s experiment)	5.873	0.184	0.859	0.001	21.038	0.016	115.53	30.46
109665-R00-LS001_0002 (5 g/s experiment)	8.789	0.216	0.859	0.001	20.374	0.025	150.15	30.96
109665-R00-LS001_0003 (3 g/s experiment)	3.993	0.192	0.865	0.001	11.640	0.013	93.15	30.75
109665-R00-LS001_0003 (4 g/s experiment)	5.836	0.192	0.859	0.001	22.014	0.013	120.15	30.62
109665-R00-LS001_0003 (5 g/s experiment)	8.725	0.218	0.859	0.001	20.898	0.010	156.02	31.11
111007-R00-LS001_0001 (3 g/s experiment)	2.287	0.197	0.864	0.001	12.418	0.017	89.86	30.05

Table A1.15. Continued.

Part Number	P_{flow} [bar]	$S_{P_{flow}}$ [bar]	P_{amb} [bar]	$S_{P_{amb}}$ [bar]	T_{flow} [ºC]	$S_{T_{flow}}$ [ºC]	$m_{fuel\ storage\ tank}$ [g]	t_{test} [s]
111007-R00-LS001_0001 (4 g/s experiment)	3.135	0.159	0.863	0.001	12.899	0.014	119.46	30.85
111007-R00-LS001_0001 (5 g/s experiment)	4.737	0.157	0.859	0.001	20.064	0.009	156.55	29.74
111007-R00-LS001_0002 (3 g/s experiment)	2.282	0.171	0.864	0.001	12.538	0.059	95.72	30.90
111007-R00-LS001_0002 (4 g/s experiment)	3.132	0.156	0.864	0.001	12.857	0.017	122.49	30.28
111007-R00-LS001_0002 (5 g/s experiment)	4.643	0.163	0.860	0.001	20.661	0.015	163.43	30.24
111007-R00-LS001_0003 (3 g/s experiment)	2.267	0.142	0.866	0.001	10.701	0.010	96.14	31.18
111007-R00-LS001_0003 (4 g/s experiment)	3.123	0.174	0.865	0.001	10.534	0.015	126.42	31.25
111007-R00-LS001_0003 (5 g/s experiment)	4.359	0.183	0.866	0.001	11.100	0.007	156.34	31.16
111013-R00-LS001_0001 (3 g/s experiment)	1.600	0.031	0.864	0.001	12.049	0.030	88.50	30.64
111013-R00-LS001_0001 (4 g/s experiment)	2.188	0.169	0.864	0.001	13.193	0.013	123.83	31.52

Table A1.15. Continued.

Part Number	P_{flow} [bar]	$S_{P_{flow}}$ [bar]	P_{amb} [bar]	$S_{P_{amb}}$ [bar]	T_{flow} [ºC]	$S_{T_{flow}}$ [ºC]	$m_{fuel\ storage\ tank}$ [g]	t_{test} [s]
111013-R00-LS001_0001 (5 g/s experiment)	2.967	0.127	0.859	0.001	19.010	0.013	159.12	30.60
111013-R00-LS001_0002 (3 g/s experiment)	1.621	0.032	0.864	0.001	11.675	0.019	93.90	32.44
111013-R00-LS001_0002 (4 g/s experiment)	2.257	0.122	0.862	0.001	19.633	0.019	119.70	29.22
111013-R00-LS001_0002 (5 g/s experiment)	2.935	0.116	0.860	0.001	19.412	0.022	160.79	31.27
111013-R00-LS001_0003 (3 g/s experiment)	1.584	0.035	0.864	0.001	11.242	0.028	90.48	31.41
111013-R00-LS001_0003 (4 g/s experiment)	2.263	0.142	0.861	0.001	21.651	0.013	124.93	30.38
111013-R00-LS001_0003 (5 g/s experiment)	2.949	0.134	0.860	0.001	18.940	0.014	163.00	31.34
111013-R00-LS001_0004 (3g/s experiment)	1.620	0.025	0.863	0.001	11.507	0.011	90.17	30.84
111013-R00-LS001_0004 (4 g/s experiment)	2.207	0.166	0.864	0.001	13.747	0.036	126.64	31.28
111013-R00-LS001_0004 (5 g/s experiment)	2.952	0.129	0.859	0.001	18.335	0.006	159.35	30.22

Table A1.16. Transmittance and Attenuation Coefficient of JP-10.

Wavelength [nm]	Transmittance [%]	Attenuation Coefficient [1/mm] x 10^{-4}
300	81.83	87.09
310	76.72	115.1
320	76.57	115.9
330	76.63	115.6
340	76.58	115.9
350	76.54	116.1
360	76.61	115.7
370	76.69	115.3
380	76.67	115.4
390	76.58	115.9
400	76.61	115.7
410	76.69	115.3
420	76.74	115.0
430	76.68	115.3
440	76.72	115.1
450	76.72	115.1
460	76.68	115.3
470	76.48	116.5
480	76.49	116.4
490	76.56	116.0
500	76.58	115.9
510	76.48	116.5
520	76.46	116.6
530	76.48	116.5
540	76.58	115.9
550	76.64	115.6
560	76.80	114.6

Table A1.16. Continued.

Wavelength [nm]	Transmittance [%]	Attenuation Coefficient [1/mm] x 10^{-4}
570	76.86	114.3
580	76.84	114.4
590	76.82	114.5
600	76.83	114.5
610	76.88	114.2
620	76.89	114.1
630	76.89	114.1
640	76.86	114.3
650	76.86	114.3
660	76.83	114.5
670	76.83	114.5
680	76.82	114.5
690	76.73	115.0
700	76.72	115.1
710	76.77	114.8
720	76.71	115.2
730	76.63	115.6
740	76.65	115.5
750	76.66	115.4
760	76.68	115.3
770	76.72	115.1
780	76.64	115.6
790	76.66	115.4
800	76.55	116.1
810	76.51	116.3
820	76.54	116.1
830	76.50	116.3

Table A1.16. Continued.

Wavelength [nm]	Transmittance [%]	Attenuation Coefficient [1/mm] x 10^{-4}
840	76.47	116.5
850	76.46	116.6
860	76.35	117.2
870	76.44	116.7
880	76.44	116.7
890	78.44	105.5
900	78.45	105.4
910	78.42	105.6
920	78.43	105.5
930	78.39	105.7
940	78.39	105.7
950	78.34	106.0
960	78.33	106.1
970	78.30	106.2
980	78.25	106.5
990	78.28	106.4
1000	78.25	106.5
1010	78.27	106.4
1020	78.27	106.4
1030	78.29	106.3
1040	78.27	106.4
1050	78.25	106.5
1060	78.33	106.1
1070	78.43	105.5
1080	78.41	105.6
1090	78.33	106.1
1100	78.29	106.3

Table A1.17. Sensor data 2.

Case		D_1 [K]	D_2 [K]	D_3 [K]	D_4 [K]
2 g/s [1st]	Average	460.87	462.05	410.44	290.80
	Deviation	±7.2026x10^{-2}	±1.2428x10^{-1}	±7.1299x10^{-2}	±5.2148x10^{-3}
2 g/s [2nd]	Average	458.58	460.19	409.32	291.02
	Deviation	±1.0115x10^{-1}	±1.8838x10^{-1}	±2.9383x10^{-1}	±6.1221x10^{-3}
3 g/s [1st]	Average	457.40	458.25	411.00	290.50
	Deviation	±5.2189x10^{-2}	±6.6914x10^{-2}	±5.0825x10^{-2}	±4.7294x10^{-3}
3 g/s [2nd]	Average	456.39	457.30	409.19	290.87
	Deviation	±2.7949x10^{-2}	±8.3755x10^{-2}	±9.5507x10^{-2}	±8.7512x10^{-3}
4 g/s [1st]	Average	454.28	454.85	409.50	290.00
	Deviation	±6.9424x10^{-2}	±4.1213x10^{-2}	±2.3672x10^{-2}	±8.4657x10^{-3}
4 g/s [2nd]	Average	455.39	456.05	412.65	290.61
	Deviation	±5.4072x10^{-2}	±5.8795x10^{-2}	±4.1278x10^{-2}	±9.0540x10^{-3}

Table A1.18. Sensor data 3.

Case		D_5 [bar]	D_6 [K]
2 g/s [1st]	Average	2.203	164.14
	Deviation	±3.084x10^{-2}	±1.0517
2 g/s [2nd]	Average	2.249	163.29
	Deviation	±3.131x10^{-2}	±1.5303
3 g/s [1st]	Average	2.906	167.38
	Deviation	±3.064x10^{-2}	±5.9375
3 g/s [2nd]	Average	2.861	168.22
	Deviation	±3.080x10^{-2}	±6.7812
4 g/s [1st]	Average	3.769	169.20
	Deviation	±3.208x10^{-2}	±4.7207
4 g/s [2nd]	Average	3.733	167.89
	Deviation	±3.103x10^{-2}	±1.1904

In Table A1.17 and A1.18, D_1, D_2, D_3, D_4, D_5 and D_6 represent high-pressure chamber temperatures 1 and 2, high-pressure chamber surface temperature, fuel temperature and pressure before entering the injector in the conditioned fuel feeding system, and flow rate in line 2, respectively.